UNIVERSITY OF LATVIA

DOCTORAL THESIS

Dynamics of spontaneously magnetized micro-filaments under an external magnetic field: Experimental investigation

Author:
Abdelqader ZABEN

Supervisor:
Prof. Andrejs CĒBERS
Dr. Guntars KITENBERGS

A thesis submitted in fulfillment of the requirements for the degree of Doctor of Physics

Subfield

Fluid and gas mechanics
Faculty of Physics, Mathematics and Opometry

October 10, 2022

Declaration of Authorship

I, Abdelqader ZABEN, declare that this thesis titled, "Dynamics of spontaneously magnetized micro-filaments under an external magnetic field: Experimental investigation" and the work presented in it are my own. I confirm that:

- This work was done wholly or mainly while in candidature for a research degree at this University.
- Where any part of this thesis has previously been submitted for a degree or any other qualification at this University or any other institution, this has been clearly stated.
- Where I have consulted the published work of others, this is always clearly attributed.
- Where I have quoted from the work of others, the source is always given. With the exception of such quotations, this thesis is entirely my own work.
- I have acknowledged all main sources of help.
- Where the thesis is based on work done by myself jointly with others, I have made clear exactly what was done by others and what I have contributed myself.

Signed:

Date:

UNIVERSITY OF LATVIA

Abstract

Department of Physics
Faculty of Physics, Mathematics and Opometry

Doctor of Physics

Dynamics of spontaneously magnetized micro-filaments under an external magnetic field: Experimental investigation

by Abdelqader ZABEN

Micro-devices manipulated by an external force is an interesting topic of research in terms of potential applications, as for mixing in microfluidics and targeted cargo delivery in bio-medical applications. Magnetically actuated robots, as investigated here, give the advantage of both having on-demand motion control and safe bio-compatibility. In this work, the dynamics of magnetic filaments is investigated experimentally under both rotating and pulsed magnetic field. The filaments are made from ferromagnetic particles linked together by DNA fragments. The experiments were conducted under operating different conditions which allowed adequate comparison with numerical simulations results, identifies limitations in models developed in previous studies and gives a preliminary insight for using ferromagnetic filaments for mixing and as cargo delivery applications.

Acknowledgements

Foremost, I would like to express my deep gratitude to my scientific advisors Prof. Andrejs Cēbers and Dr. Guntars Kitenbergs for giving me opportunity to pursue my PhD and for their continues guidance and support in every aspect of this work.
Thanks go to all MMML group members, in particular Ivars Driķis for the useful discussions. I am also very thankful to Dārta Antāne for her generous help in the administrative paperwork.
A big thank you goes to my family, my parents for their continues support, to my brother Husni whom encouraged me to pursue a PhD and to Yasmin & Mamooni for their moral support.
Last but not least, the financial support from the European Union's Horizon 2020 research and innovation programme under grant agreement MAMI No. 766007.

Contents

To my parents

Majed Zaben
and
Hanan Abulaila

Chapter 1

Introduction

1.1 Motivation

Research on magnetically actuated micro-robots has become a topic of increasing interest in the past ten years (Koleoso et al. 2020), due to their potential applications, as for example, mixing (Biswal and Gast 2004; Chen and Zhang 2017; Shanko et al. 2019), targeted cargo delivery (Nguyen et al. 2021; Ahmed et al. 2017) and microrheology (Brasovs et al. 2015). Hence, understanding the dynamics of such devices in their operating environment became crucial from the point of view of feasibility, design and development. Self-propelling microdevices working in the realm of low Reynolds numbers is challenging object for research, since viscous forces exerted by the fluid dominates over inertial forces. When the inertia effects are negligible, the flow regime is reversible, as first experimentally realized by Taylor 1967. Purcell 1977, in his well known paper, *Life at low Reynolds number*, formulated 'the scallop theorem' addressing the issue of this reversibility on reciprocal motion to achieve propulsion and the way to overcome it by having more than one degree of freedom. Similarly for mixing in microfluidics, where momentum transfer is mainly dependent on molecular diffusion, local mixing is becoming important to enable lab on chip devices (Drew et al. 2016), considering the constraints of space and time for diffusion to take place. Such important potential applications in the field of biomedicine and microfluidics give the motivation to conduct this study.

1.2 Magnetic micro-chains

One design of devices actuated by external magnetic field, that have been commonly used in research, are chains consisting of connected micron size magnetic particles. This design gives the advantage of easy in-house manufacturing at a lab, as well as the flexibility to explore the dynamics of various configurations for preliminary studies. For example, as first published investigations for applications, chain of 1 μm paramagnetic particles, driven by oscillating transverse magnetic field (Dreyfus et al. 2005), was used to investigate the swimming behaviour with an added cargo. Moreover, chains made from 1.4 μm para-magnetic particles, propelled by a rotating magnetic field, were used to study the dynamics for mixing application (Biswal and Gast 2004).

A method to form the magnetic chains or filaments, as realized experimentally by Biswal and Gast 2003; Goubault et al. 2003, utilizes the streptavidin-biotin to bind the particles with special linkers. The magnetic particles are coated with Streptavidin and are linked with DNA fragments biotinylated from their both ends. The particles are aligned in chains by the application of a strong static magnetic field. Brownian motion ensures the motion of DNA fragments until they form bonds with particles. Eventually this results in the formation of flexible magnetic filaments. Their flexibility and physical properties can be adjusted by different parameters. For example, the increase of linker length increases the flexibility (Byrom et al. 2014). Moreover, the effect of varying chemical properties as PH and salt as investigated by Ērglis et al. 2008, can also vary the filament properties. Further details on the filament formation process is presented in chapter 2.1.

1.3 Filament dynamics

The dynamics of flexible magnetic filaments is interesting since their behaviour is governed by both magnetic and elastic forces. Under the action of static field applied in one dimension, paramagnetic filaments were found to either align with the magnetic field direction or deform having and S-like or U-like shape, as experimentally observed by Goubault et al. 2003. The resultant deformed shape is dependent on the filament length, were longer filaments tend to deform while shorter ones align with the field direction (Goubault et al. 2003). Such filament configurations have been also predicted numerically as presented by Cēbers 2003; Shcherbakov and Winklhofer 2004, showing that the transitional meta-stable U-like (hairpin) mode can be created under initial filament conditions, such as including a defect in the model for the filament.

Under the action of rotating field profile in a plane, the filament experiences a torque of magnetic origin which is opposed by hydrodynamic friction force as the result of the filament rotation (Spatafora-Salazar et al. 2021). At relatively low frequencies, for a filament made from super-paramagnetic

particles different rotational modes were observed experimentally, namely rigid, wagging (S-like shapes) and folding. The mode of rotation depends on the filament flexibility, while the filament may rotate synchronously or asynchronously with the magnetic field (Kuei et al. 2017). Transitional behaviour was investigated by applying a sudden relatively higher frequency rotating field, were an irreversible 2D compact structures were formed (Casic et al. 2010), from spiral formation on the filament both ends as the result of dissipative torques (Cēbers and Kalis 2011).

A theory that was adopted by several authors to model flexible magnetic filaments is based on the modified Kirchhoff rod theory to account for magnetic energy (Cēbers 2003; Barreto et al. 2022). The force and torque acting in the cross section of the rod are derived by energy variation which includes the elastic bending energy and energy of magnetic rod in an applied field (Cēbers 2003). In the case of ferromagnetic material, the magnetic moment per unit length of the rod $\vec{M}$ is antiparallel to the local tangent direction $\vec{t}$: $\vec{M} = -M\vec{t}$. The torque balance reads (Ērglis et al. 2010),

$$\frac{d\vec{K}}{dl} + \vec{t} \times \vec{F} - M\vec{t} \times \vec{H} = 0 \tag{1.1}$$

where $\vec{K}$ is the curvature. For the magnetic force gives $\vec{F}_m = M\vec{H}$. The balance of the viscous, elastic and magnetic forces reads

$$\vec{\vec{\zeta}}\frac{\partial \vec{r}}{\partial t} = -A_b \frac{\partial^4 \vec{r}}{\partial l^4} + \frac{\partial(\Lambda \vec{t})}{\partial l} \tag{1.2}$$

where $\vec{\vec{\zeta}}_{ik} = \zeta_\perp \delta_{ik} + (\zeta_\parallel - \zeta_\perp) t_i t_k$ is the matrix of hydrodynamic drag coefficients, Λ is the tension to sustain the inextensibility of the rod and A_b is the bending modulus.

The length is scaled with the length of the filament L, time with the elastic relaxation time $\tau = \zeta_\perp L^4 / A_b$, the elastic force by A_b / L^2. As a result, the behavior of the rod is determined by the magnetoelastic number $Cm = MHL^2 / A_b$ and $\omega\tau$, where ω is the angular frequency of the AC field.

The numerical algorithm is based on the construction of the projection operator projecting the configuration on the class of inextensible configurations. For that the rod is discretized by $\vec{r}_i, i = 1, ...p+1$ marker points (in simulations $p = 300$ for the most cases). For the inextensible rod there are p constraints $g_i = (\vec{r}_{i+1} - \vec{r}_i)^2 = h^2$. The constraints give $p \times 3(p+1)$ matrix $J_{ij} = \partial g_i / \partial \vec{r}_j$. Approximating the derivatives by finite differences, where the condition that ends are torque free $\partial^2 \vec{r} / \partial l^2 = 0$ is taken into account, the equation of motion introducing $3(p+1) \times 1$ column vectors $\vec{r}$ and $\vec{F}$ may be written as (J' is transposed matrix)

$$\frac{\partial \vec{r}}{\partial t} = \vec{\vec{\zeta}}^{-1} \cdot (\vec{F} + J' \frac{\Lambda}{2h}) \tag{1.3}$$

where $\zeta^{-1}_{ik} = \zeta^{-1}_\perp + (\zeta^{-1}_\parallel - \zeta^{-1}_\perp) t_i t_k$ is the mobility matrix. As a result of

discretization, the stiffness matrix A and $\vec{F}_k = \vec{F}^e_k = A_{k;l}\vec{r}_l$ are obtained. for $k = 2, ...p$ and $\vec{F}_{1,p+1} = A_{1,p+1;l}\vec{r}_l + Cm\vec{h}$ for $k = 1$ and $k = p+1$.

The condition of inextensibility $J \cdot \frac{\partial \vec{r}}{\partial t} = 0$ allows to express Λ as follows

$$\frac{\Lambda}{2h} = -(J\zeta^{-1}J')^{-1}J\zeta^{-1}\vec{F} \tag{1.4}$$

and the equation of motion reads

$$\frac{\partial \vec{r}}{\partial t} = (I - \zeta^{-1}J'(J\zeta^{-1}J')^{-1}J)\zeta^{-1}\vec{F} \tag{1.5}$$

Eq.(1.5) contains the projection operator $P = I - \zeta^{-1}J'(J\zeta^{-1}J')^{-1}J$. It is easy to check that $P^2 = P$. Eq.(1.5) is numerically solved by implicit scheme

$$\frac{\vec{r}(t+\Delta t) - \vec{r}(t)}{\Delta t} = P\zeta^{-1}(\vec{F}^e(t+\Delta t) + \vec{F}_m) \tag{1.6}$$

After each time-step redistribution of marker points is carried out to sustain their homogeneous distribution along the arclength of the filament's centerline.

This model was used to describe the dynamics of ferromagnetic swimmer (Belovs and Cēbers 2009), deformation dynamics under the action of the magnetic field inversion, where the filament was found to form a loop (Ērglis et al. 2010) and numerically to investigate the behavior under a rotating field (Goyeau et al. 2017), showing that the rotation can be either synchronous or asynchronous with the magnetic field depending on the rotational frequency. Moreover, the model was used for a magnetic rod with a fixed end (Wang et al. 2020).

1.4 Propulsion at low Reynolds number

As discussed in section 1.1, one of the main proposed bio-medical applications for micro swimmers driven by magnetic field is the ability of being propelled and navigated in viscous environment (Peyer et al. 2013). From the continuum theory of fluids based on mass and momentum conservation, a well known physical interpretation of the Reynolds number is the ratio between inertia and viscous forces terms in the Navier Stokes equations, which for incompressible flows with neglecting the bulk compressibility reads,

$$\nabla \cdot \vec{u} = 0 \tag{1.7}$$

$$\rho\left(\frac{d\vec{u}}{dt} + (u \cdot \nabla)\vec{u}\right) = -\nabla p + \mu\Delta\vec{u} + \rho\vec{f} \tag{1.8}$$

where ρ is the density, time t, $\vec{u}$ is the fluid flow and μ is the viscosity,

$$Re = \frac{\rho U l}{\mu} \tag{1.9}$$

and by scaling Eq.1.7 with the length and velocity scales l and U with $\hat{u} = \vec{u}U^{-1}$ and $\hat{r} = \vec{r}l^{-1}$ and by the definition of the Reynolds number, eq.1.7 reads,

$$Re\left(\frac{\partial \hat{u}}{\partial \hat{t}} + \hat{u}\cdot\hat{\nabla}\hat{u}\right) = -\hat{\nabla}\hat{p} + \hat{\Delta}\hat{u} + \hat{f} \tag{1.10}$$

The left terms in Eq.1.10 consists of the inertia terms having the convective and dynamic acceleration terms $u \cdot \nabla u$ and $\frac{du}{dt}$ respectively and the right hand terms ($-\nabla p + \mu\Delta\vec{u}$) represents the viscous forces. Taking the limit $\lim_{Re\to 0}$ Eq.1.8 & 1.7 reduces to Stokes equations as follows

$$\mu\nabla^2\vec{u} = \nabla p - \vec{f} \tag{1.11}$$

$$\nabla\cdot\vec{u} = 0 \tag{1.12}$$

Stokes equations are linear and with the absence of time dependence, it gives the property of Stokes flows to follow perfect reciprocal motion (Lauga and Powers 2009), which results in no net displacements. Therefore, the displacements of the micro swimmer at low Reynolds number environment is solely dependent on the geometrical configurations over time, not the frequency of the reciprocal motion. This is referred as the scallop theorem (Purcell 1977), which states that the body should have more than one degree of freedom in order to achieve propulsion. It should be noted here that the term 'swimmer' is used here for devices which are actuated by internal energy, or by the application of an external force or torque. Another term is used in literature as a 'propeller', while 'swimmer' is donated to microorganisms (Lauga and Powers 2009). Stokes equations are derived assuming that the Reynolds number is very small ($Re \approx 0$), however small inertial forces depending on the swimmer shape and size may contribute in breaking the time reversal symmetry and allow propulsion. Moreover, the symmetry can be also broken in non-Newtonian fluids, in visco-elastic fluids as an example (Peyer et al. 2013).

For self propelling filament like swimmers similar to spermatozoa, the propulsion at low Reynolds number is achieved by the shape change as a results of local hydrodynamic interaction differences across its deformed flagella or filament. This showed through resistive force theory the importance of anisotropy of hydrodynamic drag, by considering the difference in the the drag coefficients acting along ($\zeta_{\parallel}$) and perpendicular ($\zeta_{\perp}$) to the filament are required to achieve propulsion. The instantaneous drag acting on the filament per unit length $\vec{f}(s,t)$, given by the tangent local angle dynamics (s,t) as a function of space and time reads (Lauga and Powers 2009),

$$\vec{f}(s,t) = -[\zeta_{\parallel}\vec{t}(s,t)\vec{t}(s,t) + \zeta_{\perp}[1 - \vec{t}(s,t)\vec{t}(s,t)]]\cdot\vec{u}(s,t) \tag{1.13}$$

where $\vec{u}$ is the local velocity of a point on the filament relative to the surrounding fluid as a function of arc length s and time t. For an asymptotically

slender filament with a length L and radius a, where L/a tends to ∞, the parallel ($\zeta_{\parallel}$) and perpendicular ($\zeta_{\perp}$) drag coefficients can be expressed as (Lauga 2020),

$$\zeta_{\parallel} = \frac{2\pi\mu}{\ln(L/a)} \tag{1.14}$$

$$\zeta_{\perp} = \frac{4\pi\mu}{\ln(L/a)} \tag{1.15}$$

As the radius a tends to zero, a maximum ratio of $\zeta_{\perp}/\zeta_{\parallel} \approx 2$ can be achieved theoretically, and this ratio is lower for real slender bodies with finite dimensions (Yang et al. 2017). Several theoretical models have been presented to estimate the anisotropy of hydrodynamic drag coefficient for a rod like objects, for example; bead model consisting of touching N number of beads (Yamakawa and Tanaka 1972) and cylinder model (Batchelor 1970). The comparison of estimates between different theoretical models is recently presented by Yang et al. 2017.

In studies of microswimmers, far-field velocity become important to consider especially if the swimmer is interacting with another object, for example, a wall boundary or with other swimmers. A fundamental solution of velocity fields $\vec{u}(r)$ for (eq. 1.11, 1.12) can be obtained by Green's function $\mathbf{G}$, as $|u| \to 0$ when $r \to \infty$, by,

$$\vec{u}(r) = \vec{F} \cdot \mathbf{G}(\vec{r}) \tag{1.16}$$

where $\vec{F}$ is a point force applied locally at the origin and $\mathbf{G}\ (\vec{r})$ is defined as,

$$\mathbf{G}(\vec{r}) = \frac{1}{8\pi\mu}\left(\frac{\mathbf{I}}{r} + \frac{\vec{r}\vec{r}}{r^3}\right) \tag{1.17}$$

$\mathbf{G}(\vec{r})$ is a tensor field, known as the Oseen tensor, where r is $|\vec{r}|$ and $\mathbf{I}$ is the identity tensor. The fundamental soultion of a single point source at the origin, known as stokeslet, where in this case u decays spatially as $1/r$. Since Stokes equations are linear, it is possible to obtain the velocity field by superposition principle of several stokeslets by,

$$\vec{u}(\vec{r}) = \int \vec{f}(\vec{r'}) \cdot \vec{G}(\vec{r} - \vec{r'})d\vec{r'} \tag{1.18}$$

where $\vec{f}$ is the fluid force density. For most of swimming cells, the far field velocities u decays spatially as $1/r^2$, resulting in a force dipole flow fields. The force dipole is arised from the local hydrodynamic forces produced by the flagella as they swim, opposed by the drag of moving cell body acting in the opposite direction (Lauga 2020). Hence, understanding the system is necessary to solve Stokes equations using method of superposition of fundamental solutions. Here as presented in chapter 5, the far field velocity was found experimentally to have a decay spatially as a function of $1/r^2$, for a filament under a rotating field.

Another aspect to consider in the propulsion of microswimmers, is the direction or the signature of the flow fields relative to the swimmer. The term 'pusher' is used when the driving flagella is used to push the cell body through the surrounding fluid. 'Puller' swimmers, for which the flagella are located in the front of the cell body, pull the surrounding fluids while the cell body is dragged along its sides. For example, spermatozoa and Chlamydomonas reinhardtii represent the types of pusher and puller configurations respectively. The resultant velocity fields are similar, however the direction of the flow is the opposite. In equation 1.9, Re is defined as a function of the characteristic velocity U. Another interpretation of Re is defined as a function of driving frequency, referred as oscillatory Reynolds number Re_ω (Lauga 2020),

$$Re_\omega = \frac{\rho L^2 \omega}{\mu} \tag{1.19}$$

The magnitude of oscillatory Reynolds number is higher than Re calculated using Eq.1.9 when operating at low Reynolds number environments. For example, a difference of 2 order of magnitude for bacterium swimming at Re $\approx 10^{-4}$, and is lower or equal for swimmers operating at Re $> 10^{-1}$ (Lauga 2020).

The design of magnetic artificial swimmers are often inspired by microorganisms, that use a bending or rotating flagella to propel. The design of such devices is complex and capturing the propulsion mechanism from nature can help keeping the complexity minimal (Peyer et al. 2013). Examples of designs for artificial swimmers driven by magnetic field are shown in Fig.1.1. Such as, a flexible beating flagella similar to spermatozoa motility mechanism driven by an oscillating magnetic field (Dreyfus et al. 2005; Pak et al. 2011), shown in Fig.1.1(a), helical structures similar to *E.coli* bacterial flagella driven by a rotating magnetic field (Zhang et al. 2009a; Tottori et al. 2012) (Fig.1.1(b)), artificial cilia made using flexible chains of para-magnetic beads, as shown in Fig.1.1(c & d) and driven with a rotating magnetic field (Vilfan et al. 2010). Here as presented in chapter 4, we study a new propulsion mechanism, which is similar to Chlamydomonas reinhardtii micro algae.

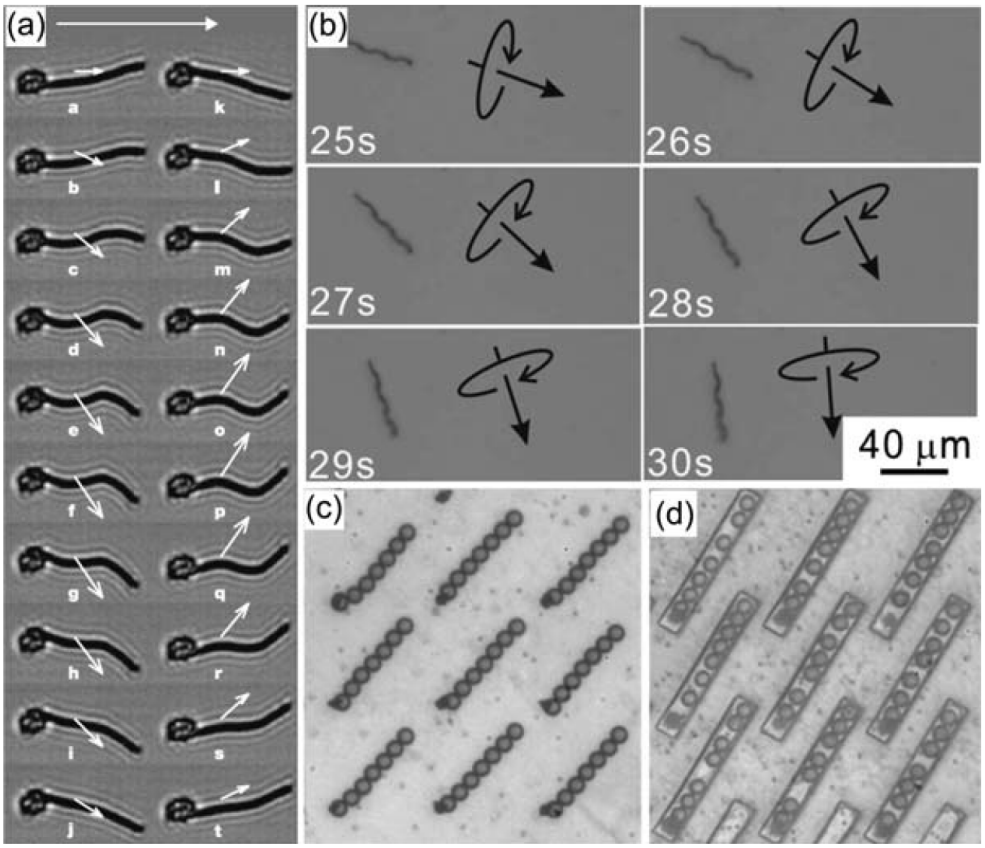

FIGURE 1.1: Example of magnetic driven microswimmers presented in the literature: (a) flexible tail made from paramagnetic particles attached to a blood cell driven by an AC field. (b) helical swimmer, made from a helical tail attached to a magnetic bead driving by a rotating field. (c) shows assembled chains of paramagnetic particles fixed from one end, representing artificial magnetic cilia. (d) shows the formation process of the filaments used in (c), by the use of rectangular trenches and the application of a static field. (source: Peyer et al. 2013)

1.5 Particle image velocimetry (PIV)

Particle image velocimetry (PIV) is an optical non-intrusive technique used to characterize the flows both quantitatively and qualitatively. The fundamental principles of a PIV system consists of the following (Raffel et al. 2007):

- **Seeding**: tracer particles are added to the flow or system. They have to be small enough not to influence the phenomenon of interest. As a result of their reflections, the flow can be quantified over time based on their locations.
- **Light source**: the added tracer particles are exited by a light source, which can be either a mono wavelength source (laser beam) or multi-wavelength source. This improves their contrast in the short exposure times used in experiments. Particles can be fluorescent, allowing a selective visualisation. Moreover, these tracer particles can be either illuminated in a desired plane area (light sheet) or by illuminating the volume. In micro-flows which are observed under microscope, the volume is illuminated. Such a measurement technique for micro-flows is often termed in the literature as μ-PIV.
- **Image acquisition**: to detect tracer particle locations in time. For this exposure time is important and has to be short enough not to allow blurring of particles. Also precise timing of image acquisition is important for further calculations.
- **Velocity computation**: image analysis methods (typically cross correlation) are used on the recorded images to obtain the displacements of particle ensembles within two images.This is done for multiple parts of the image, called interrogation areas, typically obtaining a set of displacements, from which velocities can be calculated using the measured time between the images.
- **Results validation**: the calculated velocity fields are generally validated by different tools. For example, errors associated with the cross-correlation solution method that is used.

The quality of PIV experiments are typically evaluated by the measure of errors associated with cross correlation method and used tools. This requires considerations of the tracer particle concentration per interrogation areas, to have a minimal noise to signal ratio. Moreover, the tracer particles should be able to follow with the flow at the shortest time delay. From Stokes equation, the velocity lag (U_l)between the particles and the flow can be calculated by (Raffel et al. 2007),

$$U_l = d_p^2 \frac{\rho_p - \rho}{18\mu} a, \tag{1.20}$$

where a is acceleration, d_p is the tracer particle diameter, ρ and ρ_p are fluid and particle densities respectively, μ is fluid viscosity. Assuming that the

density of the tracer particles is close to the density of the fluid, the lag velocity (U_l) is a function of d_p^2. Hence using particles of lower size is more desired to obtain accurate measurements. Moreover, smaller tracer particles increase the spatial resolution by having more particles per interrogation areas. However, by using smaller tracer particles in micro systems, the particle displacements are distorted due to the Brownian motion and may interfere with the measurement quality. The effect of particle displacements due to the Brownian motion can be evaluated by calculating Stokes number Stk, defined as Raffel et al. 2007,

$$Stk = \frac{\tau_p}{\tau_f}, \tag{1.21}$$

were τ_p is the tracer particle response time defined as $\tau_p = d_p^2\ \rho_p/18\ \mu$ and τ_f is the characteristic time of the flow. A value of $Skt << 1$ is desirable to consider in setting the experiments.

1.6 Mixing at low Reynolds number

By considering the definition of Reynolds number (Eq.1.9) in microfluidic devices, the characteristic length L and velocity U are relatively small. Hence, mixing is mainly dependent on the molecular diffusion due to the absence of turbulent chaotic flow. However, molecular diffusion for some applications is too slow and inefficient in the scale of hundreds of microns for mixing to take place (Shanko et al. 2019). Several designs have been developed to enhance the mixing rate at low Reynolds number regimes. This can be achieved by changing the device geometry, termed as passive micromixers, to enhance both chaotic advection by the addition of obstacles or by increasing the interfacial area between the fluids. For example, a spiral shaped channel geometry as presented by Sudarsan and Ugaz 2006, whom showed that mixing will occur at shorter distances downstream the channel compared to straight channels. or by adding diamond-shaped obstructions to increase the chaotic advection by breaking and recombining the flow within the channel (Bhagat et al. 2007).

Another way to enhance the chaotic advection and breakup flows is by the introduction of external forces, known as 'active mixing', which can be done by the application of pressure, temperature, acoustic and magnetic gradients (Shanko et al. 2019). Magnetic chains or rods driven by a rotating magnetic field (microstirrer) have showed to be a good choice with an achievable mixing efficiency up to 92 % (Cai et al. 2017). Under a rotating field, the magnetic torque is expressed by,

$$\vec{T} = \vec{M} \times \vec{B} \tag{1.22}$$

Where $\vec{M}$ is the magnetic moment per unit length of the chain and B is the magnetic field strength. The mixing efficiency can be evaluated by Mason

number Ma, which is ratio of viscous forces to the magnetic forces, defined under the application of magnetic torques by (Shanko et al. 2019),

$$Ma = \frac{16\eta\omega}{\mu_0\chi^2 H^2} \tag{1.23}$$

where η is the viscosity, ω is the angular velocity, μ_0 is the permeability of free space, χ is the dimensionless susceptibility of the magnetic particles and H is the magnetic field strength. For mixing applications, Mason number is used to characterize between the contribution of mixing due to advection relative to diffusion. Hence, higher Ma results in a higher mixing effectiveness, with the value of Ma is > 1, mixing is dominated by advection. When a magnetic rotating field is applied, the particle chain rotates with angle ϑ between its magnetic moment and the field direction. The critical angular velocity ω_c can be obtained when the viscous drag torque is equal to the magnetic torque. For rigid linked particles, rotations when angle $\vartheta < 90$ is synchronous with the magnetic field (Kang et al. 2007).

For angular velocities above ω_c, the filament breaks into smaller filaments. This was observed experimentally by Kang et al. 2007, characterized when operating at ($Ma > 0.002$). To increase the flexibility and avoid breakage of the filament, elastic linkers such as the DNA fragments can be used to link the particles.

1.7 Magnetic properties

The magnetic properties of a material can be defined based on its behaviour under a magnetic field - as a ferromagnetic, paramagnetic or diamagnetic material. The magnetic properties are determined by the net magnetic moment of the material. At atomic scale, if the magnetic moment across the material orients randomly in a way to have zero net magnetization, the material is referred as paramagnetic. In the case of a ferromagnetic material, larger volumes or domains within the material have a magnetic moment in the same direction, which results in a net permanent magnetization (Rikken et al. 2014). When a magnetic field is applied, the magnetic moment of the material domains try to align with the magnetic field direction, until reaching the maximum magnetic moment per unit volume (saturation magnetization M_s), where the material magnetic moment vector is aligned with the magnetic field direction. Below M_s, a difference of angle between the magnetic moment and the magnetic field direction occurs, referred as magnetic anistropy. Studies of magnetic particles manipulated by an external magnetic field are either conducted using ferromagnetic or paramagnetic particles (Xu et al. 2021).

To highlight the main difference, ferromagnetic particles behave differently when the field is switched off, a residual magnetization is present, while paramagnetic particles have a zero net magnetization (Rikken et al. 2014). Moreover, ferromagnetic material gives a higher response to external field. In this work, ferromagnetic particles are used. Their magnetic properties have been previously measured through vibrating sample magnetometer (VSM), as presented by Ērglis et al. 2010. The magnetization curve is shown in Fig.1.2.

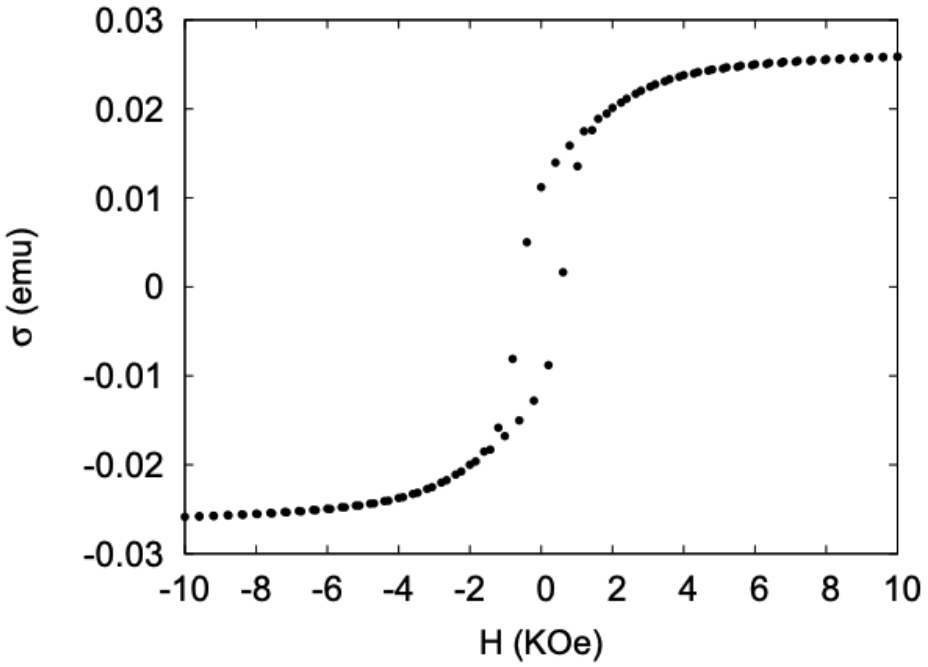

FIGURE 1.2: Magnetic moment of the diluted sample of core-shell ferromagnetic particles in dependence on the magnetic field. (source: Ērglis et al. 2010)

1.8 CGS unit system

In the following chapters, calculations of the material magnetic properties were made based on centimeter-gram-second (CGS) unit system, which is preferred by MMML (Laboratory of Magnetic Soft Materials) research group in contrast with the International System of Units (SI). Different views have been presented on the advantages of using CGS *emu* (electromagnetic) units when compared SI. For example, the value of the permeability of vacuum μ_0 in CGS is 1, which avoids the confusion in referring the field strength H as B, where $B = \mu_0 H$ and $\mu_0 = 4\pi \times 10^{-}7N/A^2$ in SI units. However, working with SI units give the advantage of uniting both electrostatic (*esu*) and (*emu*) units. More on the comparison of units systems in Electromagnetism is presented by Goldfarb 2018. The following table 1.1 presents the factors to convert cgs to SI units, for the parameters which are used in this work.

Note that *emu* is an indication that electromagnetic units is used, which is equivalent to erg/G.

Conversion between cgs and SI units			
Quantity	**cgs units**	**S.I. Units**	**Conversion factor to SI**
Magnetic Flux density B	Gauss	T	10^{-4}
Magnetic field strength H	Oe	Am^{-1}	$10^3/4\,\pi$
Magnetization M	$emu\ cm^{-3}$	Am^{-1}	10^3
Energy E	erg	J	10^{-7}
Dynamic viscosity η	P	$Pa \cdot s$	10^{-1}

TABLE 1.1: Conversion factors between cgs and SI units

1.9 Thesis overview

The main aim of this thesis is to experimentally investigate the dynamics of semi-flexible magnetic chains, made of ferromagnetic particles linked by elastic polymers, under various magnetic field profiles. This work is proposed to fill research gaps in the literature available in the public domain, where the focus in this field is mainly oriented in using para-magnetic particles, by trying to answer the following questions,

- How do the filaments behave under a rotating magnetic field? When sweeping through field frequencies, can one observe a change in the behavior of the filament with a characteristic critical frequency?
- Can a ferromagnetic filament propel under a periodic field inversion profile, as numerically proposed by Belovs and Cēbers 2009?
- What are the flow characteristics around the filaments under a rotating magnetic field?

In chapter 2, the synthesis procedures of the filament formation is first presented, we also discuss here about the limitations and problems encountered by using this formation method. In Section 2.2 and 2.3 the experimental setup is described for video microscopy based analysis and μ-PIV measurements methodology respectively.

The structure of chapters 3, 4 & 5 is sectioned as following,

- Experimental procedures
- Processing and data analysis methods
- Comparison between experimental with numerical simulations results and result discussion

The numerical simulation results were obtained from the model, as presented briefly in Section 1.3, using Matlab program which has been previously developed by MMML group. More details on the numerical algorithms

can be found in (Ērglis et al. 2010; Goyeau et al. 2017).

In chapter 3, the results showing the filament behaviour under a rotating magnetic field are presented, which is divided into two sections. In 3.1: the dynamics when operating at frequencies where the magnetic torques are higher that the viscous torques. Some of the results presented here have been previously communicated in the publication (Deformation of flexible ferromagnetic filaments under a rotating magnetic field, Zaben et al. 2020a). In section 3.2, the results obtained when operating at a higher field frequency are presented, which were communicated through the publication (3D motion of flexible ferromagnetic filaments under rotating magnetic field, Zaben et al. 2020b).

In chapter 4, we present the results obtained for the filament dynamics under a pulsed magnetic field, which represents the application use of filaments as micro-swimmers. A part of the results presented in this chapter have been previously communicated in the publication (Instability caused swimming of ferromagnetic filaments in pulsed field, Zaben et al. 2021). In chapter 5, we present the local velocity measurements around the filaments under a rotating field, analysis methods and discuss about the optimal mixing efficiency operating conditions. Finally, the conclusions from this work and further work suggestions are presented in chapter 6.2.

Chapter 2

Experimental methodology

In this chapter, the experimental set-up and methods used for producing the results in subsequent chapters will be presented. In the first section, the filament formation method will be presented, followed by the experimental setup. In section 2.3, the setup for velocity measurements is presented.

2.1 Filament formation

Throughout this work, the method used to form filaments was adapted from the work done by K. Ērglis 2010. The filament is formed by linking magnetic particles with DNA fragments. The ferromagnetic particles used are supplied by Spherotech, with the mean diameters of 4.21 μm and 4.39 μm for the lots used. These particles are made of polystyrene, which is coated with a thin layer of chromium oxide and afterwards functionalized with streptavidin. The DNA fragments are supplied by the Latvian Biomedical Research and Study Centre, which are 1000 base pair (bp) long and biotinylated on both their ends. The resultant Streptavidin-biotin is strong in-terms of binding strength and has widely been utilized for applications as in biochemical sensing (Liu et al. 2016).

The synthesis procedure is as follows,

- First, 10 μL DNA fragment solution (182 ± 10 μg/ml) was mixed with 2 ± 0.5 μL magnetic particles (1% w/v) and 0.5 ml 10 % TE buffer solution (made by mixing 7.5 pH TE buffer solution with distilled water) in 1.5 - 2 ml test tubes.
- The test tube is then placed between two strong permanent magnets, made from a Neodymium alloy. Dimensions of each magnet are $5\ cm \times 5\ cm \times 1\ cm$. Magnets are fixed at 7 cm apart and can provide a homogeneous field of $\approx$ 500 Oe.

A schematic diagram showing the filament formation mechanism is shown in Fig.2.1. The resultant DNA and particle mass concentration in the sample is 6 nM and 0.004% w/v respectively. This concentration results in an average of $\approx 8 \cdot 10^6$ DNA fragments to bind with each particle in the sample.

The maximum ability of a particle to bind with DNA is $\approx 2 \cdot 10^7$, as calculated

by Ērglis 2010, where the DNA molecular weight is $M_{DNA} = 607.4N_{nucliotides} + 157.9$. Since the main interest is the formation of chains, the desired areas of linkage are the parts covered between aligned two particles. The working DNA to particle ratio was found to be good for this study, since it was observed to have a relatively low probability of particle clusters formation.. It is about one order of magnitude lower than to cover the whole particle. Using this synthesis method, the formed filament length has a wide distribution, where we observed chains ranging from three particles in length to 130 μm.

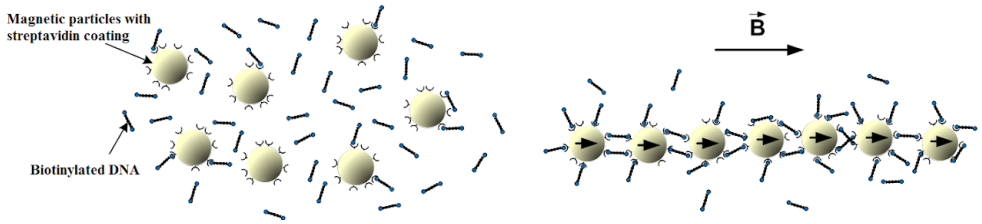

FIGURE 2.1: Schematic representation of the filament formation, Ērglis 2010

Different parameters are responsible for the resultant structures or shapes formed using this method. Such as, magnetic field strength, DNA length and particle size. The magnetic field strength used in the formation process can be varied by having an adjustable track, as shown in the illustration in Fig. 2.2. The effect of magnetic field strength on the formed length was previously investigated by Belska 2018, using similar particles size and DNA fragment length. There, is was found that reducing the distance between the magnets results in the formation of longer chains. However, the increase of the field strength will also result in the increased probability of particle aggregations. An adequate study showing the effect of particle size and DNA length on the formation process was not done on ferro-magnetic particles so far. However, it was observed by Ērglis 2010, that using 465 bp long DNA fragments did not result in chain formation using this synthesis method.

Other formation procedures have been proposed in the literature. For example, Byrom et al. 2014 investigated the formation criteria of super-paramagnetic particles using DNA fragments of various lengths. For them the filaments were prepared in a thin fluidic chamber placed on a hot plate for 1.5 hours, while a lower field strength (19G - 275G) was applied. Since this study is concerned about preliminary investigation of the dynamics using individual filaments, literature gaps in the filament formation mechanism and process, such as synthesis of desired length, were out of the scope. However, it is proposed that several research areas in the formation of ferromagnetic filaments are yet to be potentially investigated. Examples of shapes observed using this formation method are shown in Fig. 2.3 and range from straight filaments (a) to conjoining of two filaments (b), aggregated particles (c) and non-linked particles (d).

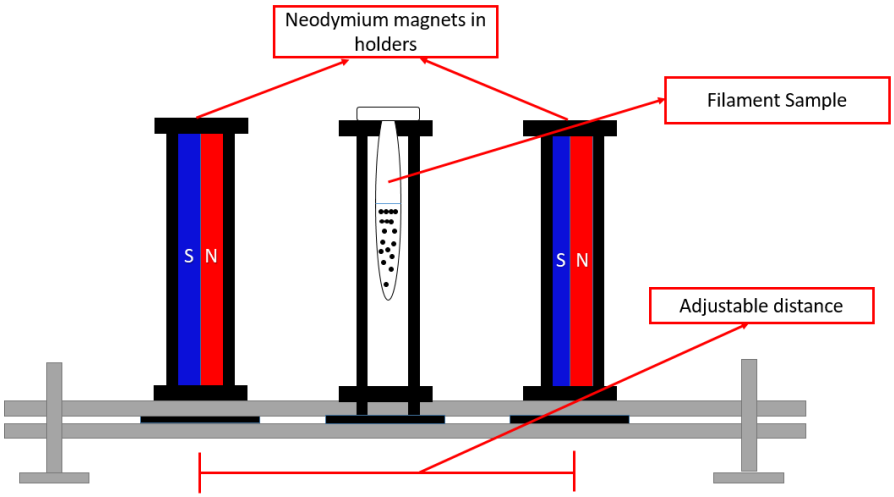

FIGURE 2.2: Schematic illustration showing the experimental setup for filament synthesis in a strong magnetic field.

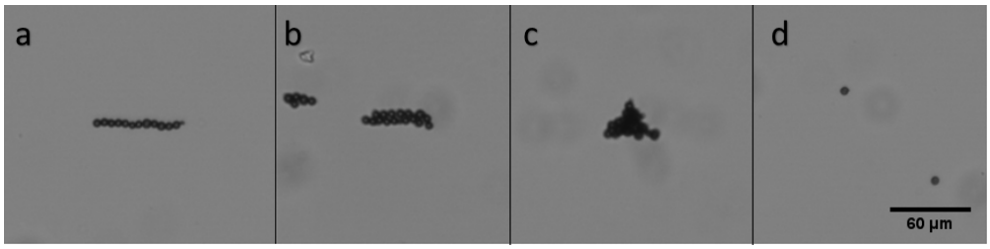

FIGURE 2.3: Example of shapes observed with the application of a static field in the horizontal direction.

2.2 Experimental setup and tools

The experimental setup consists of the following components (shown in Fig.2.4),

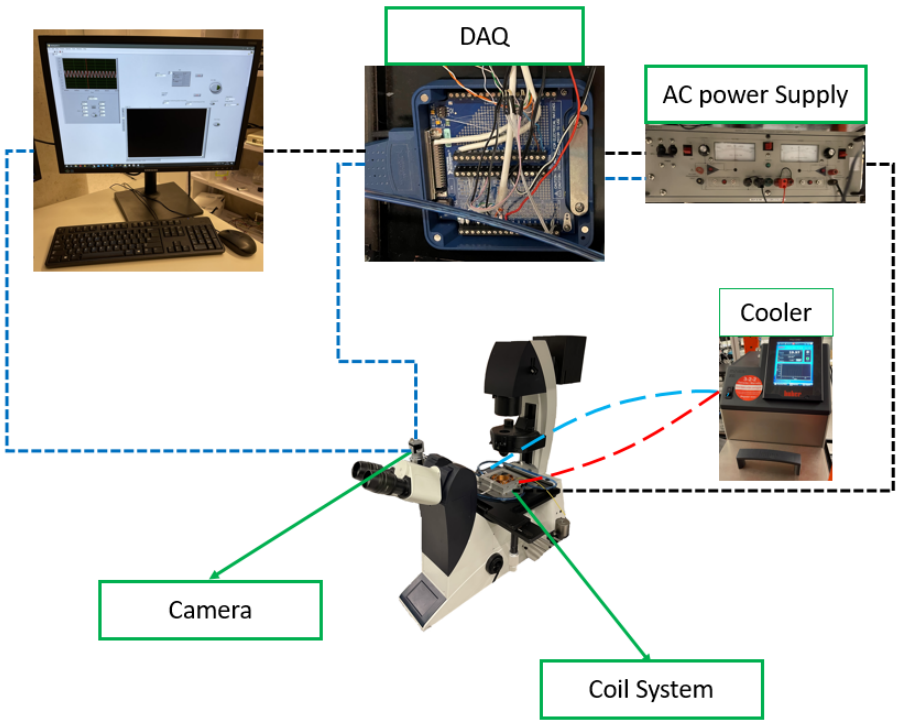

FIGURE 2.4: Experimental setup

- **Microscope**: For sample observation, an optical (Leica DMI3000B) microscope was used, under both (40×, NA = 0.8) and (10×, NA = 0.25) in bright field mode.
- **Camera**: The images were acquired by Basler ac1920-155um camera, which has a grayscale CMOS sensor and can deliver up to 200 frames per second. Image acquisition was controlled by either fixing the frame rate or by an external trigger mode, depending on the desired goal.
- **Coil system**: The magnetic field was generated using an in-house built coil system (schematic is shown in Fig.2.5). It consists of three coil pairs, which are capable of providing any magnetic field configuration in three dimensions. The coils are powered by three AC power supplies (Kepco BOP 20-10M), which can provide currents up to 7 A and frequencies up to 50 Hz. Two pairs of coils are cooled with a heat exchanger (Huber ministat 230) through fluid circulation. The coil system is capable of producing a maximum magnetic field of 51 Oe.
- **System control**: The desired magnetic field strength and profile is first defined by a LabVIEW code. This defined signal is then sent to the

power supplies through National Instruments data acquisition (DAQ) card (NI PCI-6229). The power supplies are set to the current control mode, which supplies the current based on the voltage input from the signal sent, where 1 V corresponds to 1 A. The camera is synchronized with the system in two ways. In one case it receives a pulsed digital input signal through the DAQ card. Using the camera trigger mode setting, images are acquired at a desired magnetic field direction, predefined in the LabVIEW code (The LabVIEW code is shown in Appendix B.1). The other way of synchronization is a continuous reading of the magnetic field. In this case current values from the power supplies are measured by a voltage drop on resistors of known resistance. By defining a fixed frame rate acquisition mode, a pause trigger by a signal sent from the camera is used to record the field values based on the images acquired. The program code used in this case is shown in Appendix B.2.

- **Fluidics**: The fluidic cells used in experiments are placed in the coil system. Cells are made by using two square microscope glass slides and a 211 μm double-sided adhesive tape. A square of 1×1 cm cut is made in the middle of the tape, which results in a volume capacity of $\approx$20 μl. Using micropipettes, such amount is added from the prepared filament sample for observation.

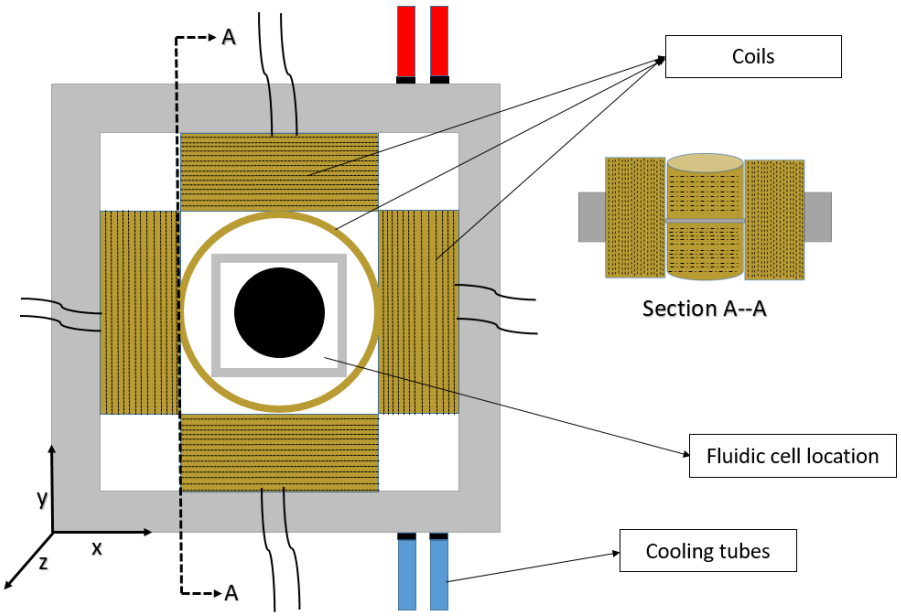

FIGURE 2.5: Schematic illustration of the coil system

2.3 PIV experimental setup

Similar to the filament synthesis procedures presented in section 2.1, 30 μl of ≈ 0.53 μm tracer Nile red fluorescent particles (Spherotech) are also added to the tube before adding magnetic particles and DNA and placing the sample between the magnets. To reduce the tracer particle aggregation probability, 10μl of 0.01% SDS (Sodium Dodecyl Sulfate - a surfactant) was added to the sample. It is also sonicated for 30 min before adding the magnetic particles and DNA fragments. A schematic illustration of filament formation for velocity measurements is shown in Fig.2.6. From experimental observations it should be noted that a careful concentration of SDS should be used. A higher concentration will result in adherence of the fluorescent dye of the tracer particles to the magnetic particles in a short time.

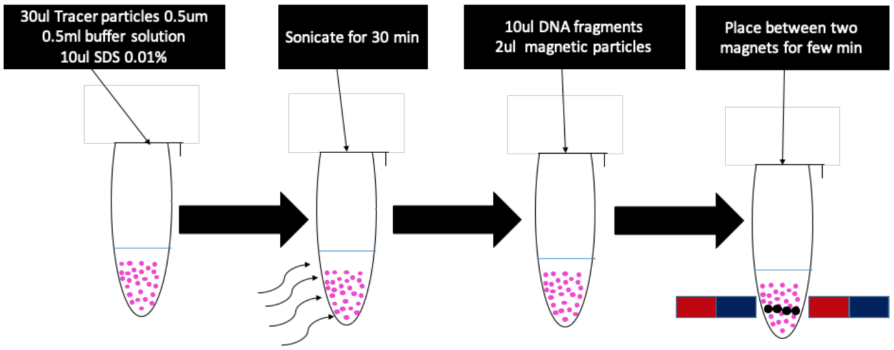

FIGURE 2.6: Schematic illustration of filament formation method used in velocity measurements

The tracer particle concentration was determined initially by following an approximation (Kiger 2010),

$$N_1 = \frac{C\,\Delta z}{M_0^2}\,D^2, \tag{2.1}$$

where C is the particle concentration, Δz is the thickness in the z-axis illuminated, D is the size of the interrogation region, M_0 is the magnification and N_1 is the desired number of particles in the interrogated regions. The choice of the interrogation region size, often called as window size, is based on the signal to noise ratio obtained from a cross correlation map, which also allows to specify the spatial resolution. An average 10 or more particles, up to 25, are desired to obtain accurate measurements, as presented in literature (Raffel et al. 2007). More details on the effect of particle concentration will be presented in chapter 5. By having the initial calculations, the working tracer particle concentration was chosen and then fine-tuned based on a trial and error process in experimental observations in order to have the maximum particle per window while taking into account the possible particle aggregation that may occur as a result of higher concentrations used. The optimal

concentration was found to be approximately 2 times higher than the one estimated in using eq 2.1.

The μPIV setup used in this study is made by Dantec dynamics and consists of the following (as shown in Fig.2.7):

- **Camera**: HiSense MkII camera is used for images acquisition. It has a special CCD sensor, which allows to operate in a double frame mode, with a maximum frame rate of 12.2Hz and a minimum inter frame time 200 ns. Hence, an effective acquisition rate between two consecutive images in the double frame mode can reach five million frames per second (fps). Images are saved via Dynamic Studio software and can be later exported.

- **Light source**: The light source used to excite the tracer particles is a double pulsed YAG laser, capable of producing mono wave-length light pulses with a wave length $\lambda = 532$ nm at a maximum frequency of 50 Hz. The choice of nile red florescent particles was based on the maximum excitement wave length of the florescent (λ = 532 nm) given by the manufacturer's specification. This results in the reduction of the image noise to signal ratio and enhances the quality of the velocity measurements.

- **System control**: The camera and the laser are synchronized by a timer box (NI PCI-6602) through the Dantec dynamic software Dynamic Studio .

- **Microscope**: An inverted optical microscope (Leica DM-ILM) is used for sample observation. We use Y3 filter cube in which the filters of excitation and emission light emitted from laser and tracer particles have ranges of 535 $\pm$50 and 610 $\pm$75 respectively. 40x objective with NA=0.8 is used here.

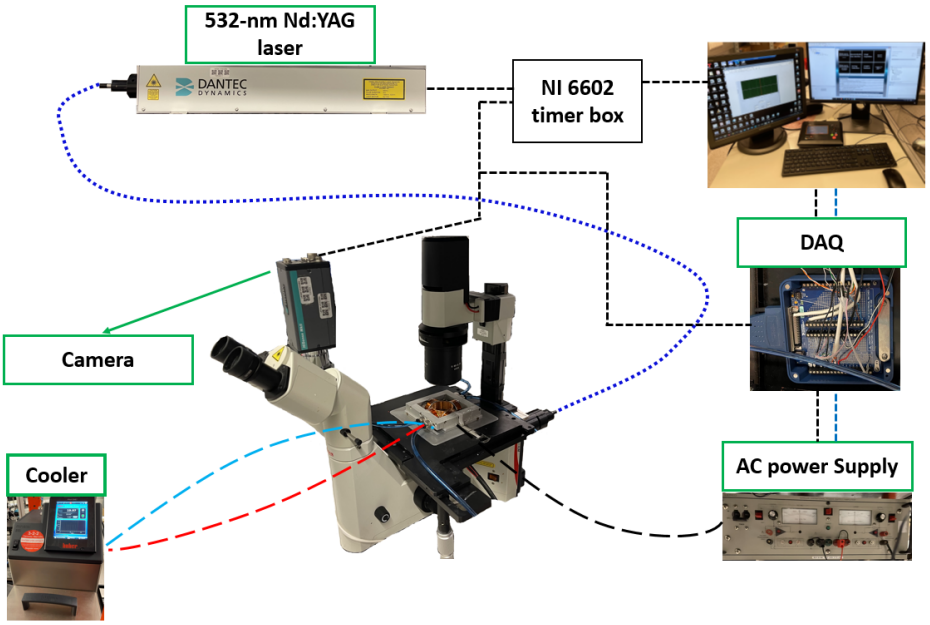

FIGURE 2.7: Experimental setup for velocity measurements

Chapter 3

Filament dynamics under a rotating field

In this chapter, the experimental procedures and filament behaviour under the application of a rotating magnetic field will be presented. The filament under this field profile was found to undergo two regimes: a 2D in-plane rotation at frequencies below a critical value f_c (presented in section 3.1) and in a 3D motion for higher frequencies (Section 3.2). The results presented in this chapter have been communicated via two publications (Zaben et al. 2020a; Zaben et al. 2020b), which are added in appendix A.

3.1 Behaviour at low frequency ($f < f_c$)

3.1.1 Experimental Procedure

The experiments were conducted as following: the fluidic cell containing the filament solution, prepared as presented in chapter 2, is placed under the microscope for observation. A static magnetic field of $H = 17.2$ Oe in an arbitrary direction is applied first for a few minutes, to allow the filament to align with the field direction and connect any nearby free particles to the filament, which may have been disassembled during the transfer process. A rotating field in the $x - y$ plane is then applied, defined in the Labview code as two sine profile signals with one having a phase shift of 90 degrees. The images were acquired by setting the camera in an external trigger mode, defined to capture a single frame per period when the magnetic field direction is pointing in the y-direction. The experiments were repeated at a range of both magnetic field strength $H = 6$ Oe - 25 Oe and field frequency $f = 0.1$ Hz - 8 Hz.

Examples of the observed filament shapes are shown in Fig.3.1. In these experiments the field strength is fixed while the frequency is varied for two filaments of different lengths. It is observed that operating at higher frequencies increases the filament deformation, as visible in images (a-d) and (A-D), with a resultant 'S'-like shape deformation, while having the filament tips pointing opposite directions. This increase of frequency also induces a larger observable lag of the central part of the filament with respect to the magnetic field direction, which is pointing upwards. Finally, it was also observed that

at at a certain frequency the filament tip moves out of the focus plane, as visible in Fig.3.1(d). The angle between the central part of the filament and the magnetic field is nearly perpendicular.

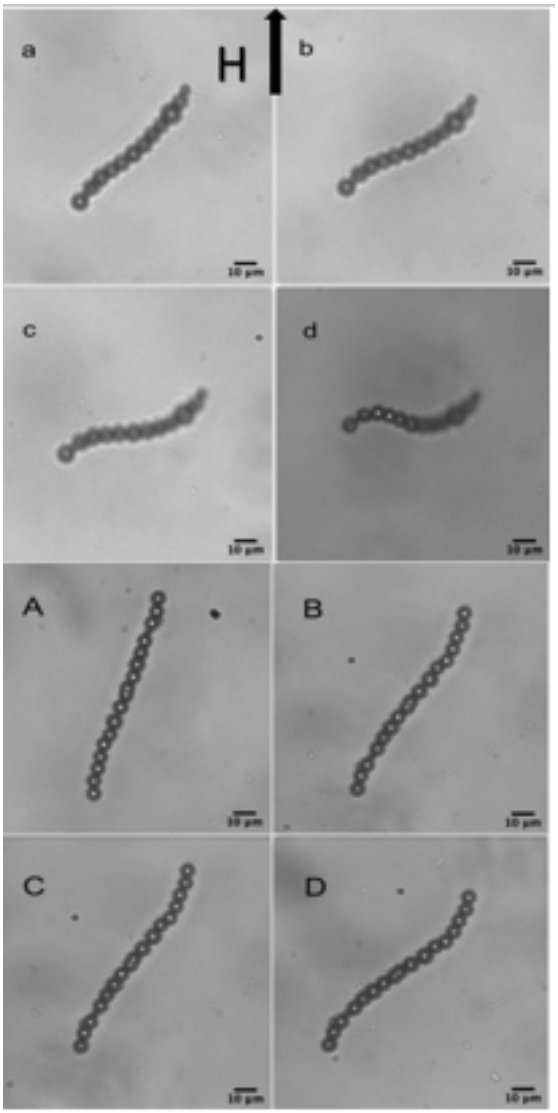

FIGURE 3.1: Examples of the observed filament shapes under a rotating magnetic field of strength $H = 8.6$ Oe. Filament with $L = 50.5$ μm at (a) 1 Hz, (b) 1.5 Hz, (c) 2 Hz and (d) 3 Hz. Filament with $L = 67.4$ μm at (A) 0.2 Hz, (B) 0.3 Hz, (C) 0.4 Hz and (D) 0.6 Hz.

3.1.2 Image processing

The filament deformation here is characterized by measuring the angle between the magnetic field direction and the tangent angle at the filament centre ϑ. To do so, the images were processed in Matlab with the following steps. The particle centres were found using circular Hough transform function (Atherton and Kerbyson 2001). Then the filament centre line is found by fitting the detected particle centers with a polynomial function. The angle ϑ is then calculated at the median point of the centre line. These steps are shown in an illustration in Fig.3.2(a), which is made from a processed experimental image.

Experiments to determine the filament bending modulus A_b were made by registering the y-displacement as a function of time t, as illustrated in Fig.3.2(b) with the data from processed experimental images for an initially deformed and relaxed filament after the magnetic field is switch off from a rotating state. In Fig.3.2(c), the approximated centreline from a polynomial fit of data from the processed experimental images is shown for four different frequencies at a fixed magnetic field strength.

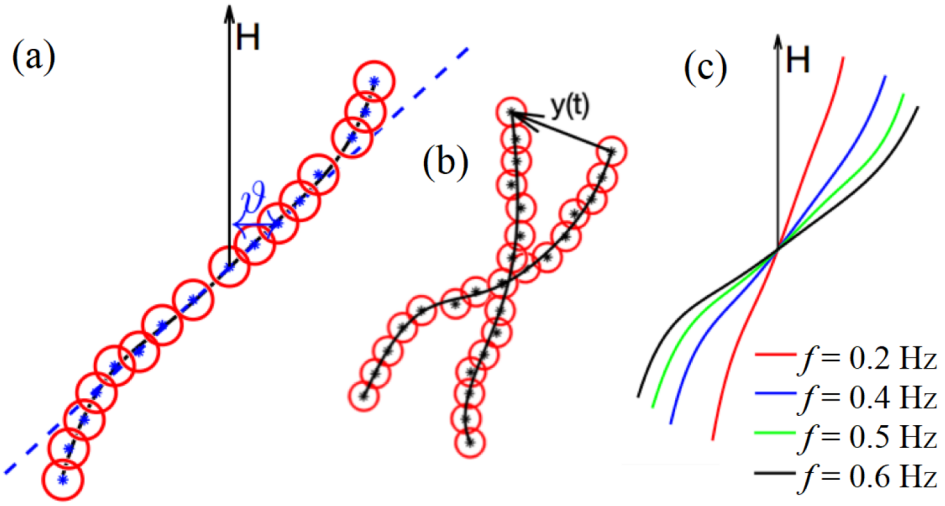

FIGURE 3.2: Illustration of the image processing process. (a) shows the detected circular shapes (red circles) of the particles with centres (blue asterisks), the black dashed line shows the centres coordinates fit with a polynomial of sixth order. Tangent angle ϑ is marked with a blue arrow. (b) Processing method for relaxation experiments, the y-displacement of the tip particle coordinate was tracked over this. (c) Shows the approximated centrelines over a range of frequencies f (0.2, 0.4, 0.5 and 0.6 Hz) at a fixed magnetic field strength $H = 8.6$ Oe.

3.1.3 Results

As mentioned earlier, the experiments are done under different operating conditions for filaments with different lengths. The angle ϑ was calculated for filaments with three different lengths L, as shown in Fig.3.3. Blue, red and green dashed lines connect angle values for filaments with length $L = 16$ μm, 38 μm and 46 μm respectively at two field frequencies $f = 1$ Hz and $f = 2$ Hz, at $H = 6.9$ Oe.

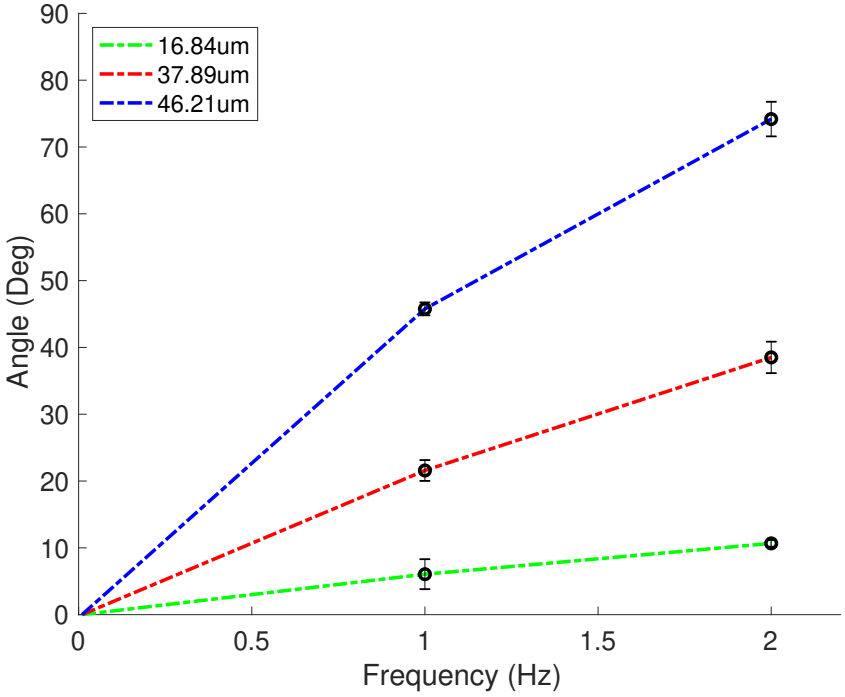

FIGURE 3.3: Relationship between the angle ϑ and frequency f under a rotating magnetic field at $H = 6.9$ Oe for filaments with different lengths $L = 46.2$ μm (blue line), $L = 37.9$ μm (red line) and $L = 16.8$ μm (green line).

These results show that longer filaments undergo a higher deformation at a fixed frequency and field strength. Therefore, the increase of the filament length will result in a higher deformation by the viscous torques under a rotating field. The results obtained showing the effect of varying the magnetic field strength under a range of frequencies (0.1 Hz to 5 Hz) for the same filament with a length $L = 46.3$ μm is shown in Fig.3.4. The circles, points and squares donate the calculated values of ϑ at three magnetic fields 8.6 Oe, 17.2 Oe and 25.5 Oe respectively. From the results in Fig.3.4 it is visible that the increase of the magnetic field strength results in a lower angle ϑ. This is expected considering the force balance between magnetic torque (which is a function of the field strength) versus the viscous drag exerted by the fluid and the elasticity of the filament, resulting in a dynamic steady state. It should be also noted that at low frequencies the angle ϑ has a linear relationship with

the frequency, due to the low contribution of elastic forces. At higher frequencies, ϑ deviates to lower values as compared to the the linear fits, shown as the colored dashed lines in Fig.3.4. A further increase of frequency forces the filament to move out of the rotating plane, with observed ϑ values approaching 90 °. The filament behaviour at higher frequencies will be further discussed in section 3.2.

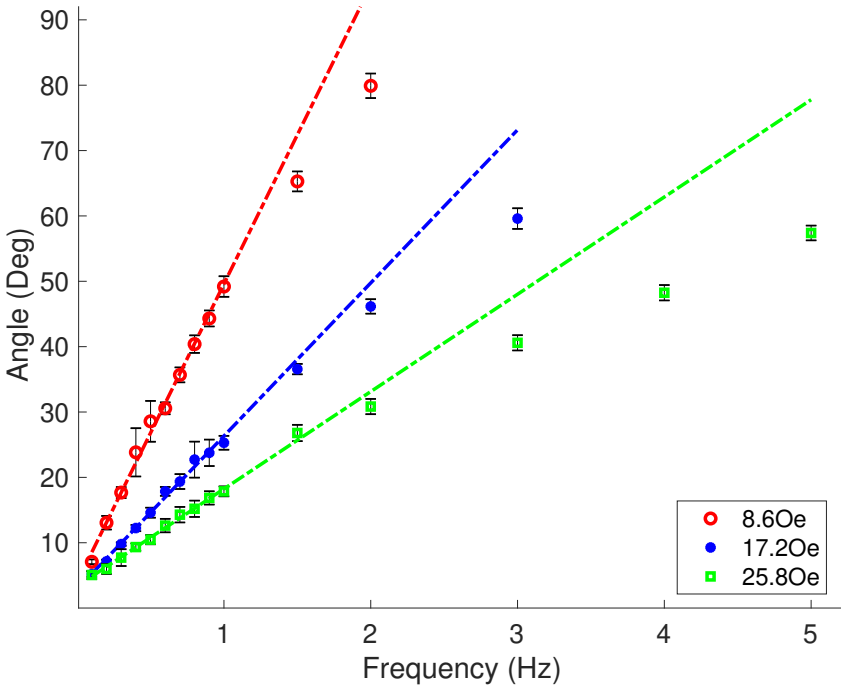

FIGURE 3.4: Relationship between the angle ϑ and frequency f, under rotating magnetic field with different strengths, $H =$ 8.6 Oe (red), $H = 17.2$ Oe (blue) and $H = 25.8$ Oe (green) for a filament with a length $L = 46.3$ μm.

To approximate the filament magnetization from the obtained experimental results and considering the observable linearity of ϑ dependence at low deformations regime, the following relation is used, which is obtained theoretically by considering rigid rod:

$$\vartheta = 0.086 \frac{\omega \tau}{Cm} \tag{3.1}$$

where Cm = $\frac{MHL^2}{A_b}$, is the magnetoelastic number, $\tau = \frac{\zeta L^4}{A_b}$ and ζ is the hydrodynamic coefficient approximated by $4\pi\eta$, the viscosity of the fluid η is approximated with the water viscosity 0.01 P. Using the experimental results obtained in Fig.3.4, we obtain the relationship of $\frac{d\theta}{df}$ as a function of $\frac{1}{H}$, as shown in Fig.3.5. Since the relationship is linear, the slope a of $\frac{\theta}{f}$ = a $\frac{1}{H}$ was found to be 6.8 Oe·s. Substituting the values with the relationship obtained by the numerical simulations in 3.1, the filament magnetization per

unit length M is found to be $M = 2.14 \cdot 10^{-7}$ emu. While the magnetic moment per particle m is found to be $m = 9.01 \cdot 10^{-11}$ emu using $M \cdot d$, where d is the average particle diameter ($d = 4.26$ μm).

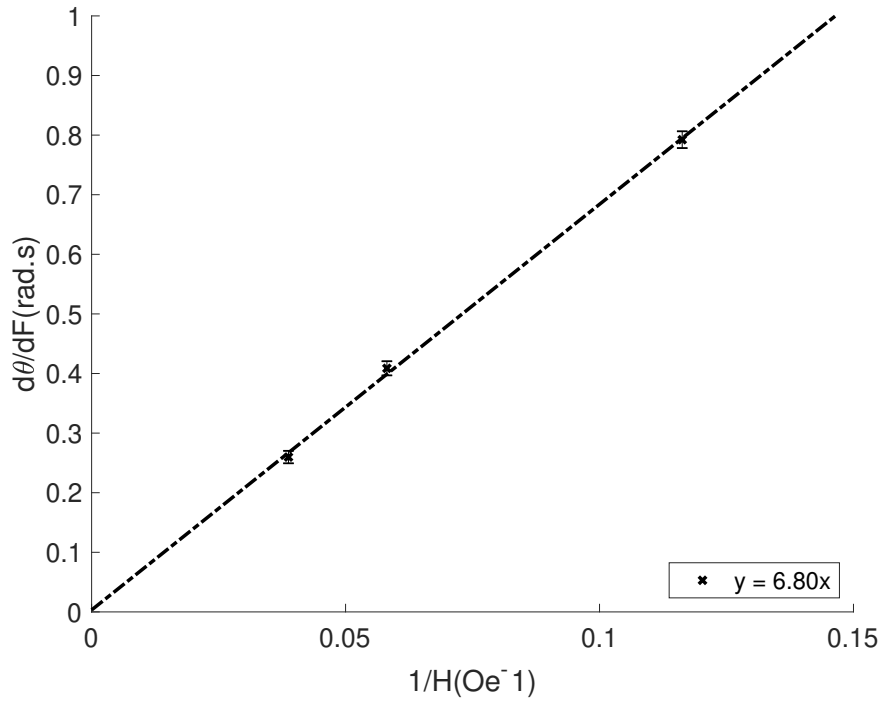

FIGURE 3.5: Relationship between $\frac{d\vartheta}{df}$ and $\frac{1}{H}$, obtained for a filament with length $L = 46.3$ μm.

The filament bending modulus is measured by registering the displacement of a filament tip along the y axis over time after rotating field is switched off, as illustrated in Fig.3.2(b). The measured y-displacement over time is shown in Fig.3.6 and was found to have an exponential dependence for three filaments with different lengths. The decrements of the filament relaxation from the decay rate were found to be 0.25 s^{-1}, 0.42 s^{-1} and 0.25 s^{-1} for filaments with length $L = 80$ μm, 76.4 μm and 63.2 μm respectively. Using the solution for a free rod with the unclamped boundary conditions for the elastic micro filament problem (eq: 3.2), as presented by Wiggins et al. 1998, the bending modulus A_b is then estimated using the decay rates $1/\tau$ obtained from the experimental data.

$$\frac{1}{\tau} = 3.93^4 L^{-4} A_b / \zeta \tag{3.2}$$

The average bending modulus was estimated by a liner fit of the relaxation decrements with the filament length, including experimental errors in the registration of the filament tip displacements and is shown in Fig.3.7. The estimated value of bending modulus is $A_b = 6.5 \pm 3.4 \cdot 10^{-13}$ erg.cm.

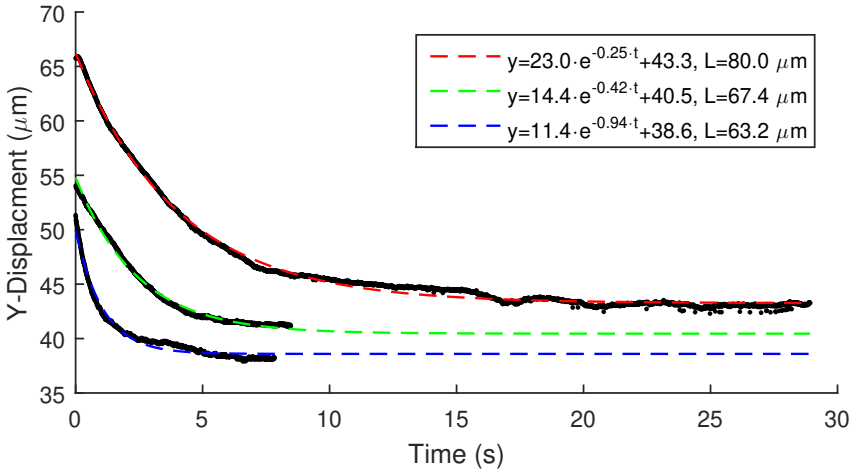

FIGURE 3.6: Filament relaxation behaviour for different filament lengths L and the initial rotating field conditions: $L = 80.0\ \mu$m, $f = 1.0$ Hz and $H = 8.6$ Oe (red curve). $L = 63.2\ \mu$m, $f = 1.0$ Hz and $H = 13.7$ Oe (blue curve). $L = 67.4\ \mu$m, $f = 1.5$ Hz and $H = 8.6$ Oe (green curve).

From the results presented above, it was found that the filament under the action magnetic field deform with an 'S'-like shape. This was previously seen experimentally for filaments using para-magnetic particles (Kuei et al. 2017) and numerically for ferromagnetic flexible rods (Goyeau et al. 2017). The flexibility of the filament is determined by the operating condition and its physical properties. For example, higher deformations can be seen when increasing frequency, decreasing the magnetic field strength and when using filament with longer length. Moreover, the length of the DNA linker determines the bending modulus (Byrom et al. 2014), due to the contribution of the elastic compared to the magnetic dipole interaction between the particles. By using the relation $Ab = M^2/2$ as given in (Cēbers 2005; Vella et al. 2014; Kiani et al. 2015), we find that the bending modulus obtained experimentally is two orders of magnitude larger than it is expected from the magnetic energy contribution. Hence, it can be assumed that the filament deformations observed are mainly driven by the elasticity of the DNA linkers between the particles.

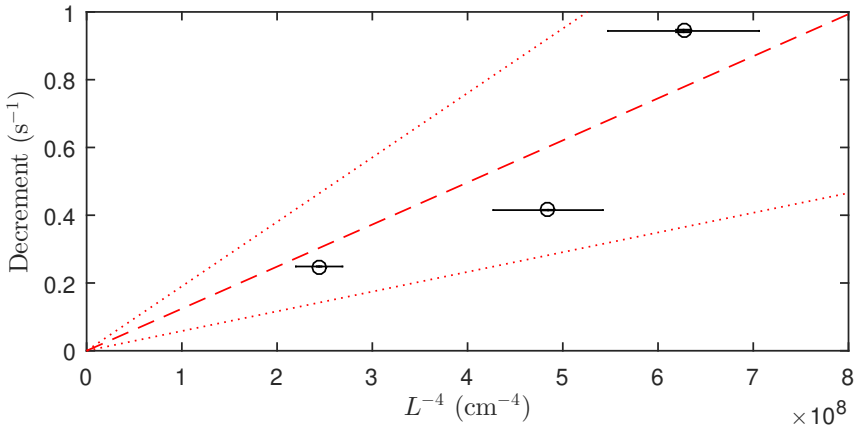

FIGURE 3.7: Relationship between relaxation decrements and L^{-4} for different filament lengths. Black circles are experimental points with errorbars. Red dashed line is linear fit and red dotted lines are confidence intervals of 3σ.

3.2 Behaviour at higher frequency ($f > f_c$)

3.2.1 Experimental procedures

Experiments were performed in the same way as presented in section 3.1 with the exception that a wider range of frequencies was used, to observe the filament dynamics particularly at higher frequencies. As these experiments take longer time and the filament slightly moves around during the rotations, we first apply a rotating field of strength H = 17.2 Oe, f = 1 Hz for 15 minutes. This allows catching and connecting the free particles in the surrounding of the filament. Otherwise filament parameters can change during the experiment, complicating the analysis. This slight movement may happen due to several reasons - variable interaction with the wall or a somewhat unsymmetrical rotation with respect to the filament centre, due to the particle size distribution, variation in the number of links from DNA fragments. The camera acquisition mode is set to a fixed frame rate to allow capturing the filament configurations at different locations within a period.

Examples of the deformed filament shapes observed are shown in Fig.3.8. In images (a)-(c) the difference of deformed shapes of a filament with L = 41 μm can be seen for an increasing frequency at a constant field strength H. In Fig.3.8(a) & (b) it is visible that the filament performs a steady in-plane rotation with a slight 'S'-like deformation, as discussed in chapter 3.1). While in Fig.3.8(c), the filament undergoes a 3D motion, observable experimentally due to the blurred filament body shape when focusing on one of the filament tips. For longer filaments at the same constant frequency above f_c and the same field strength, higher deformations are observed. This can be seen in Fig.3.8(d), (e) and (f), where $L = 33$ μm, $L = 41$ μm and $L = 65$ μm respectively. Similarly, the observed shapes of a filament with length $L = 46$ μm

are shown in Fig.3.8(g)-(i) for a frequency $f = 5$ Hz when increasing the field strength.

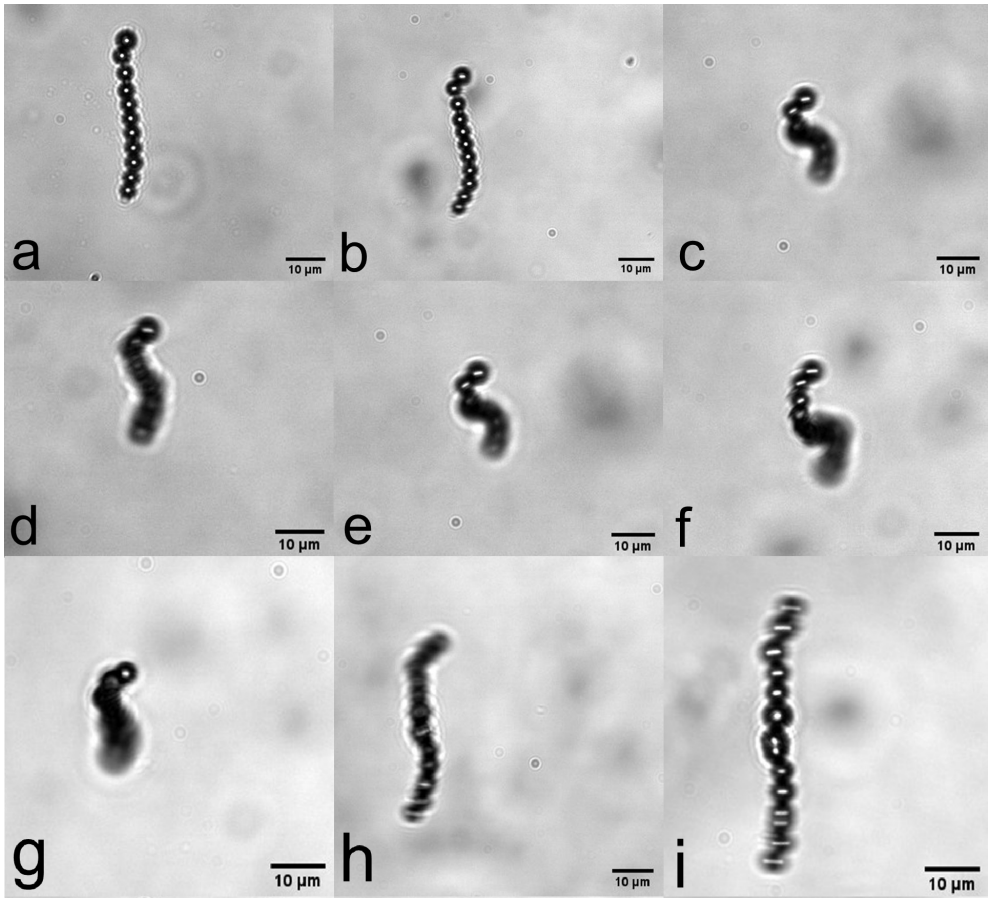

FIGURE 3.8: Shapes of deformed filaments under rotating magnetic field. A filament with $L = 41$ μm at $H = 17.2$ Oe for frequencies (a) $f = 1$ Hz, (b) $f = 4$ Hz, (c) $f = 9$ Hz. Filaments at $H = 17.2$ Oe and $f = 8$ Hz for filaments with lengths (d) $L = 33$ μm, (e) $L = 41$ μm, (f) $L = 65$ μm. A filament with $L = 46$ μm at $f = 5$ Hz and magnetic fields (g) $H = 4.3$ Oe, (h) $H = 12.9$ Oe, (i) $H = 25.8$ Oe.

3.2.2 Image processing

The images were processed on Matlab in the following manner. The filament image is first segmented using a threshold with a manually chosen intensity value. This step results in a binary image, which is then processed by an open source package NRBC (Zeng et al. 2015), to approximate the filament centre line in each image. And the process is repeated for every image of the series.

In this investigation, we characterize the filament deformations as the ratio $\frac{R}{L}$ between the radius of the tip trajectory R with the filament length L. Furthermore, The filament length L is approximated here as $2 \cdot R_0$, not the measured filament length. where R_0 is the radius of the tip trajectory radius observed for a filament at low frequencies without a notable shape deformation.

The method used for finding R is illustrated in Fig.3.9. In (a) examples of experimental images at different locations and over several rotations are shown. From the detected centre line (shown as red dashed line), the coordinates of the filament tip which is in-focus (the yellow point), are registered over several rotations. To account for the slight movement that the filament undergoes, the tip coordinates for each location are corrected by translation with a reference location. The calculated tip coordinates are then fitted with a circle function, as shown in Fig.3.9(b) for a sample experimental data. Hence, this allows to estimate the radius of the tip trajectory R while accounting for the unsymmetrical centre of rotation. The difference of the centre coordinates obtained by fitting and the reference point are shown in Fig.3.9(b) as (x_c, y_c) and (x_r, y_r) respectively. Moreover, the experimental results show that the tracked tip trajectories follow a circular path.

3.2.3 Results

The experimental results obtained for the relationship between R/L and frequency are shown in Fig.3.10 for filaments with three different lengths. Red, green and blue diamonds denote data points for L = 65 μm, 41 μm and 33 μm respectively measured under a constant field strength H = 17.2 Oe. This relationship shows that an increase in frequency first results in a minor decrease of R/L, which is followed by an abrupt drop of R/L, which can be seen clearly for L = 41 μm and 33 μm data behaviour in Fig.3.10. This abrupt change was observed experimentally to occur during the transition from a 2D planar regime to 3D motion for frequencies above the critical frequency f_c. A further increase in the frequency was observed to have lower influence on R/L. Moreover, longer filaments were found to have lower values of critical frequency f_c.

To compare the experimental results with numerical simulation, the model from section 1.3 is used. As discussed previously, Goyeau et al. 2017 investigated the filament dynamics under a rotating field using the same model and showed that rotations are in a 2D plane synchronously following the field or becoming asynchronous and having a back and forth motion. This back and forth motion has been previously observed for paramagnetic nano rods

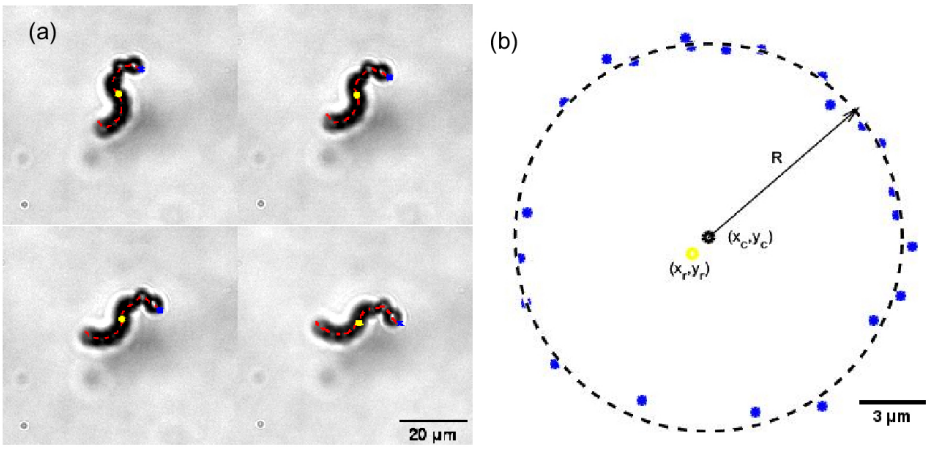

FIGURE 3.9: An illustration of how radius R of filament rotation is found in each experiment. (a) Four consecutive images of a filament, which is rotating in 3D. Dashed red lines indicate the centre line. The blue points show the tracked tip, while yellow points represent the tracked centre, which is used for reference. (b) The tracked tip coordinates for one experiment (blue points) are fitted with a circle (black dashed line). Yellow point (x_r, y_r) is the reference and black point (x_c, y_c) denotes the fitted centre of the circle.

under a rotating field (Frka-Petesic et al. 2011). In the simulations conducted here, we also take into account the small perturbations which the system may experience. It is defined as an initial condition - a tiny deviation from the rotational plane is made via setting z-coordinate to 0.004 for one of the filament tips (numerically it is normalised with the filament length L).

From numerical simulation results, the change in the filament initial configuration was sufficient to predict the experimentally observed behaviour. For example, the relationship between the filament tip z-coordinates in dependence on the dimensionless time t at $Cm = 50$ and $\omega\tau_e = 1000$ is shown in Fig.3.11. The coordinates and time are scaled with the filament length L and the elastic relaxation time τ respectively. It can be seen that the filament undergoes first a transition state with some oscillations, eventually reaching a stable 3D motion region after $t \approx 0.14$. This stability is noticed from the unchanged z-coordinate of the filament tip over time. The numerically obtained configurations for a frequency above f_c, when the processional regime is established are shown in Fig.3.12 for a filament with $Cm = 220$ and $\omega\tau_e = 4500$ at different locations within a period. From the numerically obtained shapes it can be seen that the filament becomes strongly bent, while the tips move in antiphase along circular trajectories similar to what was observed experimentally in Fig.3.9.

To numerically estimate the critical frequency f_c, which here defines the transition from planar to 3D synchronous rotation, the exponential decay rate

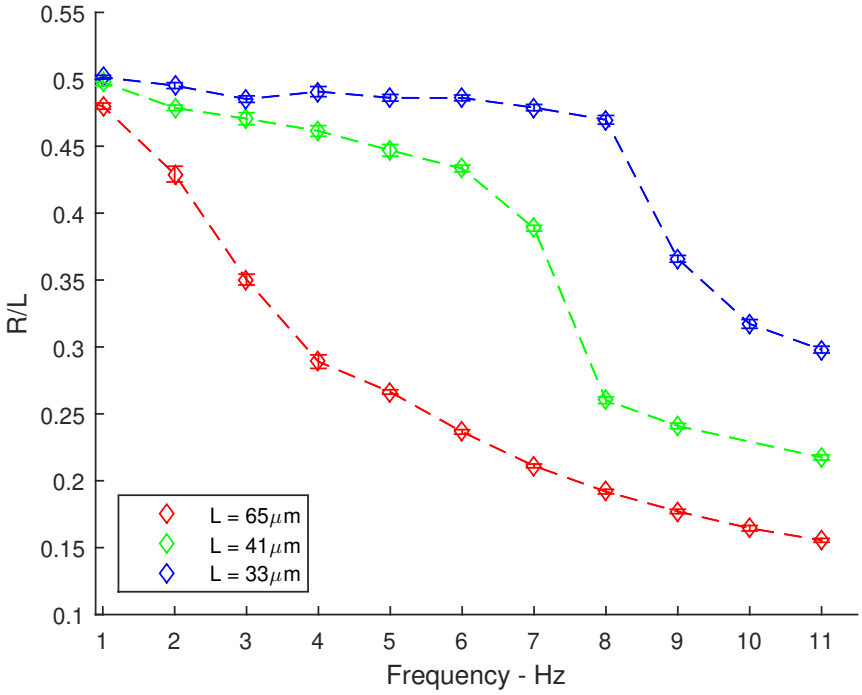

FIGURE 3.10: Experimental data for the relationship between R/L and frequency f. Deformation of filaments with different length is measured operating at the field strength $H = 17.2$ Oe.

λ is obtained by registering the relaxation behaviour of a filament tip coordinate in the z-axis to the plane of rotating field. Since λ characterizes an exponential behaviour, it is obtained using the relationship $z = z(0)exp(-\lambda t)$. After obtaining λ over a range $\omega\tau$ values for several Cm, the critical $\omega\tau_c$ for each Cm can be found, as shown in Fig.3.13(a) for $Cm = 225$ and $Cm = 300$. Considering the linear dependence shown in Fig.3.13(a), the critical $\omega\tau_c$ is obtained by extrapolating the line to $= 0$. The obtained results for $\omega\tau_c$ dependence on Cm are shown in Fig.3.13(b). Again a linear relation can be observed and the coefficient is found from the slope $\omega\tau_c = 12.04\ Cm$. This value obtained for the critical frequency is similar to the one obtained for the transition frequency from a 2D synchronous to 2D asynchronous regime in Goyeau et al. 2017. However, here critical frequency describes the transition to a 3D motion.

Numerical simulations allow us to illustrate the filament shapes. Projections of the filament configurations in the plane of field rotation at different time instants within a period, when operating at frequencies above critical, are shown in Fig.3.14, where x and y axis are scaled with the filament length at $Cm = 220$ and $\omega\tau_e = 4500$.

From the estimated critical frequency f_c, the relationship between the filament deformations characterized by R/L with frequency normalised by the

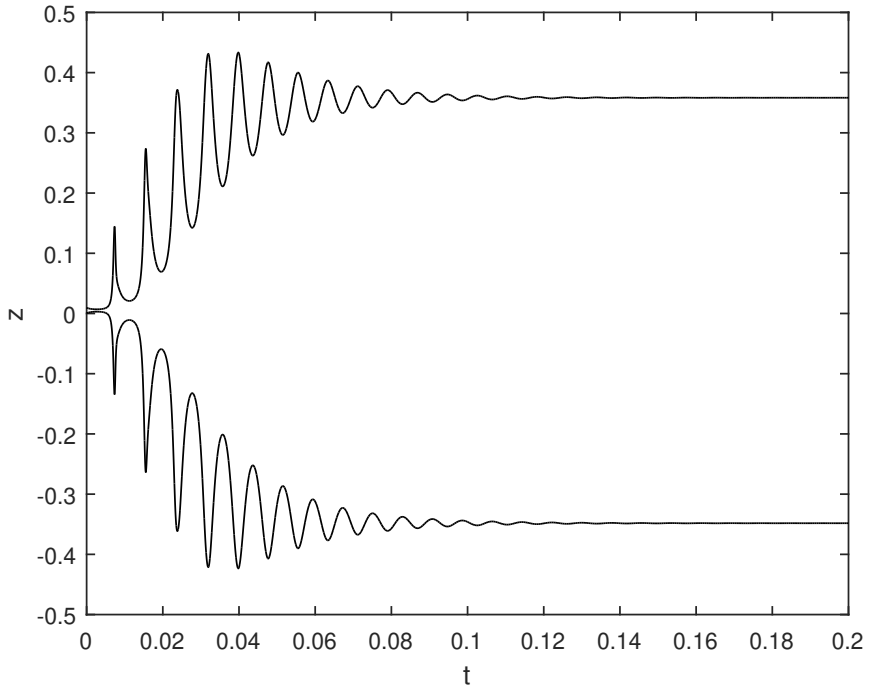

FIGURE 3.11: Time dependence of filament tips' z coordinates show formation of a precessional regime. Numerical calculation is performed for $Cm = 50$ and $\omega\tau_e = 1000$.The coordinates are scaled with the length of filament L and time with the elastic relaxation time τ_e.

critical frequency $\omega\tau/\omega\tau_c$ is shown in Fig.3.15. The behaviour can be divided into three regimes as follows:

- In **region I**: operating at frequency below critical with minor deformations until reaching $\omega\tau/\omega\tau_c \approx 0.5$, followed by a notable drop in R/L ratio until reaching $\omega\tau/\omega\tau_c = 1$. Moreover, higher values of Cm have a sharper decreasing slope, which may be explained from the increased deformation as a function of filament length, when considering the definition of Cm.

- In **region II**, the filament is operating at frequencies above the critical value. In this regime, a rapid increase in the deformation appears, which is seen from R/L behaviour.

- A further increase in $\omega\tau/\omega\tau_c$ where its value is > 2 is shown in **region III**. Here, a lower influence of the filament deformation can be noted as observed from R/L slope when compared for smaller operating frequencies. Moreover, when looking at higher values of Cm in region III, there is no observable change of the R/L behaviour for values above $Cm > 200$.

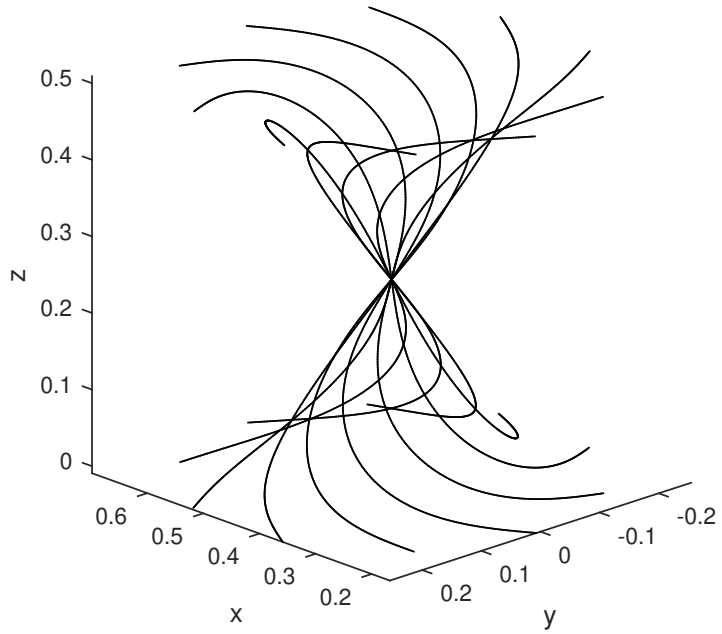

FIGURE 3.12: Configurations of the filament in precessional regime at several moments of one period for $Cm = 220$, $\omega\tau_e = 4500$. Coordinates are scaled with the length of filament L.

When comparing the above presented results obtained both numerically and experimentally, the filament behaviour is found to be in a good agreement. For example, from the observed relationship between R/L and frequency, shown in Fig.3.10 for experimental and Fig.3.15 for numerical results. Similarly, the filament shapes observed as shown in Fig.3.8 and numerically in Fig.3.14. To compare the results quantitatively, the experimental data, shown in Fig.3.10, was fitted with results obtained by numerical simulation. In these experiments, R/L values were calculated for a filament with length $L = 46$ μm, operating at a range of field strength and frequencies. To fit the experimental results obtained (shown as diamonds in Fig.3.15) with numerical results, two parameters were introduced here: A which is linked with the magnetic field strength H and Cm by $A = Cm/H$ and B, which is linked with the non dimensional frequency by $B = \omega\tau_e/f$.

Fitting the results was done using Matlab, where A and B are obtained by a non-linear square fit of all the experimental results at once. To do so, 'scatterinterpolant' function was used for the characterized filament deformation $R/L = function(\omega\tau_e, Cm)$, with several numerical simulation results, which were done using different values of Cm for a range of $\omega\ \tau$. The selected range was based on the previously estimated parameters of magnetic moment M and bending modulus A_b, as presented in section 3.1. From the obtained local minima of the non-linear least square fit, A and B were found to be

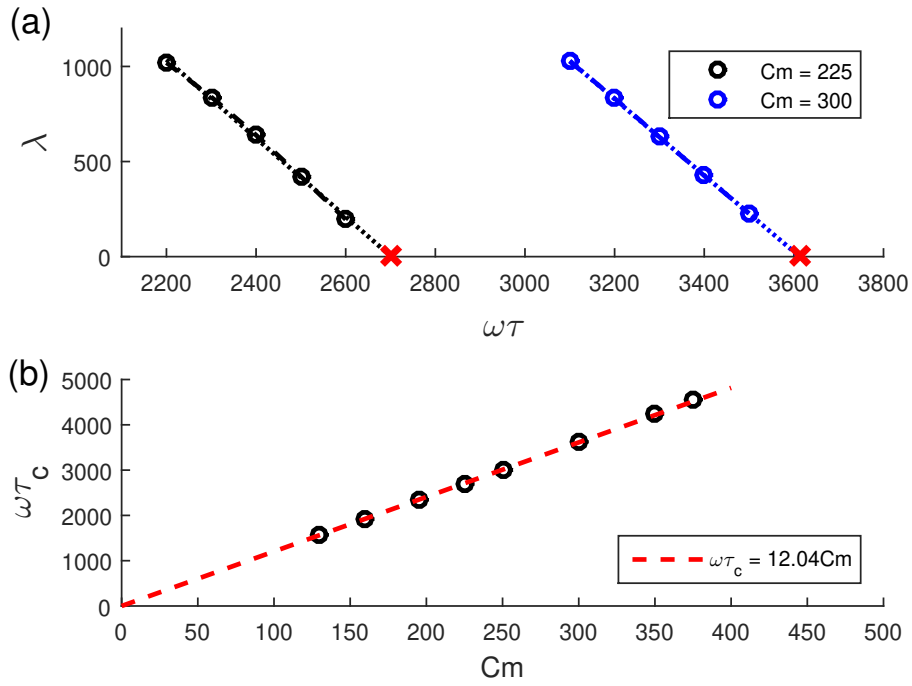

FIGURE 3.13: Critical frequency $\omega\tau_c$ is proportional to the magnetoelastic number Cm. (a) An example of finding critical frequencies by decrement (λ) analysis for $Cm = 225$ and $Cm = 300$. Circles represent numerical data, lines - linear fits and red $\times$ correspond to critical frequencies ($\omega\tau_c$. (b) Critical frequency as a function of Cm. Circles are numerical data and the dashed line is the linear fit.

125 ± 2 Oe^{-1} and $241 \pm 4\ s^{-1}$ s respectively.

From the best fit, A_b and M is found to be $1.5 \cdot 10^{-12}$ erg·cm and $4.9 \cdot 10^{-7}$ emu respectively. These estimates are not far from the estimated values from the force balance at low deformation regimes and from the filament relaxation experiments in section 3.1. However, these results show that this filament synthesis methodology can vary the filament physical properties, remarkably, the bending modulus - by one order of magnitude difference. This may be due to either the difference of linked DNA fragments between the particles or due to the variation of particle size along the filament, as mentioned earlier. The numerical results for the corresponding experiment are shown in Fig.3.16 as dashed lines denoting the best fits and colored regions showing the upper and lower errors, calculated from the upper and lower deviations of parameters A and B. The obtained values of Cm for the numerical simulation shown in Fig.3.16, corresponds to field strength H values defined in experiments as given in Table 3.1.

To compare the filament shapes in the 3D regime between experimental and numerical simulations performed, an overlap of numerical configurations was made on experimental images, which are observed in as 2D shapes.

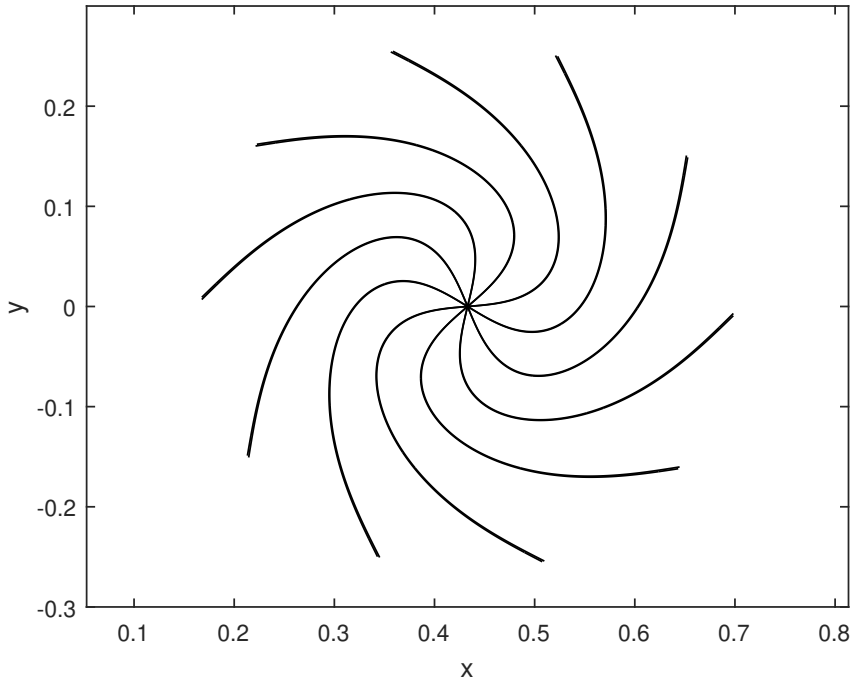

FIGURE 3.14: Projection of the filament configurations in the precessional regime on the plane of the rotating field (x-y plane, $Cm = 220$ $\omega\tau_e = 4500$).

H, Oe	Cm
4.3	31.0
8.6	62.5
12.9	93.8
17.2	125.0
25.8	187.5

TABLE 3.1: Experimental field strength H and corresponding magnetoelastic numbers Cm, as found by the non-linear fit.

This comparison is shown in Fig.3.17 for a filament with length $L = 46$ μm, frequency $f = 5$ Hz and operating at different field strengths ($H = 4.3$ Oe, $H = 8.6$ Oe and $H = 12.9$ Oe for images (a), (b) and (c) respectively). From this comparison, a good agreement was found. However, discrepancies in the filament length was observed, notably as shown in Fig.3.17(c), which may be a result of the chosen length L, explained in the image processing section of the projected tip radius for an undeformed filament.

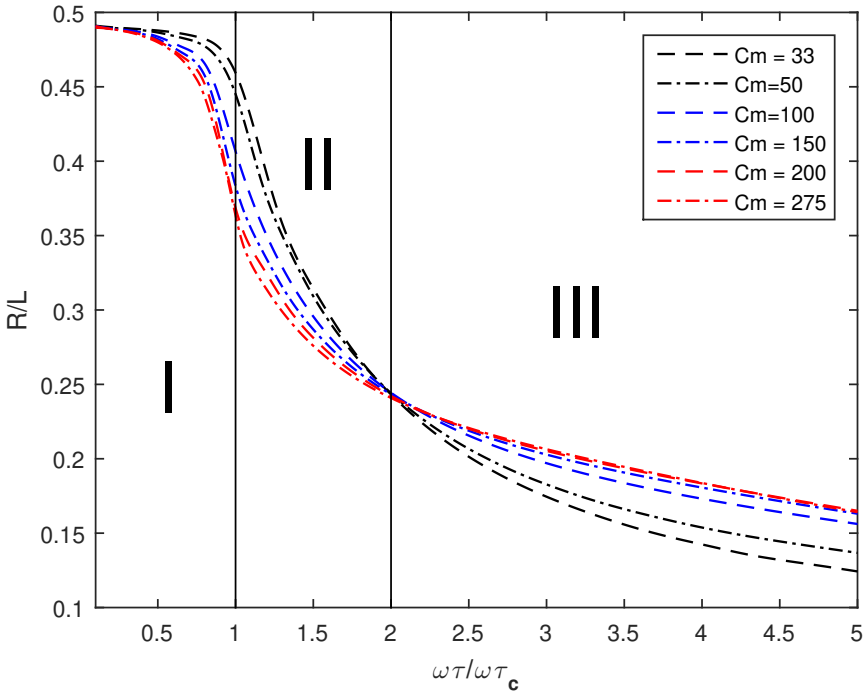

FIGURE 3.15: Numerical simulation results for filament deformations. Normalized deformation R/L as a function of normalized frequency $\omega\tau/\omega\tau_c$.

3.3 Discussion

From the results presented above, it can be seen that flexible chains formed by linked ferromagnetic particles, under the action of a 2D rotating magnetic field, rotates synchronously with the magnetic field in its plane of rotation or undergo a transition to a 3D motion. This transition is dependent on the critical frequency (f_c), which depends on the filament flexibility. This transition was experimentally observed when the filament tangent angle at the centre ϑ orients perpendicularly with the magnetic field direction. At frequencies below f_c, the behaviour of the filament was characterized by measuring the lag with the magnetic field. Such measurements have allowed to estimate the magnetization per unit length M, considering the low effect of elastic forces arising in the energy balance between filament elasticity and magnetic torques at low deformation regimes. Hence, these results show a linear dependence (Fig.3.5). The estimated value of M is not far from the measured one, obtained by a vibrating sample magnetometer (Ērglis et al. 2010), where $M = 3.3 \cdot 10^{-7}\ emu$. The shapes obtained at this regime were observed to have either an undeformed straight filament shape or have an 'S'-like deformation, where the filament tips are pointing in the opposite direction following the magnetic field with angles up to 30 degrees.

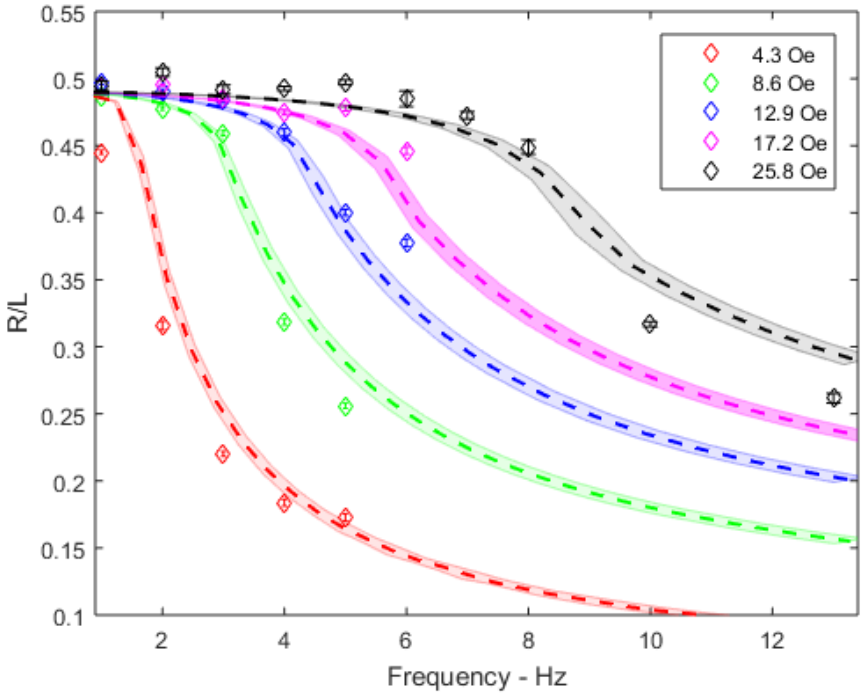

FIGURE 3.16: Filament deformation comparison between experiment and numerical results via R/L dependence on frequency. The colored diamonds denote experimental data for filament with $L = 46$ μm operating at different field strength H. The dashed lines represent numerical simulations scaled with values of parameters obtained from the fit for different Cm values as shown in Table.3.1. The shaded area represents the error margins obtained from fitting.

The bending modulus Ab of the filament was estimated from the experimental relaxation rate from the deformed shapes under a rotating field. The thermal fluctuations here that occur due to Brownian motion were not found to be large enough to be applicable in determining the filament bending modulus, which may be probably due to the particle size or DNA length used. This differs form the investigation by Byrom et al. 2014, who estimated the filament elasticity by registering the displacements due to thermal fluctuations. Furthermore, from the estimated values of Ab, the filament was found to be quite stiff, as the respective persistence length has a value of tens of centimetres.

The transition to a 3D rotating motion at frequencies above critical frequencies was previously predicted numerically for magnetic particles in a rotating field (Cīmurs and Cēbers 2013) and where experimentally realized in a recent study for nano-rods made from ferro-magnetic material (Palkar et al. 2019). Moreover, a transition to an out of plane motion was also observed for paramagnetic rods under precessing magnetic field (Cīmurs et al. 2019). This movement to the 3D motion may be explained by considering the

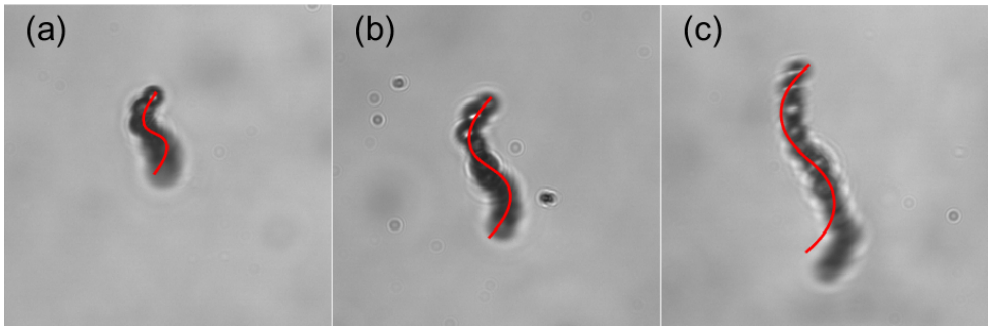

FIGURE 3.17: Direct comparison of filaments in experimental images and numerical simulations, using best fit, shows a qualitative agreement. Filament of $L = 46$ μm at $f = 5$ Hz and different H is compared to numerical results at $\omega\tau = 1208$ and different Cm. (a) $H = 4.3$ Oe, $Cm = 31$, (b) $H = 8.6$ Oe, $Cm = 62.5$, (c) $H = 12.9$ Oe, $Cm = 93.8$.

perturbations to the system. For example:

- The filament has a slightly unsymmetrical shape formed from the adapted synthesis process.
- The earth magnetic field which is not accounted for in the numerical model.
- Other existing magnetic field gradients from the experimental setup may interfere.
- Thermal fluctuations for the whole filament.

The increase of frequency at the planar regime will result in a lower hydrodynamic drag, seen in Fig.3.4, showing the relationship between the ϑ and f, where ϑ deviates from the linear dependence. This can be explained from the role played by the filament elasticity and was found also found numerically to match. When the critical frequency (f_c) is reached and considering such mentioned possible perturbations, the filament moves to structurally preferable 3D regime.

The estimated critical frequency from the numerical simulations ($\omega\tau_e = 12 \cdot Cm$) is similar to one calculated for paramagnetic filaments, when an asynchronous planar regime is established (Kuei et al. 2017). Moreover, it is shown that the contribution of magnetic dipolar interactions on the filament elasticity using $A_b = M^2/2$ (Cēbers 2005), the calculated A_b from filament relaxation time and by fitting the experimental results with numerical (as shown in Fig.3.16) was found to be two and one order of magnitude higher respectively. Hence, we can deduce that the filament elasticity is mainly present due to the elasticity provided by DNA fragments linking the particles. Increasing the DNA length will result in a decrease of the persistence length, resulting in different dynamics as folding or coiling, observed experimentally by Kuei et al. 2017. Such behaviour was not seen at the ranges of

the estimated A_b and may rise an interesting research question - if behaviour of magnetic chains made from ferromagnetic particles remains the same with the increase of filament flexibility.

As discussed in section 1.1, the flexible magnetic chains are a good potential candidate for local mixing applications in micro-fluidic devices. This was presented in details in the review article by (Drew et al. 2016; Shanko et al. 2019). From the results obtained, it can be seen that using ferromagnetic filaments can overcome the limitation of the paramagnetic filaments by the transition to a 3D motion, while maintaining to rotate synchronously with the magnetic field. This behaviour may give the advantage in terms of mixing efficiency at higher frequencies when comparing the use of the two materials. Moreover, 3D rotary motion may be advantageous for specific applications, where local mixing is desired over a wider height ranges or across the volume.

Chapter 4

Filament dynamics under a pulsed field

In this chapter, we present a swimmer configuration behaviour which is applicable for chains made from ferromagnetic particles. The filament propels by the application of a pulsed magnetic field profile with a duty cycle of 30%. A part of the results presented in this chapter have been communicated through the publication (Zaben et al. 2021), which can be found in appendix A

4.1 Experimental procedure

Following the filament preparation as presented in chapter 2, 20 μm of the prepared sample is first added to the fluidic cell and then it is placed under the microscope for observation. The camera mode is set to continuous image acquisition with a fixed frame-rate up to 100 Hz. A static field is first applied in the horizontal x-direction for a few minutes, which aligns the filament with the field direction and allow unconnected free particles to attach with the filaments. A pulsed field profile is then applied in the same direction with a duty cycle of 30%, where the field is inverted 30% of time within one period. An example of deformed filament shapes with their corresponding magnetic field direction are shown in Fig.4.1. The magnetic field readings in Fig.4.1(A) H^* are normalised by the maximum field strength value and the time t is normalised with the period of the pulsed magnetic field T. As shown in Fig.4.1(B)(a-c), the filament bends in a U-like shape in the 30% of the period, followed by a relaxation stage as shown Fig.4.1(B)(d-f). At the location shown in Fig.4.1(B)(f), the filament relaxes and aligns with the magnetic field direction.

The swimming direction was found to be perpendicular to the magnetic field, in the y-direction. However, displacements in the x-direction were also observed, which may probably be a result of the difference in the 'arm' length of the filament, due to unequal number or sizes of the particles at each side of the 'U' shape or due to the difference in the number of DNA fragments linking particles.

It should be noted that initially the field profile in the experiments is defined to have the unstable part in the longer part of period. However, the filament was observed to flip its orientation and align with the magnetic field, to

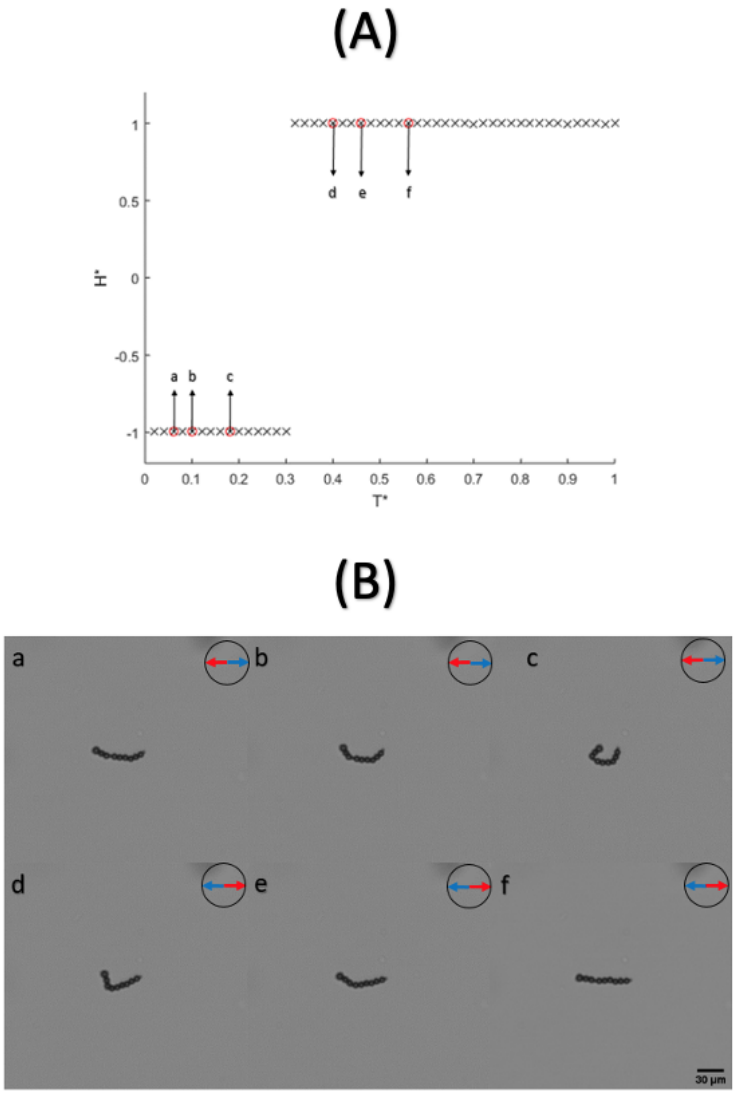

FIGURE 4.1: (A) Magnetic field measurements versus time over one period where $H^* = H/H_{\text{max}}$ and $T^* = t/T$. The red circles show the readings that correspond to images (a-f)(B). (B) An example of filament 'U' deformations under a magnetic field with a 30% duty cycle pulse wave profile, at different location within one period for filament with length $L = 60$ μm, field frequency $f = 2$ Hz and field strength $H = 5.2$ Oe.

have the stable part in the shorter stage in the period. Here, the bending and relaxation stages are referred as the unstable and stable parts of the field respectively, where the filament magnetization direction is opposite and along the field direction.

4.1.1 Image processing

The images were processed using Matlab as following (illustrated in Fig.4.2):

- The filaments were segmented first from the images based on intensity threshold.
- The function *(regionprop)* was used to obtain the centroid of the segmented filament shape, as shown in Fig.4.2(b).
- The centre line of the filament is then obtained by connecting centre points of particles, which was found using Hough tramsform function (Atherton and Kerbyson 2001), identifying circular objects. An example of the identified centre points is shown in Fig.4.2(c).

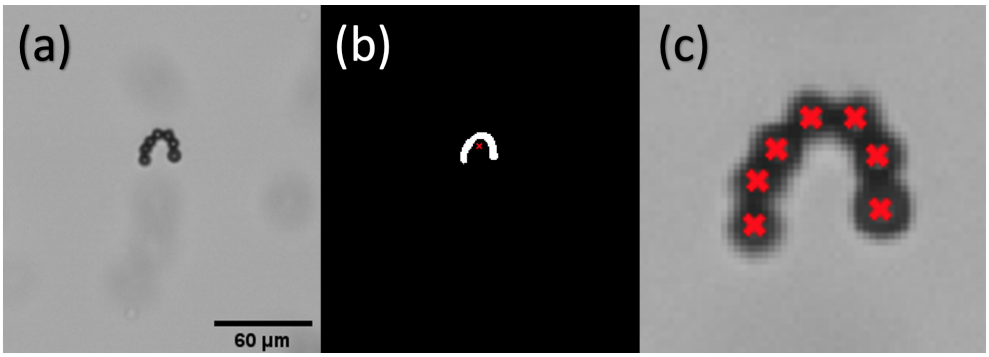

FIGURE 4.2: Illustration of the image processing: (a) Example of a base image used for processing (b) Binary image obtained by intensity threshold, where red 'x' denotes the calculated centroid from *regionprop* function of the filament shape. (c) Estimated particle centre points using Hough tramsform function.

4.2 Results

The experiments were repeated using filaments with different length L, at a range of frequencies f and under a constant magnetic field strength H. The swimming behaviour is characterized by calculating the velocity perpendicular to the field direction. The centre of mass coordinate in the y-direction is first registered over time, as shown in Fig.4.3(a). The velocities are then estimated by a linear fit (shown as by the dashed red line in Fig.4.3(a)). The obtained velocities over a range of frequencies for filaments having different length L are shown in Fig.4.3(b), namely $L = 48$ μm (red), 59 μm (blue) and 70 μm (black). It can be shown from the obtained results in Fig.4.3(b), for $L = 48$ μm and 59 μm, that the velocities reach a maximum and then decrease with the increase of frequency. A maximum value of velocity was not observed for the filament with $L = 70$ μm due to the formation of a ring like shape, when the filament ends get connected.

An example of a ring like shape is shown in Fig.4.4(a). From the maximum observed filament deformations shown in Fig.4.4, it can be seen that the distance between the filament ends in the x-direction is lower when the frequency is increased. For example, as shown in Fig.4.4(a-c) for a filament with the same length at a constant field strength, while the frequency in increasing ($f = 4...6$ Hz), with a step of 1 Hz. Furthermore, It was observed that longer filaments have a lower distance between the two ends, as shown in Fig.4.4(d) when compared with (a), for the same field strength and frequency.

The obtained experimental results were compared with numerical simulations results, by using the same model presented in chapter 1.3 and to investigate the behaviour under a rotating field (as presented in chapter 3). However, the difference between perpendicular $\zeta_\perp$ and parallel $\zeta_\parallel$ hydrodynamic drag coefficients is considered here to account for the filament propulsion. The drag coefficient ratio is defined as λ, where

$$\lambda = -\Big(\frac{\zeta_\perp}{\zeta_\parallel} - 1\Big). \tag{4.1}$$

The values of filament physical properties used for M and A_b are $M = 4.9 \pm 5.0 \cdot 10^{-7}$ emu and $1.5 \pm 2.0 \cdot 10^{-12}$ erg·cm respectively, which were previously estimated as discussed in chapter 3.2. The field profile is defined similar to what is observed in the experiments. A pulsed field profile with a duty cycle of 30%, where the bending stage occurs in the shorter part of the period (30%). An example of numerically obtained configurations with their corresponding field readings is shown in Fig.4.5. In (A) the magnetic field profile is displayed, where H^* is the field strength scaled with the maximum H. The corresponding filament shapes at the locations marked in (A)(a-f) are shown in Fig.4.5(B).

Initially, when using the defined field profile shown in Fig.4.5(A), the resultant filament configuration is the S-like non-swimming deformations, which are non-comparable with the U-like deformations observed experimentally. A condition is then added to the model to avoid the filament to

completely relax and always have a slightly curved shape before the start of each bending stage. This initial curved shape can be seen in Fig.4.5(B)(a).

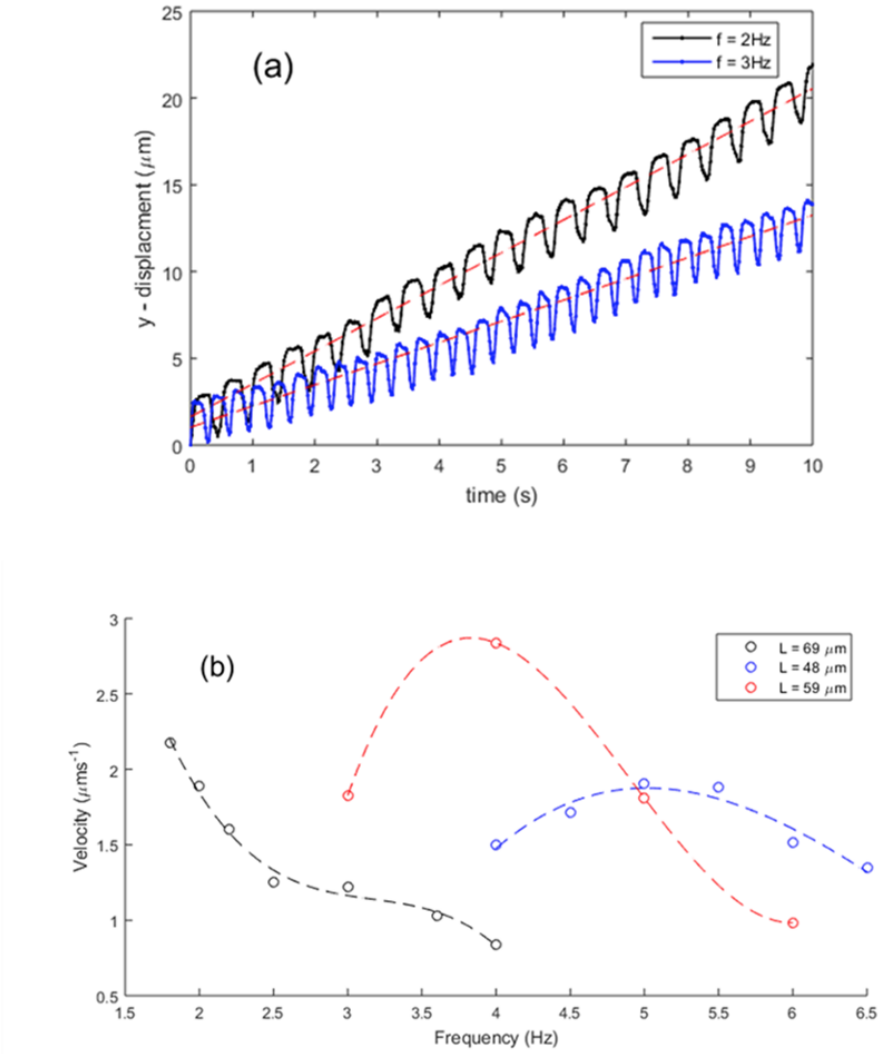

FIGURE 4.3: (a) Relationship between filament centre of mass y-displacements as a function of time for a filament with length $L = 70$ μm and frequencies f = 2 Hz (black line) and f = 3 Hz (blue line) at fixed field strength $H = 5.2$ Oe. (b) Velocity as a function of field frequency for filaments with lengths $L = 48$ μm (red), 59 μm (blue) and 70 μm (black), at a fixed field strength $H = 5.2$ Oe.

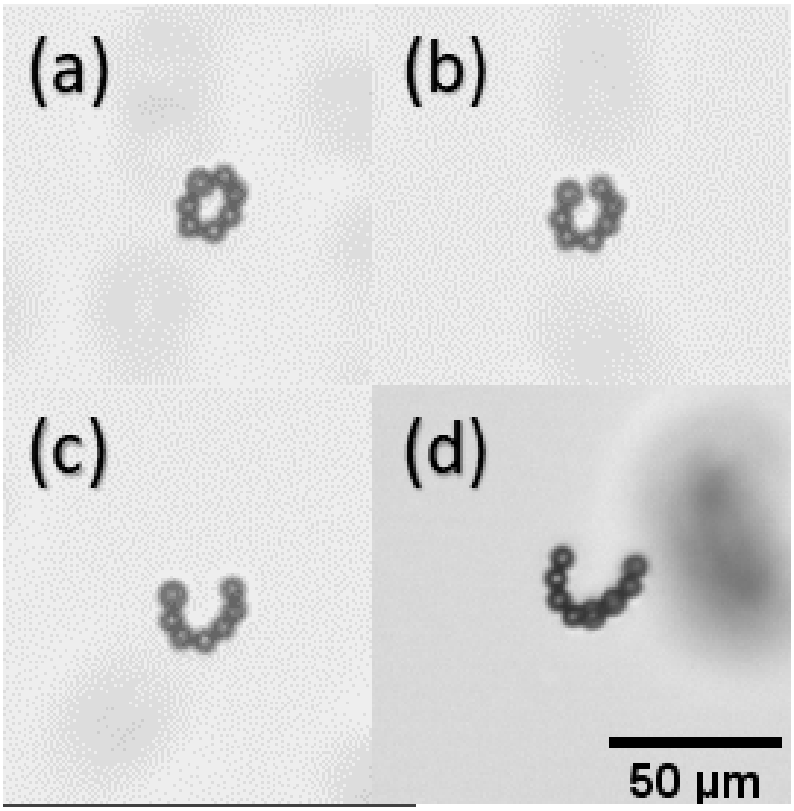

FIGURE 4.4: Maximum observed filament deformation within one period for different filaments. In (a)-(c) $L = 48\ \mu m$, $H = 5.2$ Oe and $f = 4$ Hz, $f = 5$ Hz and $f = 6$ Hz. In (d) $L = 53\ \mu m$ at fixed $f = 4$ Hz and $H = 5.2$ Oe.

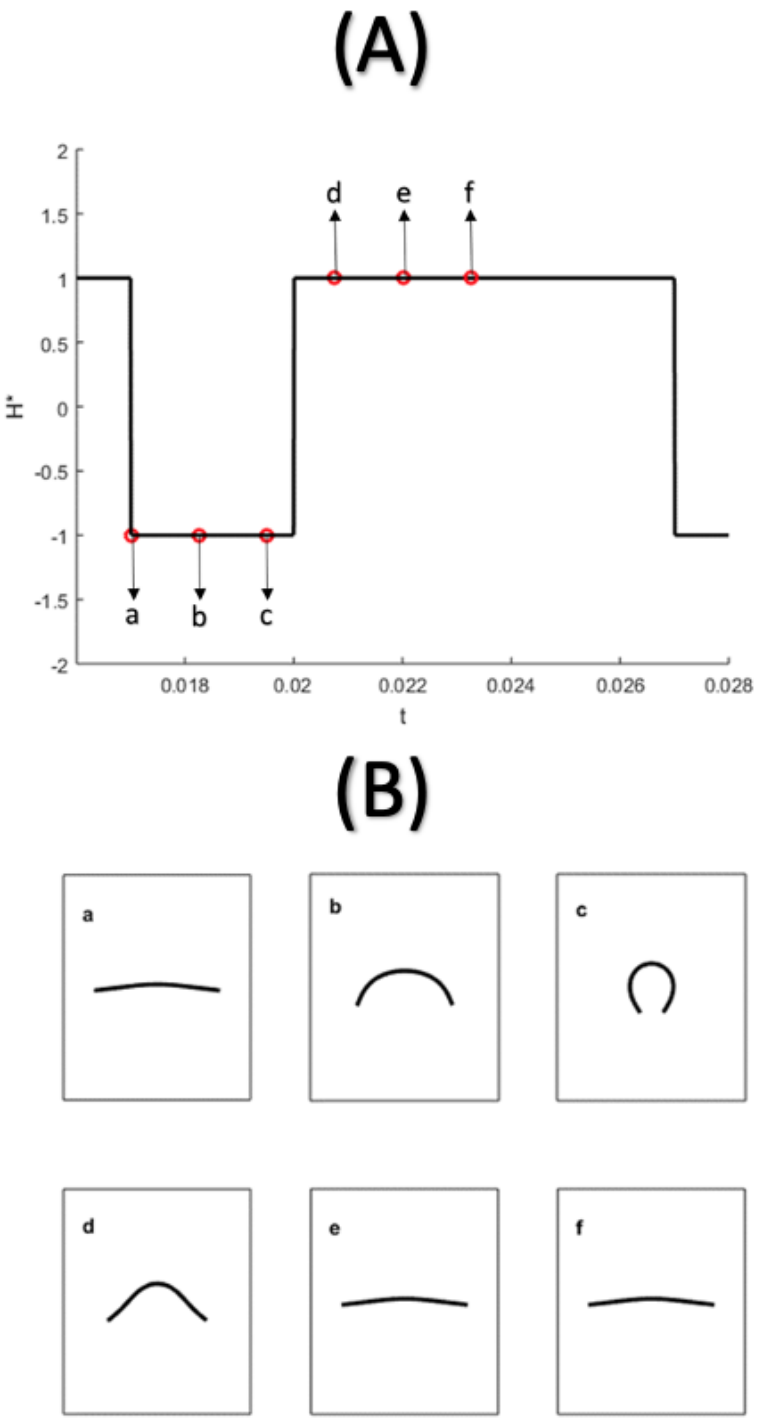

FIGURE 4.5: (A) Example of the field profile used in the numerical simulations, where H^* is a dimensionless field strength normalised by the maximum field strength H, time t is the dimensionless time. (B) Filament configurations obtained by numerical simulations at different locations within the period, which correspond to the marked field readings in (A).

It should be noted that experimentally, the S-like non-swimming filaments were also observed more frequently in the sample, when compared to the U-like. However, by looking at the filament which has a U-like deformation and propels, typically a defect was observed in the chain alignment, which results in a slightly curved shape. When comparing the experimentally observed relaxed U-deforming filament with the numerically defined condition, both shown in Fig.4.6(a), a good agreement can be seen, which confirms this to be a valid assumption. An example of the numerical simulations results obtained with the inital deformation condition added and without can be seen in Fig.4.6(b) and (c) respectively. The simulations were done using the same parameters for magnetoelastic number $Cm = 70$ and $T/\tau = 0.0052$. Hence, it can be proposed from experimental observations and numerical simulations that an initial filament shape with a slight deformation is required to result in the U-like swimming deformations.

The experimentally obtained results were compared with numerical simulations, as is shown in Fig.4.7. In Fig.4.7(a), the filament center of mass y-displacements obtained experimentally, as discussed in section 4.1, and scaled with the filament length L, are compared with numerically obtained results for three data sets - $L = 70$ μm & $f = 3$ Hz (diamonds), $L = 70$ μm & $f = 2.5$ Hz (squares) and $L = 59$ μm & $f = 3$ Hz (circles). The numerical simulations results were obtained by calculating the median obtained from the filament configurations. This corresponds to the experimentally obtained as $Cm = 70$, $T/\tau = 0.0039$ (black), $Cm = 70$, $T/\tau = 0.031$ (blue) and $Cm = 50$, $T/\tau = 0.0047$ (red) respectively. In a similar way to the experimental data processing, the velocities obtained by numerical simulation are calculated by a linear fit from the y-displacements over time relationship, and the results were compared for filaments with three different lengths, as shown in Fig.4.7(b). The data points for experimental velocity as shown in Fig.4.7(b), were previously shown in Fig.4.3(b), where here are scaled with L/τ on y-axis and τ on the x-axis, having filaments with length $L = 70$ μm (circle), $L = 59$ μm (square) and $L = 48$ μm (diamond). This corresponds to $Cm = 70$ (Blue), $Cm = 50$ (Black) and $Cm = 30$ (red) in numerical simulations respectively. The upper and lower limits donate the simulation results obtained by defining $\lambda = -0.4$ and $\lambda = -0.2$ respectively. From the numerical results presented in Fig.4.7(b), it can be seen that the decrease for frequency results in an increase of the velocity until a maximum is reached, followed by a decrease in the velocity. It should be noted here that the numerical model does not account for the magnetic interaction between the filament ends. Hence, it can be observed numerically that the filament tips overlap, resulting in a rapid decrease in the velocities.

From the velocities obtained experimentally, as presented in Fig.4.3(b), the calculated Reynolds number is found to be in the range of Re $\approx 10^{-4}$. This order of magnitude shows that the propulsion mechanism is solely driven

by the viscous forces, in Stokes hydrodynamics regime. Hence, the time reversibility to provide propulsion here is broken by the difference in the bending and relaxation shapes. Such can be seen by the difference of filament configuration of the two stages obtained experimentally as shown in Fig.4.8(a), where black diamond and red square points denote relaxation and bending stages respectively. As a result, the velocities are not linearly dependent on the frequency, but are also a function of the difference in the bending and relaxation time. To characterize this difference, the distance between the filament ends (d^*) in the x-direction is obtained, as shown in Fig.4.8(b) for a filament with length $L = 48\ \mu m$, $f = 6\ Hz$ (red points) and $f = 4.5\ Hz$ (blue points) at a fixed field strength of $H = 5.2$ Oe. This was also compared with numerical simulations, as shown by the dashed line, using the parameters $Cm = 30$, $\lambda = -0.2$, $T/\tau = 0.011$ (upper plot, compared to red points) and $T/\tau = 0.014$ (lower plot, compared to blue points).

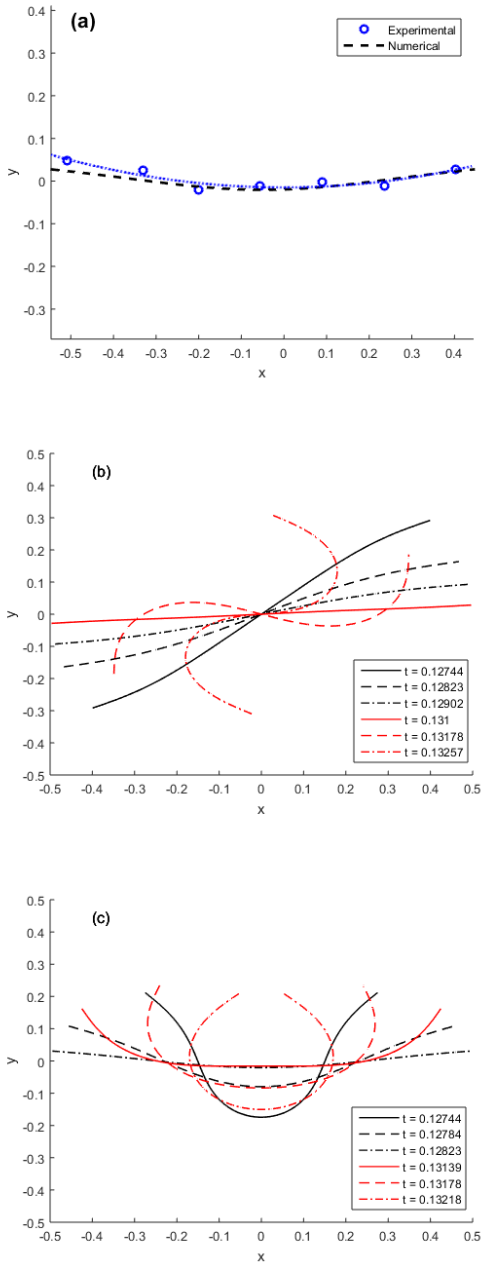

FIGURE 4.6: (a) - Relaxed filament shapes obtained from experimental data and numerical simulations. For dashed line, $Cm = 30$ and $T/\tau = 0.0013$. The circles denote particle centres of experimental data with $L = 48$ μm and $H = 5.2$ Oe. (b) & (c) - Filament shapes obtained by numerical simulations, red and black lines donates the configuration during bending and relaxation stage respectively within one period at different time moments t for $Cm = 70$ and $T/\tau = 0.0052$. (b) and (c) shows the difference of the results without and with the condition of curved initial shape respectively.

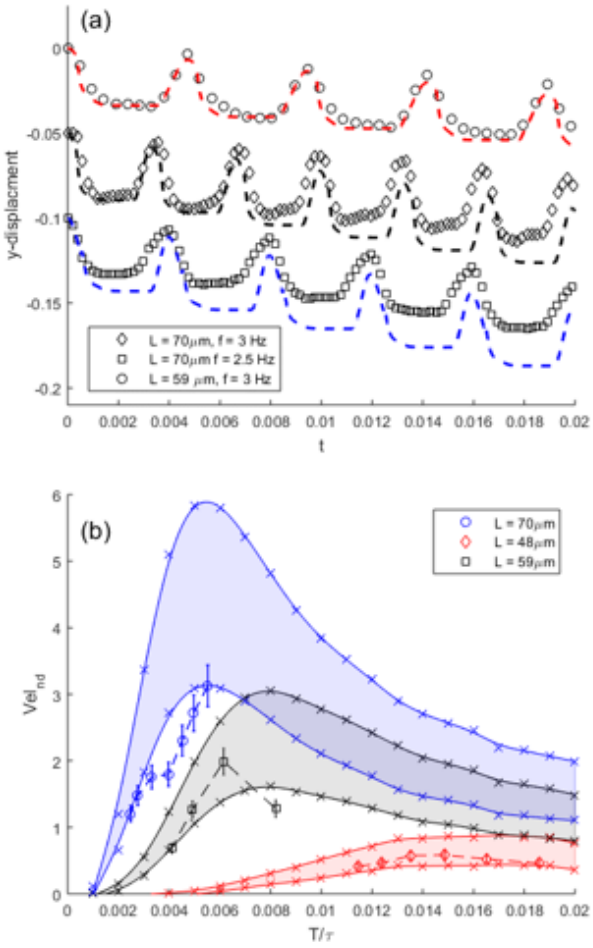

FIGURE 4.7: The filament centre of mass y-displacements as a function of time t. Circle, diamond and square points denote experimental data. The displacement is scaled by the filament length L on the y-axis and with $\tau = 54$ s (diamond and square) and 42 s (circle) on the x-axis. The dashed lines show the numerical filament centre dynamics that correspond to the experiment - $Cm = 70$, $T/\tau = 0.0039$ (black), $Cm = 70$, $T/\tau = 0.031$ (blue) and $Cm = 50$, $T/\tau = 0.0047$ (red). (b) Scatter points show velocity as a function of frequency for filaments with lengths $L = 48$ μm (diamond), 59 μm (circle) and 70 μm (square) scaled with L/τ on y-axis and τ on the x-axis, operating at a range of frequencies and fixed field strength $H = 5.2$ Oe. The solid lines represent numerical simulations over range of T/τ for $Cm = 70$ (Blue), $Cm = 50$ (Black) and $Cm = 30$ (red). Colored regions boundaries correspond to simulations by defining a slightly different $\lambda = -0.2$ and -0.4 for lower and upper lines respectively.

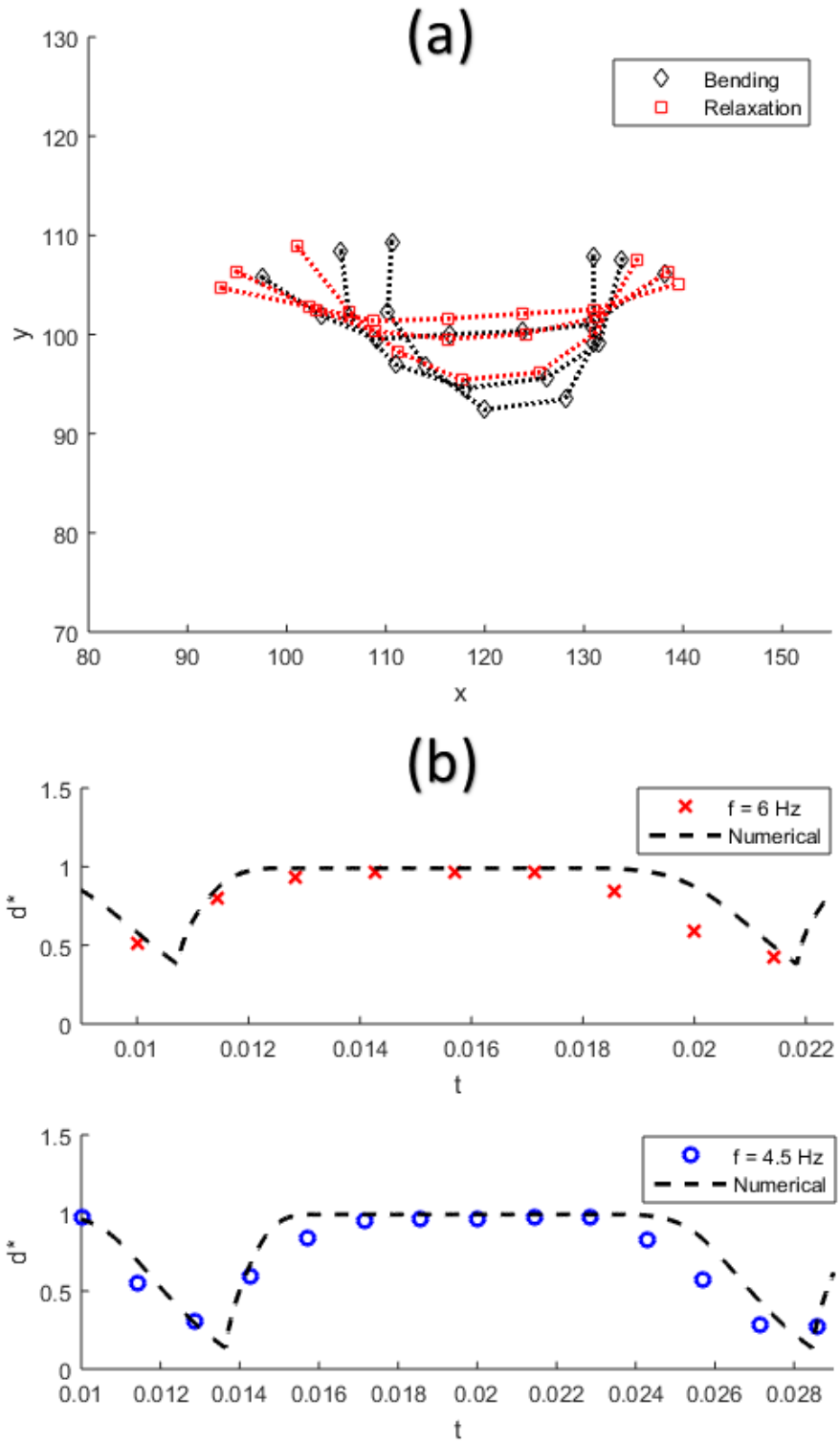

FIGURE 4.8: (a) Experimental filament configurations showing the difference in bending and relaxation stages at a constant time step over one period. (b) End to end x-displacement of filament tips (d^*) as a function of time t. Scatter points show experimental data for a filament with length $L = 48$ μm, $H = 5.2$ Oe, frequency $f = 6$ Hz (cross) and $f = 4.5$ (circle). Dashed lines show numerical simulation results for $Cm = 30$, $\lambda = -0.2$, $T/\tau = 0.011$ (upper plot) and $T/\tau = 0.014$ (lower plot).

4.3 Discussion

In this chapter, a possible swimming mechanism is presented, which is applicable for filaments made by linking ferromagnetic particles. The filament propels by breaking the time reversal symmetry due to the difference between bending and relaxation stages. This difference can be seen from the filament configurations obtained experimentally, as presented in Fig.4.8(a). The difference in the slopes between these two stages is observable from the d^* as a function of time as shown Fig.4.8(b).

Previous studies available on the investigation of the micro-swimmer swimming behaviour have been made using chains of paramagnetic particles. For example as presented in Ido et al. 2016; Li et al. 2013; Dreyfus et al. 2005. Unlike for the chains made of paramagnetic material, where its magnetization is zero once the field is switched off, spontaneously magnetized filaments buckle when the magnetic field is inverted, in a similar way to Euler instability of a rod under the compression Pilyugina et al. 2017. This buckling instability was experimentally realized by Ērglis et al. 2010, which results in a loop formation, having the filament move in the third dimension to align with the field. Numerically, such a swimmer design was first proposed by Belovs and Cēbers 2009, showing that the filament can propel with a periodic field inversion profile.

The choice of the duty cycle was made based on experimental observations, in order to have more swimming filaments in the sample as a whole. Initially, when the experiments were first conducted, the duty cycle was set to 70 %, the buckling instability was found to occur in the longer part of the period. However, in that case the filament was found to eventually flip and change its magnetization direction to align with the magnetic field direction in the longer stable part of the period. Different duty cycles were tried in the experiments. For example, at 50% square profile, the filament centre part was found to orient perpendicular with the magnetic field, while the ends try to follow the magnetic field direction in the opposite direction resulting in an S-like shape in 2D and 3D motions. It should be noted that from the numerical simulation results obtained when defining a higher duty cycle, for example at 70%, the filament swims with a U-like shape deformation and then ceases its swimming after the transition to an S-like shape. Simulations with 30% initially did not result in the swimming mode, as an immediate transition to an S-like shape was happening. After careful analysis of results, the initial curved shape was added to prevent the filament from completely relaxing before the start of each period. This is shown in Fig.4.6(a), and a defect in the filament was also observed experimentally. The cease of swimming and the transition to S-like deformations was also seen in numerical simulations by defining a sine wave inversion profile (Ērglis et al. 2011). Moreover, experimentally observed defect may be the result of applying the initial 70% unstable cycle, which may result in increased instant forces and damage the DNA fragments in the middle section to have a curved shape.

A good agreement is found when comparing experimental and numerical

results, as presented in Fig.4.7(b) for velocities of filaments with three different lengths over a range of frequencies. However, differences may arise as a result of the variation the filament physical properties, as for the bending modulus A_b due to unequal number of links between the particles or unequal section lengths. Moreover, in the numerical simulations the hydrodynamic drag coefficient ratio $\zeta_\perp / \zeta_\parallel$ was found to best fit with experimental velocities in the range of 1.2...1.4. Theoretically, $\zeta_\perp / \zeta_\parallel$ is ≈ 2 for an infinite rod (Powers 2010) and it differs when considering the filament length. Lower values were experimentally realised by applying the resistive force theory for swimmers at low Reynolds number. For example, a ratio of 1.7 and 1.4 was found for C.elegans and sperm cells respectively (Sznitman et al. 2010; Friedrich et al. 2010). Moreover, a ratio of 1.3 was found from experimental measurements for seven $2.8\mu m$ magnetic particle chain (Yang et al. 2017) and varies as a function of the number of linked particles. Hence, the experimentally obtained velocities can be better compared with the numerical simulation if the correction of drag coefficient is estimated for the number of particles used.

We can compare the swimming performance through the maximum achieved velocity with other designs presented in the literature. For example, $18\ \mu m s^{-1}$, $L = 38\ \mu m, f = 30\ Hz$ were measured for a rigid helical tail swimmer with an attached magnetic bead head and driven by a rotating field profile (Zhang et al. 2009b). A flexible propeller design actuated by a rotating field profile with a constant perpendicular field resulted in $21\ \mu m s^{-1}, L = 5.8\ \mu m, f = 21\ Hz$, as presented by Pak et al. 2011. The maximum velocity obtained here is $\approx 3\ \mu m s^{-1}$ which is lower than other designs of micro swimmers presented in the literature. However, the swimming velocity can be optimized by either modifying the magnetic field profile, to reduce the time for full relaxation before the bending stage. This can be seen in Fig.4.1(A) which corresponds to $\approx T^* = 0.67...1$.

The swimming velocity can be optimised by increasing the duty cycle, with considering the cease of swimming case discussed earlier. Moreover, unlike other micro-swimmers, it can be seen that the maximum velocities can be achieved at the lower frequencies ranges for a filament with the constant physical properties and operating at a fixed field strength, as shown in Fig.4.3(b), and the highest is reached at a maximum when the filament tips have a a distance before reaching to a ring like shape, which is shown for example in 4.4(a) and (b) respectively. Such higher performance in lower frequency regimes can give the advantage to achieve higher velocities by operation at higher frequencies and field strength. Scaling with numerical simulation results at $Cm = 70$ shown in Fig.4.3(b) for example: $v \approx 110 \mu m s^{-1}$ can be achieved for a filament with $L = 70\ \mu m$, $f = 50\ Hz$ and a field strength $H = 43\ Oe$, by designing a filament with a bending modulus $A_b = 3 \cdot 10^{-11} erg\ cm$. This estimate is comparable with the swimming velocity of *Chlamydomonos* micro algae, which have a similar propulsion mechanism (Drescher et al. 2010). Moreover, since the motion is perpendicular to the applied field direction, such a swimmer configuration may give the advantage in accurate

steering with less complicated field profile when compared to others mirco-robots (Li et al. 2013). However, the transient behaviour in changing the field direction is not studied here and may be an interesting topic for further studies.

Chapter 5

Local flow measurements

In this chapter, we present the velocity measurement around filaments under the action of a rotating magnetic field. In section 5.1, the experimental procedures are presented, followed by in section 5.2, the image processing tools used, PIV techniques adopted and the basis of material selection. In 5.3 and 5.4, the obtained velocity measurements with qualitative comparison with numerical simulation results and discussion of results are presented respectively. Part of the results from this chapter will be included in a publication.

5.1 Experimental procedures

Following the synthesis process as presented in section 2.3, 20 μl of the prepared filament sample is pipetted in the fluidic cell, and is then placed under the microscope for observation. The camera acquisition setting is set to double frame mode, at a frame rate of $1 - 6$ Hz while the inter-frame was set based on the operating frequency, which will be indicated in the following results section. For each experiment, double frames are acquired for filaments completing 9 to 25 rotations. The laser power was set to 100% with a maximum attenuator level of 25%. For higher attenuator levels the filament was observed to break. Similar to the procedures followed previously in section 3.2, a rotating field ($H = 17.2$ Oe, $f = 1$ Hz) is initially applied for a few minutes to allow the free particles to connect to filaments. During the rotations, filaments were found to slightly drift, probably as a result of wall interaction or the unsymmetrical centre of rotation. Examples of acquired images, for a filament with length $L = 73$ μm under a rotating field of strength $H = 34.4$ Oe and $f = 1$ Hz are shown in Fig.5.1. The acquisition frame rate FR is set to 6 Hz, and the inter-frame time between the first and second exposure, shown in Fig.5.1(a) and (b) respectively, is set to 15 ms. Fig.5.1(a),(c)-(f) shows the first exposed frame at different location within a period.

5.2 Data processing

Image processing was done using Matlab with the following steps:

- **PIV analysis**: the velocity field of the subsequent frames obtained by using the double exposure mode, at different location within the period

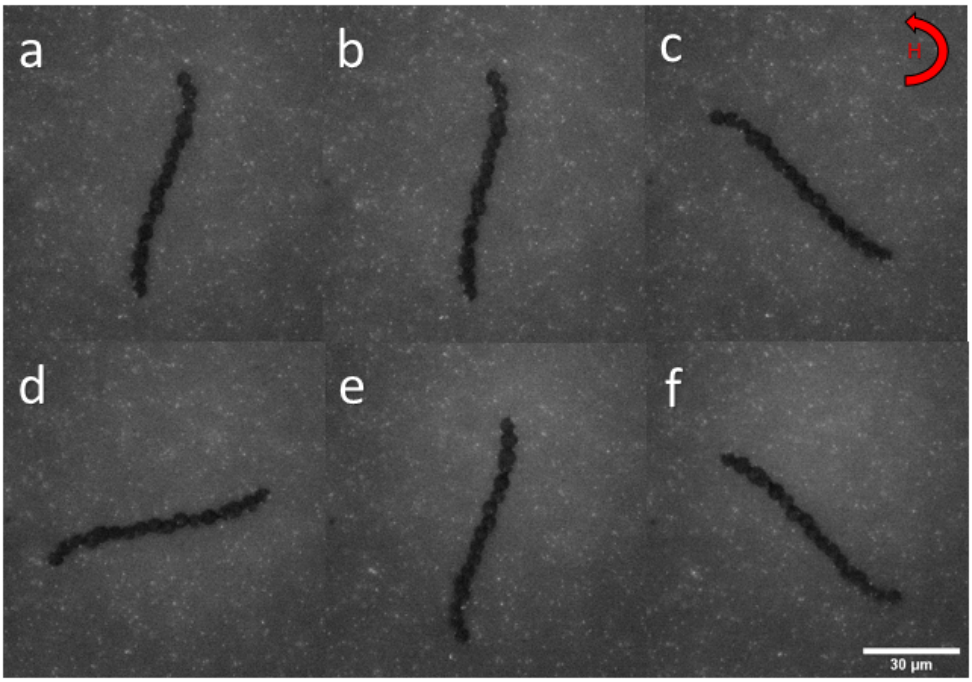

FIGURE 5.1: Examples of acquired images for local flow measurements. Filament under a rotating magnetic field of strength $H = 34.4$ Oe , frequency $f = 1$ Hz and $L = 73$ μm. (a) and (b) are the first and the second frame obtained by the double exposure mode with an inter-frame time of 15 ms. (a),(c)-(f) show the first frame acquired at different locations within one period, at a frame rate of 6 Hz.

are first obtained, using PIVlab tool; add-on package for Matlab which is used for cross-correlation calculations for PIV analysis, developed by Thielicke and Stamhuis 2014. Since the maximum achievable frame rate of double exposure mode is 6 Hz, the number of locations acquired is dependent of the field frequency.

- **Velocity fields translation and rotation**: the output data from PIVlab are then exported as a Matlab .mat files, containing (m x n) matrix of rows and columns for the calculated velocity fields based on the window size defined. To obtain the average velocity fields at single location (a reference frame which is chosen arbitrary, here based on the filament tangent angle at the centre). The velocity fields are first translated based on the movements of the filament centre point, then rotated by the angle difference between the tangent at filament centre point and the reference location.

- **Result processing and validation**: The results obtained are then averaged at a reference frame, flow characteristics such as velocity magnitude and vorticity are calculated, and validation tools are used to filter out-liner velocity vectors.

The velocity field are then obtained by solving the discrete cross-correlation, which reads,

$$C(m,n) = \sum_i \sum_j A(i,j)B(i-m, j-n) \tag{5.1}$$

where A and B are the interrogation areas for the correlated subsequent frames acquired from the double exposure mode and C is the cross-correlation matrix obtained for particle displacements. The discrete cross-correlation is commonly solved using two methods: the direct cross-correlation which computes the correlation matrix in a spacial domain by estimating the displacement vector analytically. The sizes of the interrogation areas can be different. The other method is by using the fast Fourier transform (FFT), which is selected in this work (Thielicke and Stamhuis 2014). More details on comparison and errors associated in using each method can be found in Thielicke 2014.

As discussed in Chapter 2.3, the concentration of tracer particles was chosen to obtain 10 to 25 particles per interrogation area. Here the particle density was approximated qualitatively using a tool implemented in Dantec Dynamics *Dynamic Studio* software. An example is shown in Fig.5.2. The location in this case is selected next to the filament, which is the area of interest shown in Fig.5.2(a). The particle count of 18 is given for a window area of 64×64 (Fig.5.2(b)) and particle count 12 is given for a window area 48×48 (Fig.5.2(c)).

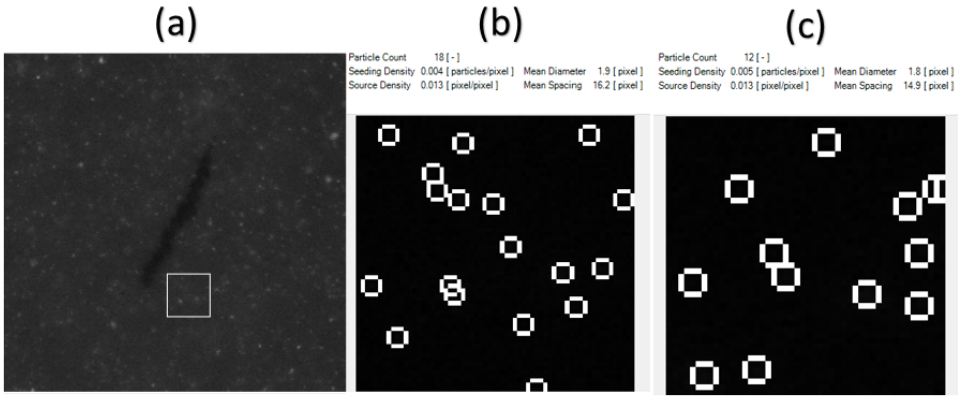

FIGURE 5.2: Example of the number of tracer particle estimation per interrogation area, (a) acquired image showing the area of interest, shown in white rectangle, (b) & (c) estimations obtained from defined window sizes of 64×64 and 48×48 respectively

Since the tracer particle distribution is not homogeneous, the concentration may vary from one location to another. Here, an approximate area of 40 x 40 pixel or more can be used to achieve the required average particle number per interrogation area of ≈ 10. It should be noted as observed experimentally, a higher particle concentration to achieve higher spatial resolution is limited in these experiments, due to the increased probability of the formation of tracer particle clusters in a short period of time once the rotating field is applied, resulting in the increase of image noise.

After the estimation of the tracer particle concentration, the defined interrogation area in the analysis is then based on the maximum tracer particle displacements, approximated from the filament displacements during the set inter-frame time. The maximum displacements were estimated by calculating the arc length of rod with radius r rotated by a known angle, which approximately corresponds to the fluid velocity at the filament interface. For example, for the filament shown in Fig.5.1 with a defined radius of $L/2$ and an inter-frame of 15 ms, the maximum calculated tip displacement is $\approx$ 15 pix. The desired window size to avoid in-plane loss of particle in cross correlation calculations, should be four times the max particle displacements (Raffel et al. 2007). Hence, a window size of 64 x 64 is defined, with a search area step of 50% the size of the window area. The resulting spatial resolution of about 7.5 μm. To further increase the spatial resolution and avoid in-plane losses, multi-pass approach is used, by adding a second pass, of size 32×32pix with a step of of 16 pix to correlate the lower displaced particles. This results in ≈ 4 μm spatial resolution and close to the diameter of the magnetic particles.

To check the applicability of the tracer particle size for their ability to follow with the flow, as presented in section 2.3, we need to characterize the velocity lag and calculate the value of Stokes number Skt, which is $\approx 10^{-10}$. Hence, the tracer particles can be safely assumed to follow fluid streamlines closely since $Stk << 0.1$ (Raffel et al. 2007).

Before cross-correlation calculations, the images were pre-processed using CLAHE tool in PIV lab package. This tool will narrow image intensity map based on their frequencies count, referred as (Contrast limited adaptive histogram equalization). This tool enhances the quality of PIV calculations for various application as presented by Thielicke 2014. Since the main interest here is the in-focus tracer particles, the equalisation tool was found to be appropriate in reducing associated noise. An example outcome of the processed experimental data is shown in Fig.5.3.

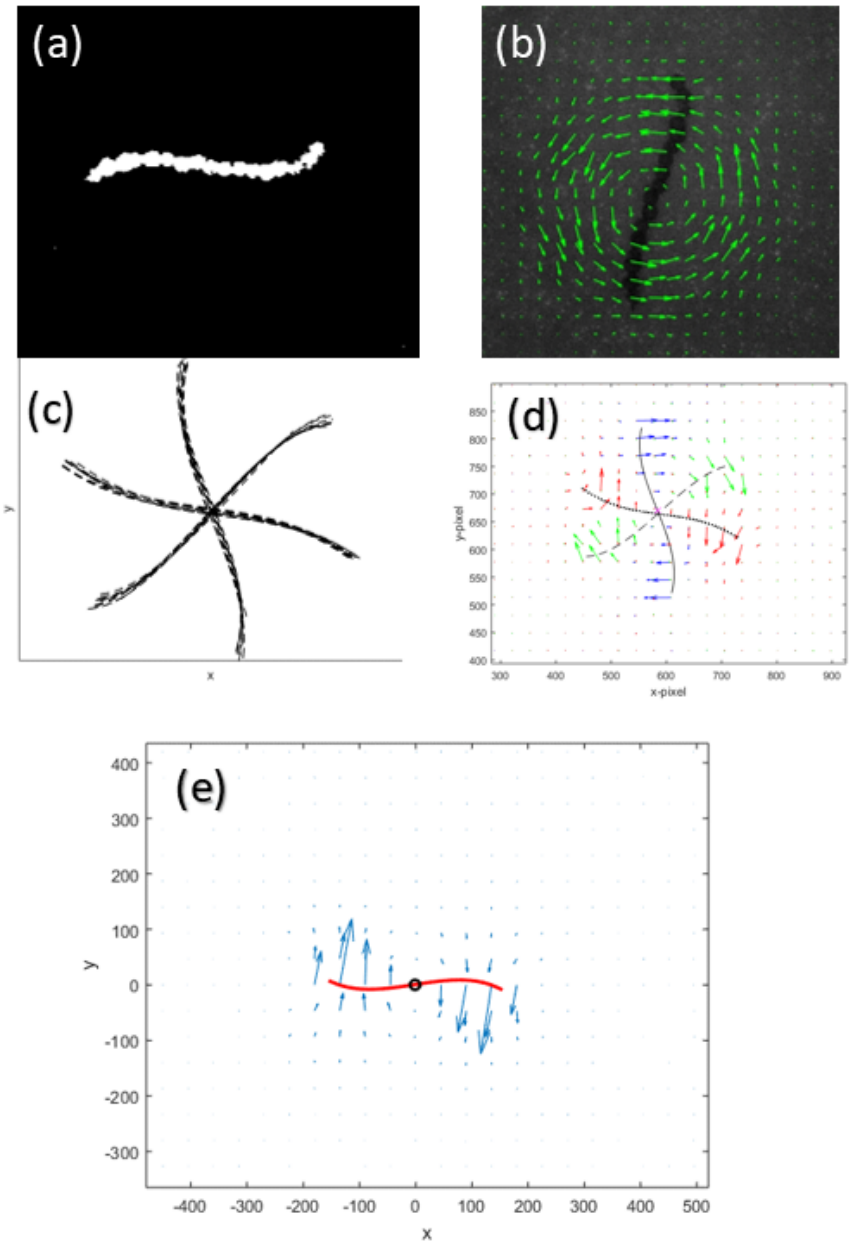

FIGURE 5.3: Example of processed data with the steps used for PIV analysis. (a) Obtained binary image. (b) Obtained original velocity field. (c) Detected centre lines for filament. (d) Velocity fields obtained are shown at three different locations within a period. (e) Results obtained for averaged velocity fields at a single location after translation and rotations.

To obtain the centre line, the filaments were first segmented using intensity threshold, resulting in a binary image. Then the filament centre line points are approximated by using an open source Matlab package, NRBC (Zeng et al. 2015), as presented in section 3.2. De-noising tool was used first

before centre line detection by Wiener filter method, to remove any interference of tracer particles located on the filament. An example of the obtained binary image and the detected centre lines for filament at three locations within the period is shown in Fig5.3(a) and (c) respectively.

As discussed previously, the correlation calculations was done with defined window areas of 64×64 pix, with a step of 32 pix and 32×32 pix second pass with a step of 16 pix. An example of the obtained original velocity field is shown in Fig5.3(b). In the results presented below, the velocity fields are filtered by removing any velocities vectors which exceed the maximum filament estimated displacement. In Fig5.3(d), an example of velocity fields obtained are shown at three different locations within a period. It should be noted that no smoothing tools for the velocity fields are used throughout this work, not to loose spatial resolution.

Rotation and translations of velocity fields obtained to the selected frame of reference was done by the following steps. The spacial resolution was first enhanced by using gridded data interpolation function, to allow a precise identification for the desired point in the matrix for transformations. The centre line points are fitted with a polynomial function, where the centre point and the tangent angle ϑ at the centre is estimated. Grid translation is done based on the mid point of the fitted centreline and then rotated by the calculated angle ϑ with respect to the horizontal x-direction axis. The new grid location is then found using scattered interpolant function. An example of results obtained for averaged velocity fields at a single location after translation and rotations is shown in figure Fig5.3(e).

5.3 Results

The experiments were done for filaments of three different lengths L, under a fixed field strength $H = 34.4$ Oe and at a range of frequencies $f = 1 \rightarrow 5$ Hz. An example of the velocity fields and their magnitude normalised by the calculated velocity of a rotating rod (v_{rod}) is shown in Fig.5.4 for a filament with $L = 73$ μm, and frequencies $f = 1 \rightarrow 5$ Hz (a-e) and in Fig.5.5 for filaments with $L = 64$ μm & $L = 48$ μm for frequencies $f = 1 \rightarrow 3$ Hz (a-c) & (d-f) respectively, under a rotating field of strength $H = 34.4$ Oe.

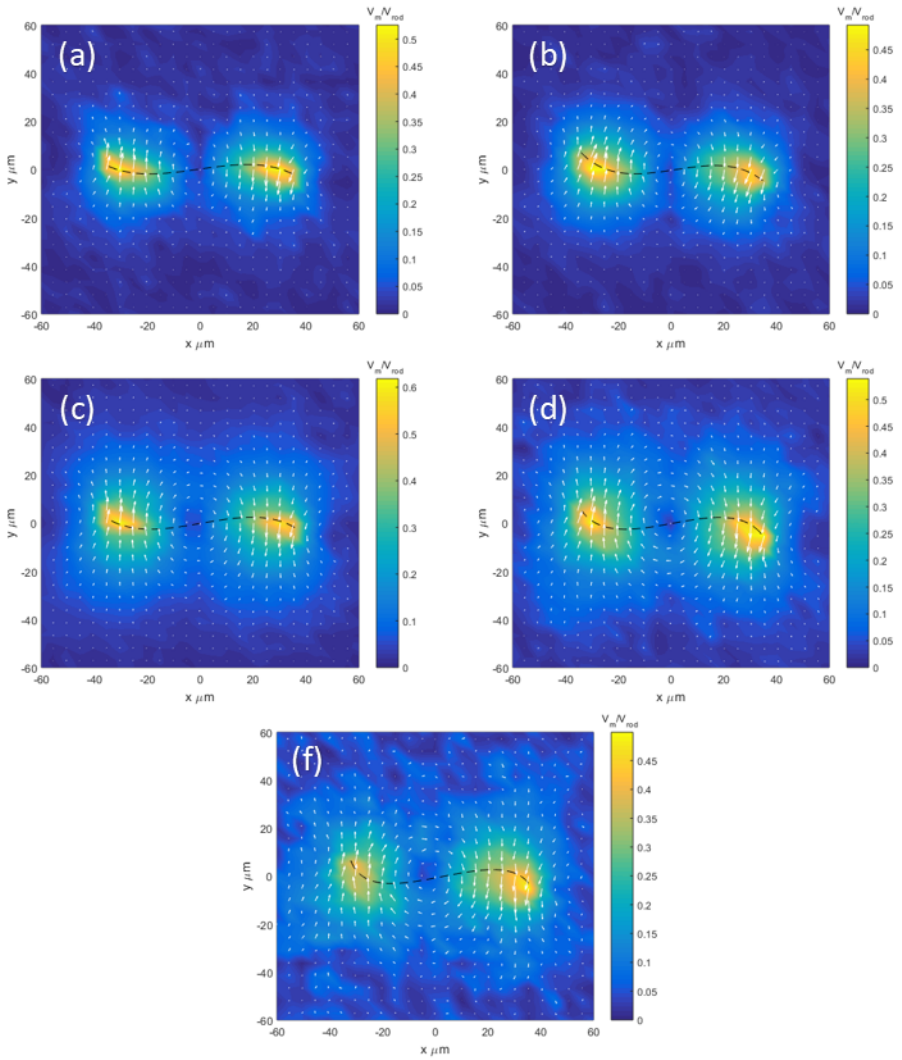

FIGURE 5.4: Velocity field obtained for a filament with length $L = 73$ μm, field strength $H = 34.4$ Oe and operating at frequency f: (a) 1 Hz, (b) 2 Hz, (c) 3 Hz, (d) 4 Hz and (e) 5 Hz

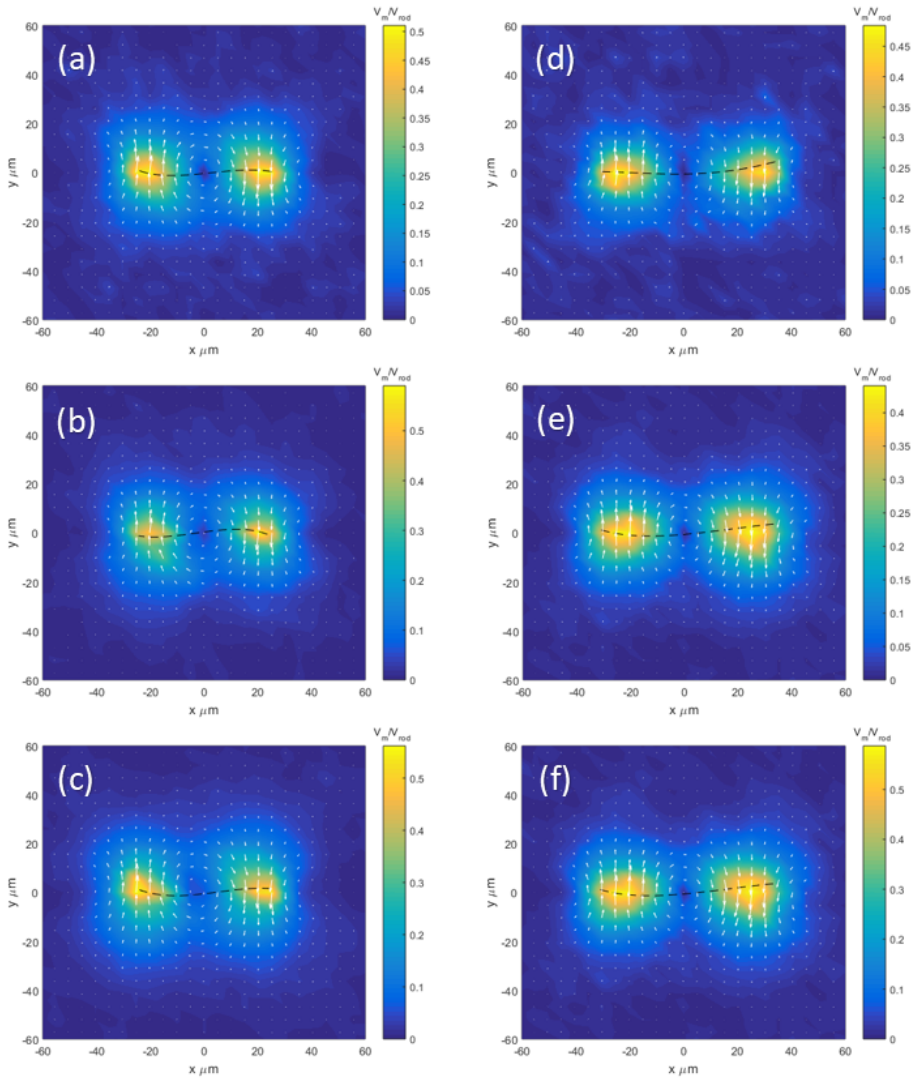

FIGURE 5.5: Velocity field obtained for filaments with two different lengths under a fixed field strength $H = 34.4$ Oe: (a -c) $L = 48$ μm, frequency f: (a) 1 Hz, (b) 2 Hz, (c) 3 Hz. (d -f) $L = 64$ μm, frequencies f: (d) 1 Hz, (e) 2 Hz, (f) 3 Hz.

As shown in Fig.5.4, increasing the frequency will result in the increase of the filament minor S-like deformations, and an increase of velocity magnitude. Moreover, it is observed that the maximum velocity magnitude is located near the filament tips. Slight change in the maximum velocities was found when comparing the magnitude at the filament tips, which maybe a result of unsymmetrical rotations. The flow profile obtained for the velocity magnitude v_m along the filament center line (f_L) is shown in Fig.5.6, for a filament with length $L = 73$ μm, $H = 34.4$ Oe and $f = 1 \rightarrow 3$ Hz for (a $\rightarrow$ c) respectively.

From the results shown in Fig.5.6, it is found that the maximum velocities

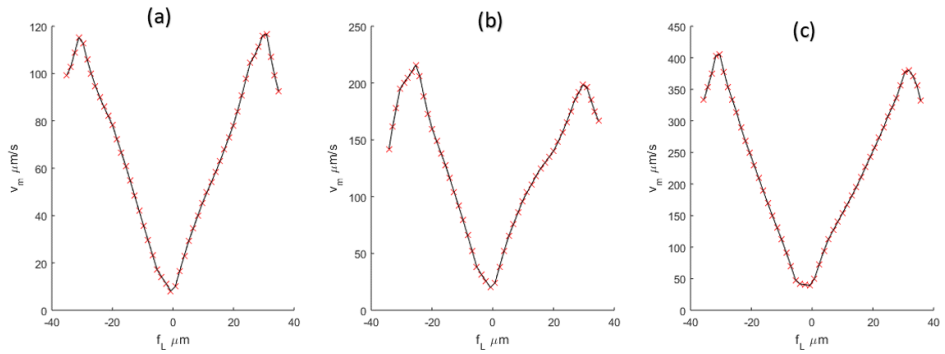

FIGURE 5.6: Flow profile of the velocity v_m along the centre line of a filament f_L with length L = 73 μm, frequency f: (a) = 1 Hz, (b) = 2 Hz and (c) = 3 Hz field strength H = 34.4 Oe

are located in the middle of the bent part of the filament close to the tip. The velocities then decrease in a linear behaviour until reaching zero at the centre of rotation. Beyond the maximum velocity towards the filament tip, the decrease of velocity was also found to be linear. This flow profile was found to have a similar behaviour at a range of frequencies, as shown in Fig.5.6(a-c), for a filament with an observable S-like deformation.

To characterise the flow at different frequencies, the sum and maximum velocities were obtained for filaments with different length operating at a field strength of 34.4 Oe. The results obtained are shown in Fig.5.7. It can be seen that the increase of frequency will result in an increase in the maximum velocities, as shown in Fig.5.7(a). This increase is higher for longer filaments, and was found to have a linear behaviour for filaments with length $L = 48$ μm and $L = 64$ μm, shown in the blue and red dashed lines respectively. To characterize how much fluid is moving, the sum of velocity V_{sum} is estimated by adding all velocity magnitudes in the field of view. The relationship obtained for V_{sum} vs frequency is shown in figure Fig.5.7(b). It was observed that the increase of frequency will result in a higher sum of velocity magnitude V_{sum} as shown by black and blue dashed lines for filaments with $L = 73$ μm and $L = 48$ μm respectively. However, for filament with $L = 64$ μm, a further increase of V_{sum} was not observed after a frequency of 3 Hz.

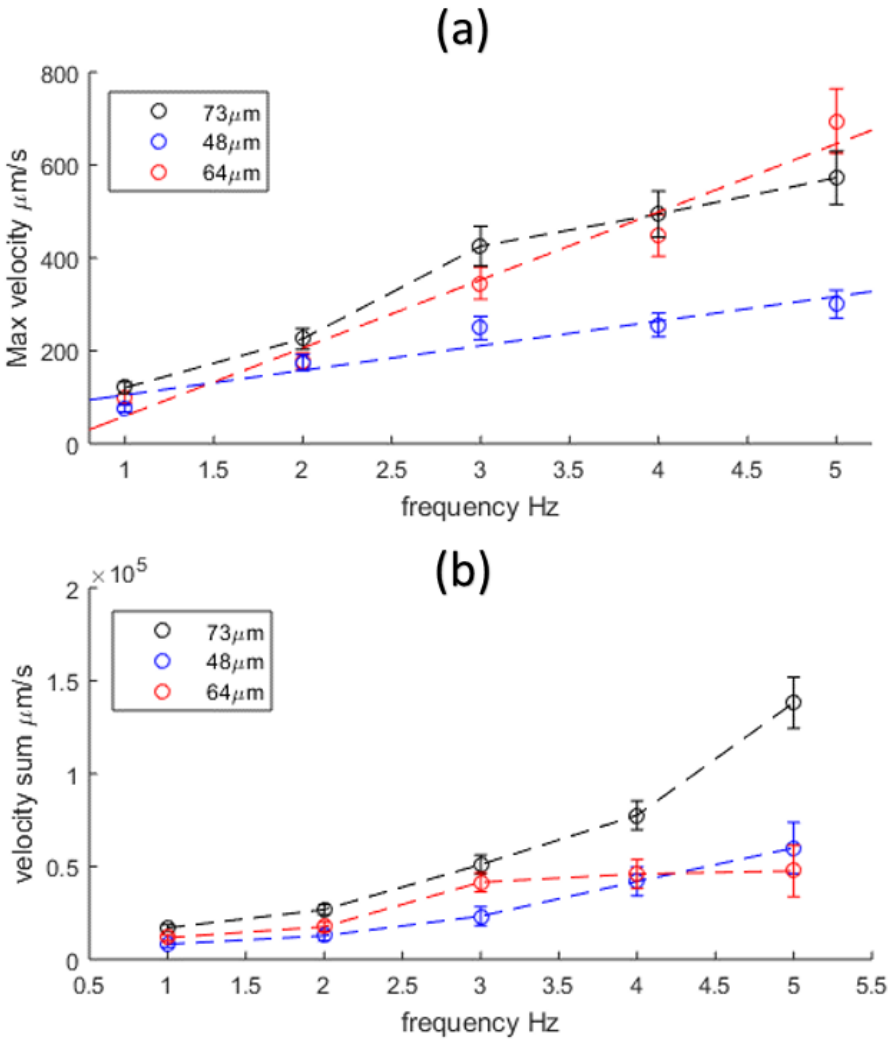

FIGURE 5.7: Maximum V_{max} & sum V_{sum} velocities as a function of frequency are shown in (a) and (b) respectively for filaments with length $L = 73$ μm (black circles),$L = 64$ μm (red circles) and $L = 48$ μm (blue circles), under a rotating field of strength $H = 34.4$ Oe

As mentioned in chapter 1.4, far field velocities become important to consider for filament interactions with other filaments or with other solid boundaries. The far field velocities here are characterised by the spatial velocity decay as a function of distance R away from the filament. Here the y-component velocity v is read along the x-axis from the filament maximum velocity near the filament tip (x_t). The points are then fitted with

$$v = \frac{a}{(R - x_t)^n}, \tag{5.2}$$

using n = 1,2,3. The results obtained for a filament with length L = 73 μm under a field strength H = 34.4 Oe are shown in Fig.5.8, operating at different frequencies. The results obtained shows qualitatively that the best fit is obtained for a fluid velocity decay as a function of $1/R^2$, (shown as the green lines), which can be described to have a flow singularity of force dipole.

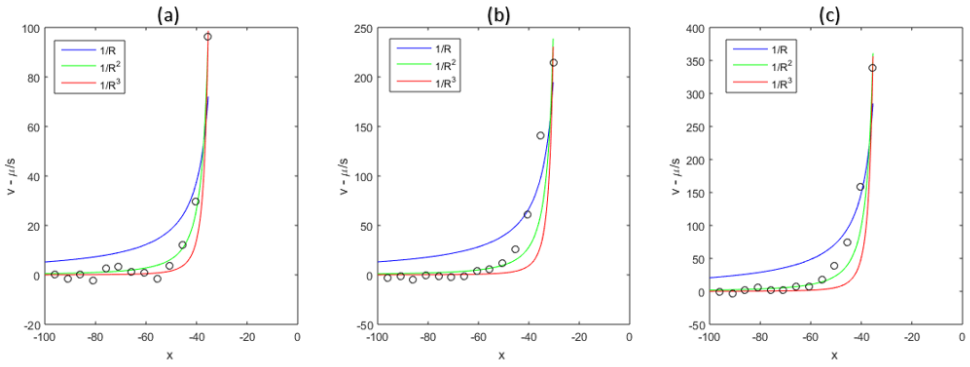

FIGURE 5.8: The fluid velocity (v) along the x-axis from the filament tip away from the filament, the black circles are read from experimental data. The lines shows the best fit obtained at different power of R, for a filament with $L = 73$ μm under a field strength $H = 34.4$ Oe and frequency for (a-c) is 1...3 Hz respectively.

The measurements are done at Stokes regime with a predictable similarity for flow behavior around the filament at different locations within the period. Hence, the quality of data processing for averaging at different locations was investigated qualitatively by observing the standard deviation of velocity fields around the filament over multiple of rotations. An example is shown in Fig.5.9(a-d), where the red and blue arrows correspond to the upper and lower standard deviations respectively, from the average over multiple rotations (shown as black arrows), for a filament with a length $L = 73$ μm under a field strength $H = 34.4$ Oe, operating at different frequencies. Moreover, the mean velocity magnitude was calculated to check the satisfaction of continuity. The results obtained are shown in Fig.5.9(e), to observe the deviations from zero considering the sign change of velocity along the filament.

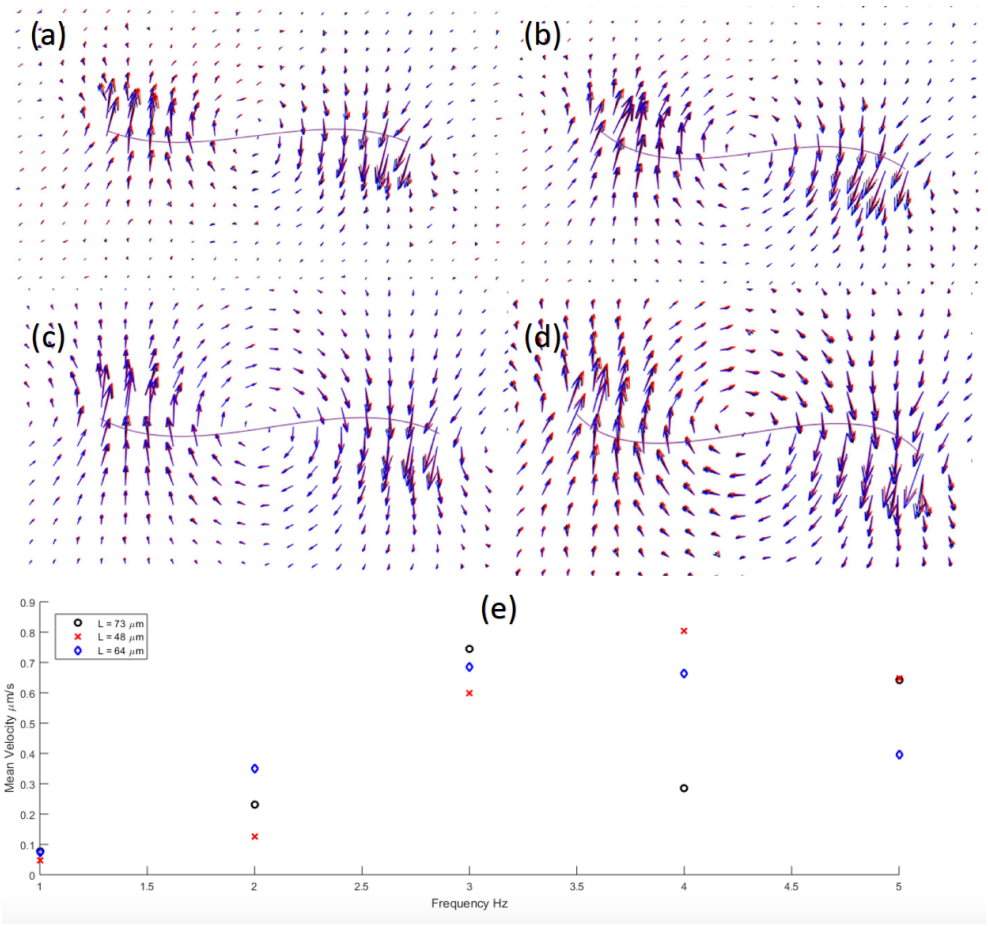

FIGURE 5.9: Velocity field for filament with $L = 73\ \mu$ m under a field strength $H = 34.4$ Oe and frequency $f = (1 \rightarrow 4)$ Hz for (a-d) respectively, averaged at locations with the period. (e) Mean velocity obtained around for different filaments with $L = 73\ \mu$m (circle), $L = 48\ \mu$m (cross) and $L = 48\ \mu$m (cross) and $H = 34.4$ Oe

As presented in section 1.4, Stokes equations are linear and can be solved in terms of fundamental solutions (Stokeslets) to find the flow fields around the filament. To avoid numerical issues of divergent flow located on a point source (Zhao et al. 2019), the method of regularized Stokeslets is used here with a regularization parameter $\delta = r/L$, defined as the ratio of particle radius to the filament length. The fluid velocity in the plane of a rotating field in dimensionless units reads (Olson et al. 2013; Zhao et al. 2019)

$$\vec{v}(\vec{r}) = \int_0^1 dl' \Big(\frac{h_1(|\vec{r} - \vec{r}(l')|}{|\vec{r} - \vec{r}(l')|} \frac{d\vec{F}(l')}{dl'} + \frac{(\vec{r} - \vec{r}(l'))(d\vec{F}(l')/dl' \cdot (\vec{r} - \vec{r}(l'))}{|\vec{r} - \vec{r}(l')|^3} h_2(|\vec{r} - \vec{r}(l')|) \Big) \tag{5.3}$$

where

$$h_1(r) = r\Big(\frac{1}{(r^2 + \delta^2)^{1/2}} + \frac{\delta^2}{(r^2 + \delta^2)^{3/2}} \Big) \tag{5.4}$$

and

$$h_2(r) = r\Big(\frac{1}{(r^2+\delta^2)^{1/2}} - \frac{\delta^2}{(r^2+\delta^2)^{3/2)}}\Big) \tag{5.5}$$

where the force $\vec{F}$ is obtained from the modified Kirchhoff rod model as presented in chapter 1.3.

An example of the obtained numerical results is shown in Fig.5.10, which correspond to the experimental data for the filaments, shown in Fig.5.4 & 5.5. Similar to the numerical simulations presented in chapter 3.1 & 3.2, scaling with experimental data is done by magneto-elastic Cm and the elastic relaxation time $\omega\tau$, where $\omega = 2\pi f$. The fluid velocity is scaled with L/τ and dimensionless length with filament length L. In Fig.5.10(a-c), the flow fields results are shown, obtained by defining $Cm = 288$ and $\omega\tau$ for (a) 640, (b) 1281 and (c) 1921, which correspond to frequencies $f = 1...3$ for a filament with length $L = 73$ μm from the experimental data. The velocity magnitude is scaled with L/τ and normalised by the maximum calculated velocity of a rotating rod (v_{rod}),estimated theoretically. Fig.5.10 (d) and (e) shows numerical results of the maximum and sum of velocity obtained over a range of frequencies, which are scaled with experimental data shown in Fig.5.7, by defining $Cm = 288$ (black), 120 (blue) and 220 (red) which correspond to $\tau = 102$, 17.5 and 60 s respectively. The results for the flow profile across the filament centre line is shown in Fig.5.10(f), by defining $Cm = 288$ and $\omega\tau = 640$, for the relationship between the velocity magnitude V_m on the y-axis and filament centre line scaled with the filament length, which corresponds to the experimental data shown in Fig.5.6(a). This shows that experimental data are in good qualitative agreement with numerical results.

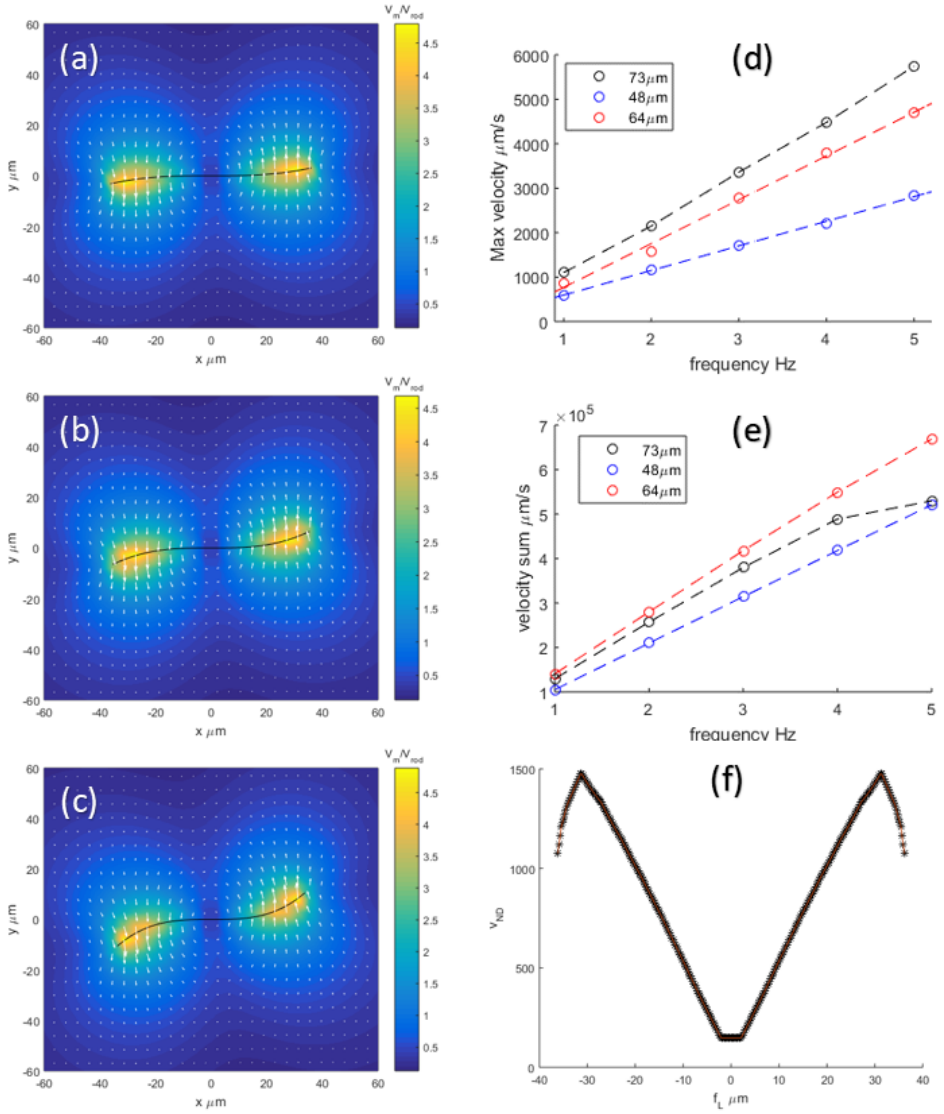

FIGURE 5.10: Example for numerical results obtained using parameters which corresponds the experimental data for a filament shown in Fig.5.4 and 5.5. (a-c): flow fields around the filament obtained using $Cm = 288$ and $\omega\tau$ for (a) 640, (b) 1281 and (c) 1921. (d) and (e) show numerical results of the maximum and sum of velocity obtained over a rage of frequencies, which are scaled with experimental data shown in Fig.5.7, by defining $Cm = 288$ (black), 120 (blue) and 220 (red) which correspond to $\tau = 102$, 17.5 and 60 s respectively. (f): Flow profile across the filament centre line by defining $Cm = 288$ and $\omega\tau = 640$.

.

5.4 Discussion

In this chapter, velocity measurements were made to investigate the flow behaviour around the filaments under the action of rotating magnetic field, using μ-PIV technique. From the experimental procedures and analysis, an optimal tracer particle concentration is proposed here, to satisfy the minimum desired particle number per interrogation area while considering the particle aggregations during the time of experiments, which can results in an increased noise to signal ratio. Moreover, laser power settings should be chosen carefully to avoid the DNA fragments breakage, which was found here to run the laser on full power while setting around 25% attenuator level.

From the results shown in Fig.5.4 and Fig.5.5, it can be seen that behaviour of the flow is similar when increasing the frequency under a fixed field strength, with an increase in the velocity magnitude. The flow profile read from the filament centreline as shown in Fig.5.6, it is observed that the maximum achieved resultant velocities are located in the middle of the curved part close to the tip, for an observable S-like shape deformed filament. Moreover, the velocity profile in the unbent section of the filament was found to have a linear relationship, similar to the expected behaviour of a rotating rigid rod. From Fig.5.8, it can be seen that far field velocities away from the filament decays spatially as a function of $1/R^2$, for example can be described to have a flow singularity of either a force dipole or rotlet, which have a similar spatial decay (Lauga 2020).

The maximum velocity magnitude was found to be around half the expected from a rotating rigid rod, with assuming no slip condition by having the velocity at the filament boundary is equal to the fluid velocity. Here, a lower maximum measured velocities are expected compared to a rigid rod since the maximum velocities is not located at the filament tip. Moreover, as the calculated from the signals of tracer particles are not located on the filament but closely around it and the fluid velocities decay as $1/R^2$, a lower maximum velocity is expected. It should be noted as observed experimentally that increasing the frequency results in rotations at larger distance from wall bottom. It may be suggested that this effect is due to the interaction with wall.

By comparing the flow fields obtained experimentally with numerical simulations, it can be seen that their behaviour are in good agreement qualitatively. This can be seen by comparing Fig.5.4 & 5.10(a-c). Similarly, good agreement was found by considering the flow profile across the filament centre as shown in Fig.5.6(a) & 5.10(f). However, the velocity magnitude was found to be about one order of magnitude higher for numerically obtained results. A further study of the numerical method used or quantitative comparison with experimental results here is not in the scope of this work. However, further investigation can be suggested as a future work by varying parameters as the bending modulus A_b or magnetisation per unit length M. Moreover, solving using regularized Stokeslets method introduces the regularization parameter δ, which is assumed here to be the particle diameter

to filament length ratio. Simulations can be done for a wider range δ to investigate difference of flow behaviour and its applicability on this system. The difference in velocity may be explained by using higher value of δ which reduces the accuracy of results (Zhao et al. 2019). Or as a result of wall interaction that are not considered in the model.

As discussed in section 1.6, mixing efficiency can be linked to Mason number Ma, which is a function of the frequency f at a fixed field strength. From the results obtained from Fig.5.7(b) and for frequencies below critical, it can be seen that the sum of flow increases in a higher slope for filament with length $L = 73$ μm and $L = 48$ μm in the range of investigated frequencies. Hence, an increase with the mixing efficiency. For a higher rotating frequencies where the filament becomes more deformed, a reduction of sum of velocity was noticed numerically as shown in Fig.5.10(e). Hence, it can be proposed that there is an optimal frequency for mixing with the higher efficiency and its deviation from linear dependence. This was realised experimentally by Biswal and Gast 2004, where mixing rate drops with the increase with frequency for filaments with various length in the sample.

Chapter 6

Conclusions and further work suggestions

In this work, we experimentally study the dynamics of filaments made from ferromagnetic particles under the action of both rotating and pulsed magnetic fields. The filaments are synthesised using magnetic particles functionalized by strepdavidin linked with biotinylated DNA fragments under a static magnetic field. From the adapted synthesis method, the formation criteria were found to provide a wide distribution of filaments where shapes like particle clusters, filaments and unconnected particles were observed.

The filament behaviour under a rotating field can be divided in to two regimes: when field frequency is below a critical frequency ($f < f_c$) and above it ($f > f_c$) as follows,

- When $f < f_c$, the filaments were observed to rotate synchronously with the magnetic field and deform with an S-like shape, having the filament ends bend in the opposite directions. In this regime, the filament behaviour was characterised by measuring the angle between the tangent angle at the centre and the magnetic field direction (ϑ), which is a measure of lag to follow the magnetic field. ϑ angle was found to increase when operating at higher frequency, lower magnetic strength and when the filament length is longer. Moreover, the ϑ deviates from linear dependency with the increase of frequency.

- When $f > f_c$, the filament was found to move out of the rotating plane. It had a circular tip trajectory in the third dimension, while having a synchronous rotation with the magnetic field. This transition to a 3D motion was observed experimentally to happen when the filament tangent angle at the centre (ϑ) reaches an angle of around 90 deg. The filament deformation at this regime was characterised by calculating the ratio between the radius of tip trajectory and the filament length (R/L). Beyond f_c, R/L was found to decrease rapidly with the increase of frequency, until reaching $f/f_c = 2$.

Numerical simulations were made using Kirchhoff rod theory modified to include magnetic energy. To account for any system instabilities, perturbation is added to the model by defining a slight elevation in the z-axis as an initial filament configuration for one of the filament tips. Good agreement

between experimental and numerical obtained results was found both quantitatively by comparing with R/L and qualitatively through shapes of the deformed filaments. The filament magnetization per unit length M was estimated from both low deformation dynamics and fit of R/L as a function of frequency f for experimental and numerical results. The estimated values of M were found to be in good agreement with the measurements of magnetic properties made for similar particles presented in the literature. The bending modulus A_b was estimated by registering the relaxation of filament configurations from an initially deformed filament. The results obtained show that the filament flexibility arises from the DNA linkers and not from the magnetic interactions. Moreover, A_b obtained from R/L vs f fit with numerical simulations is not far from the one obtained by relaxation dynamics. However, this shows that the elasticity of each filament can slightly differ using this synthesis methodology.

We experimentally validate a new propulsion mechanism, based on the buckling instability present when the magnetic field is inverted. Under a pulse field profile, the filament was found to have either an S-like or U-like shape deformations. In the latter case the filaments propel in a direction perpendicular to the applied magnetic field. The swimming mechanism is divided into bending and relaxation stages, the time difference between these two stages is responsible for filament propulsion. It is found that when reducing the time within the period of bending stage, it is more likely to observe U-like deformations in the sample. The optimal profile was found when the bending stage time is 30% within the period. Numerical results were obtained by adding a condition to the model, preventing the filament from complete relaxation before the bending stage and have a slightly curved shape. This was based on experimentally relaxed filament shapes. The velocities and filament configurations were found to be in good agreement when comparing numerical with experimental obtained results, by defining the hydrodynamic coefficient $\zeta_\perp / \zeta_\parallel$ in the range of 1.2 to 1.4., opposite to the value 2 for an infinite rod.

Flow measurements were made using μ-PIV technique, to investigate the flow behaviour around a deformed filament under the action of a rotating magnetic field. A similar flow behaviour around the filaments were obtained over a range of frequencies. The velocity magnitude read across the filament centreline increases linearly from the center of rotation until reaching the bent part of ´S´-like deformed filament, then decreases until reaching the filament tip. From experimental data, the far field velocities are best described by having a spatial decay rate of $1/R^2$. It was also observed experimentally that the distance from the wall bottom is larger with the increase of frequency. Numerical results were obtained using regularized Stokeslets method and showed good qualitative agreement with experimentally obtained results.

A summary of conclusions based on the thesis objectives as follows,

- It is found that under the action of rotating field ferromagnetic filaments

undergo two regimes: at lower frequency, the filament rotates synchronously with the rotating field and remains in its plane. At higher frequency, the filament moves out of the rotating plane in the third dimension with a circular anti-phase tip trajectory.

- It is observed under the action of periodic magnetic field inversion, the filament propels in the direction perpendicular to the field direction. However, initial filament configuration and specific field profile is required to achieve propulsion.
- It is deduced that μ-PIV technique can be used to determine the flow characteristics around the filaments. The results were validated both quantitatively by continuity of flow and qualitatively by numerical simulations.

6.1 Thesis

As a summary of the results, the author proposes a thesis: flexible ferromagnetic filaments can be useful for the design and development of soft microrobotics. Applications are foreseen in biomedicine and biotechnology.

6.2 Suggestion for further work

- In the adopted filament synthesis method, various shapes can be formed, such as particle chains or clusters (as explained in chapter 2). Hence, it is suggested to have further insight on filament formation method and check the possibility to control the filament outcome parameters, such as length.
- Investigate the applicability for using different DNA fragments length and find the effect of linker size on filament flexibility.
- Here we experimentally validate a swimming mechanism for chains made of ferromagnetic particles. Further work can be done as study the transient behaviour when changing swimming direction, the achieved swimming velocities when using filaments with physical parameters as proposed in section 4.3 and the filament behaviour in a microchannel with a flow.

Bibliography

Ahmed, Daniel, Cornel Dillinger, Ayoung Hong, and Bradley J. Nelson (2017). "Artificial Acousto-Magnetic Soft Microswimmers". In: *Advanced Materials Technologies* 2.7, p. 1700050. DOI: 10.1002/admt.201700050.

Atherton, Tim and D.J. Kerbyson (Dec. 2001). "Size invariant circle detection". In: *Image and Vision Computing* 17, pp. 795–803. DOI: 10.1016/S0262-8856(98)00160-7.

Barreto, Darius Diogo, Shashank Saxena, and Ajeet Kumar (2022). "A magnetoelastic theory for Kirchhoff rods having uniformly distributed paramagnetic inclusions and its buckling". In: *International Journal of Solids and Structures* 234-235, p. 111147. DOI: j.ijsolstr.2021.111147.

Batchelor, G. K. (1970). "Slender-body theory for particles of arbitrary cross-section in Stokes flow". In: *Journal of Fluid Mechanics* 44.3, pp. 419–440. DOI: 10.1017/S002211207000191X.

Belovs, M. and A. Cēbers (May 2009). "Ferromagnetic microswimmer". In: *Phys. Rev. E* 79 (5), p. 051503. DOI: 10.1103/PhysRevE.79.051503.

Belska, Paula (2018). In: *Internship report - Magnetic filament formation*. (unpublished).

Bhagat, Ali Asgar S, Erik T K Peterson, and Ian Papautsky (2007). "A passive planar micromixer with obstructions for mixing at low Reynolds numbers". In: *Journal of Micromechanics and Microengineering* 17.5, pp. 1017–1024. DOI: 10.1088/0960-1317/17/5/023.

Biswal, Sibani Lisa and Alice P. Gast (Aug. 2003). "Mechanics of semiflexible chains formed by poly(ethylene glycol)-linked paramagnetic particles". In: *Phys. Rev. E* 68 (2), p. 021402. DOI: 10.1103/PhysRevE.68.021402.

— (2004). "Micromixing with Linked Chains of Paramagnetic Particles". In: *Analytical Chemistry* 76.21, pp. 6448–6455. DOI: 10.1021/ac0494580.

Brasovs, Artis, Jānis Cīmurs, Kaspars Ērglis, Andris Zeltins, Jean-Francois Berret, and Andrejs Cēbers (2015). "Magnetic microrods as a tool for microrheology". In: *Soft Matter* 11 (13), pp. 2563–2569. DOI: 10.1039/C4SM02454K.

Byrom, Julie, Patric Han, Michael Savory, and Sibani Lisa Biswal (2014). "Directing Assembly of DNA-Coated Colloids with Magnetic Fields To Generate Rigid, Semiflexible, and Flexible Chains". In: *Langmuir* 30.30, pp. 9045–9052. DOI: 10.1021/la5009939.

Cai, Gaozhe, Li Xue, Huilin Zhang, and Jianhan Lin (2017). "A Review on Micromixers". In: *Micromachines* 8.9. DOI: 10.3390/mi8090274.

Casic, N., S. Schreiber, P. Tierno, W. Zimmermann, and T. M. Fischer (June 2010). "Friction-controlled bending solitons as folding pathway toward colloidal clusters". In: *EPL (Europhysics Letters)* 90.5, p. 58001. DOI: 10.1209/0295-5075/90/58001.

Cēbers, A and H Kalis (2011). "Dynamics of superparamagnetic filaments with finite magnetic relaxation time". In: *The European Physical Journal E* 34, pp. 1–5. DOI: 10.1140/epje/i2011-11030-y.

Cēbers, A. (2005). "Flexible magnetic filaments". In: *Current Opinion in Colloid Interface Science* 10.3, pp. 167–175. DOI: 10.1016/j.cocis.2005.07.002.

Cēbers, Andrejs (Apr. 2003). "Dynamics of a chain of magnetic particles connected with elastic linkers". In: 15.15, S1335–S1344. DOI: 10.1088/0953-8984/15/15/303.

Chen, Xueye and Lei Zhang (Oct. 2017). "A review on micromixers actuated with magnetic nanomaterials". In: *Microchimica Acta* 184, pp. 1–11. DOI: 10.1007/s00604-017-2462-2.

Cīmurs, J. and A. Cēbers (Dec. 2013). "Three-dimensional dynamics of a particle with a finite energy of magnetic anisotropy in a rotating magnetic field". In: *Physical review. E, Statistical, nonlinear, and soft matter physics* 88, p. 062315. DOI: 10.1103/PhysRevE.88.062315.

Cīmurs, Jānis, Artis Brasovs, and Kaspars Ērglis (2019). "Stability analysis of a paramagnetic spheroid in a precessing field". In: *Journal of Magnetism and Magnetic Materials* 491, p. 165630. DOI: 10.1016/j.jmmm.2019.165630.

Drescher, Knut, Raymond E. Goldstein, Nicolas Michel, Marco Polin, and Idan Tuval (Oct. 2010). "Direct Measurement of the Flow Field around Swimming Microorganisms". In: *Phys. Rev. Lett.* 105 (16), p. 168101. URL: https://link.aps.org/doi/10.1103/PhysRevLett.105.168101.

Drew, Owen, Ballard Matthew, Alexeev Alexander, and J. Hesketh Peter (2016). "Rapid microfluidic mixing via rotating magnetic microbeads". In: *Sensors and Actuators A: Physical* 251, pp. 84–91. DOI: 10.1016/j.sna.2016.09.040.

Dreyfus, Rémi, Jean Baudry, Marcus L. Roper, Marc Fermigier, Howard A. Stone, and Jérôme Bibette (2005). "Microscopic artificial swimmers". In: *Nature* 437.7060, pp. 862–865. DOI: 10.1038/nature04090.

Ērglis, K, D Zhulenkovs, A Sharipo, and A Cēbers (May 2008). "Elastic properties of DNA linked flexible magnetic filaments". In: *Journal of Physics: Condensed Matter* 20, p. 204107. DOI: 10.1088/0953-8984/20/20/204107.

Ērglis, K., R. Livanovičs, and A. Cēbers (2011). "Three dimensional dynamics of ferromagnetic swimmer". In: *Journal of Magnetism and Magnetic Materials* 323.10, pp. 1278–1282. DOI: 10.1016/j.jmmm.2010.11.021.

Ērglis, Kaspars (2010). "Experimental study of properties and motion of flexible magnetic microfilaments". In: *PhD Thesis, University of Latvia*. URL: https://mmml.lu.lv/publications.

Ērglis, Kaspars, Rūdolfs Livanovičs, and Andrejs Cēbers (Sept. 2010). "Three dimensional instability of flexible ferromagnetic filament loop". In: *Magnetohydrodynamics* 46.

Friedrich, B. M., I. H. Riedel-Kruse, J. Howard, and F. Jülicher (Apr. 2010). "High-precision tracking of sperm swimming fine structure provides strong test of resistive force theory". In: *Journal of Experimental Biology* 213.8, pp. 1226–1234. DOI: 10.1242/jeb.039800.

Frka-Petesic, B., K. Erglis, J.F. Berret, A. Cēbers, V. Dupuis, J. Fresnais, O. Sandre, and R. Perzynski (2011). "Dynamics of paramagnetic nanostructured rods under rotating field". In: *Journal of Magnetism and Magnetic Materials* 323.10, pp. 1309–1313. DOI: 10.1016/j.jmmm.2010.11.036.

Goldfarb, Ronald B. (2018). "Electromagnetic Units, the Giorgi System, and the Revised International System of Units". In: *IEEE Magnetics Letters* 9, pp. 1–5. DOI: 10.1109/LMAG.2018.2868654.

Goubault, C., P. Jop, M. Fermigier, J. Baudry, E. Bertrand, and J. Bibette (Dec. 2003). "Flexible Magnetic Filaments as Micromechanical Sensors". In: *Phys. Rev. Lett.* 91 (26), p. 260802. DOI: 10.1103/PhysRevLett.91.260802.

Goyeau, L., R. Livanovičs, and A. Cēbers (2017). "Dynamics of a flexible ferromagnetic filament in a rotating magnetic field". In: *Physical Review E* 96.6. DOI: 10.1103/physreve.96.062612.

Ido, Yasushi, Yan-Hom Li, Hiroaki Tsutsumi, Hirotaka Sumiyoshi, and Ching-Yao Chen (2016). "Magnetic microchains and microswimmers in an oscillating magnetic field". In: *Biomicrofluidics* 10.1, p. 011902. DOI: 10.1063/1.4939945.

Kang, Tae Gon, Martien A. Hulsen, Patrick D. Anderson, Jaap M. J. den Toonder, and Han E. H. Meijer (Dec. 2007). "Chaotic mixing induced by a magnetic chain in a rotating magnetic field". In: *Phys. Rev. E* 76 (6), p. 066303. DOI: 10.1103/PhysRevE.76.066303.

Kiani, Bahareh, Damien Faivre, and Stefan Klumpp (2015). "Elastic properties of magnetosome chains". In: *New Journal of Physics* 17.4, p. 043007. DOI: 10.1088/1367-2630/17/4/043007.

Kiger, Kenneth (2010). *Introduction of particle image velocimetry - UMD*. URL: https://home.cscamm.umd.edu/programs/trb10/presentations/PIV.pdf.

Koleoso, M., X. Feng, Y. Xue, Q. Li, T. Munshi, and X. Chen (2020). "Micro/Nanoscale Magnetic Robots for Biomedical Applications". In: *Materials Today Bio* 8, p. 100085. DOI: 10.1016/j.mtbio.2020.100085.

Kuei, Steve, Burke Garza, and Sibani Lisa Biswal (Oct. 2017). "From strings to coils: Rotational dynamics of DNA-linked colloidal chains". In: *Phys. Rev. Fluids* 2 (10), p. 104102. DOI: 10.1103/PhysRevFluids.2.104102.

Lauga, Eric (2020). *The Fluid Dynamics of Cell Motility*. Cambridge Texts in Applied Mathematics. Cambridge University Press. DOI: 10.1017/9781316796047.

Lauga, Eric and Thomas R Powers (2009). "The hydrodynamics of swimming microorganisms". In: *Reports on Progress in Physics* 72.9, p. 096601. DOI: 10.1088/0034-4885/72/9/096601.

Li, Yan-Hom, He-Ching Lin, and Ching-Yao Chen (2013). "Steering of Magnetic Micro-Swimmers". In: *IEEE Transactions on Magnetics* 49.7, pp. 4120–4123. DOI: 10.1109/TMAG.2013.2241028.

Liu, Fengjiao, John Zeng Hui Zhang, and Ye Mei (2016). "The origin of the cooperativity in the streptavidin-biotin system: A computational investigation through molecular dynamics simulations". In: *Scientific Reports* 6.

Nguyen, Kim Tien et al. (2021). "A Magnetically Guided Self-Rolled Microrobot for Targeted Drug Delivery, Real-Time X-Ray Imaging, and Microrobot Retrieval". In: *Advanced Healthcare Materials* 10.6, p. 2001681. DOI: 10.1002/adhm.202001681.

Olson, Sarah D., Sookkyung Lim, and Ricardo Cortez (2013). "Modeling the dynamics of an elastic rod with intrinsic curvature and twist using a regularized Stokes formulation". In: *Journal of Computational Physics* 238, pp. 169–187. DOI: 10.1016/j.jcp.2012.12.026.

Pak, On Shun, Wei Gao, Joseph Wang, and Eric Lauga (2011). "High-speed propulsion of flexible nanowire motors: Theory and experiments". In: *Soft Matter* 7 (18), pp. 8169–8181. DOI: 10.1039/C1SM05503H.

Palkar, Vaibhav, Pavel Aprelev, Arthur Salamatin, Artis Brasovs, Olga Kuksenok, and Konstantin G. Kornev (2019). "Rotating magnetic nanorods detect minute fluctuations of magnetic field". In: *Phys. Rev. E* 100 (5), p. 051101. DOI: 10.1103/PhysRevE.100.051101.

Peyer, Kathrin E., Li Zhang, and Bradley J. Nelson (2013). "Bio-inspired magnetic swimming microrobots for biomedical applications". In: *Nanoscale* 5 (4), pp. 1259–1272. DOI: 10.1039/C2NR32554C.

Pilyugina, Ekaterina, Brad Krajina, Andrew J. Spakowitz, and Jay D. Schieber (2017). "Buckling a Semiflexible Polymer Chain under Compression". In: *Polymers* 9.3, p. 99. DOI: 10.3390/polym9030099.

Powers, Thomas R. (2010). "Dynamics of filaments and membranes in a viscous fluid". In: *Rev. Mod. Phys.* 82 (2), pp. 1607–1631. DOI: 10.1103/RevModPhys.82.1607.

Purcell, E. M. (1977). "Life at low Reynolds number". In: *American Journal of Physics* 45.1, pp. 3–11. DOI: 10.1119/1.10903.

Raffel, M., Christian Willert, Steve Wereley, and Juergen Kompenhans (2007). *Particle Image Velocimetry: A Practical Guide*. DOI: 10.1007/978-3-540-72308-0.

Rikken, Roger S. M., Roeland J. M. Nolte, Jan C. Maan, Jan C. M. van Hest, Daniela A. Wilson, and Peter C. M. Christianen (2014). "Manipulation of micro- and nanostructure motion with magnetic fields". In: *Soft Matter* 10 (9), pp. 1295–1308. DOI: 10.1039/C3SM52294F.

Shanko, Eriola-Sophia, Yoeri van de Burgt, Patrick D. Anderson, and Jaap M. J. den Toonder (2019). "Microfluidic Magnetic Mixing at Low Reynolds Numbers and in Stagnant Fluids". In: *Micromachines* 10.11. DOI: 10.3390/mi10110731.

Shcherbakov, Valera P. and Michael Winklhofer (Dec. 2004). "Bending of magnetic filaments under a magnetic field". In: *Phys. Rev. E* 70 (6), p. 061803. DOI: 10.1103/PhysRevE.70.061803.

Spatafora-Salazar, Aldo, Dana M. Lobmeyer, Lucas H. P. Cunha, Kedar Joshi, and Sibani Lisa Biswal (2021). "Hierarchical assemblies of superparamagnetic colloids in time-varying magnetic fields". In: *Soft Matter* 17 (5), pp. 1120–1155. DOI: 10.1039/D0SM01878C.

Sudarsan, Arjun P. and Victor M. Ugaz (2006). "Fluid mixing in planar spiral microchannels". In: *Lab Chip* 6 (1), pp. 74–82. DOI: 10.1039/B511524H.

Sznitman, J., X. Shen, R. Sznitman, and P. E. Arratia (2010). "Propulsive force measurements and flow behavior of undulatory swimmers at low Reynolds number". In: *Physics of Fluids* 22.12, p. 121901. DOI: 10.1063/1.3529236.

Taylor, G.I. (1967). "Low Reynolds Number Flows". In: *Educational Services Incorporated. Distributor: Encyclopaedia Britannica Educational Corporation, Chicago, Illinois*.

Thielicke, William (Oct. 2014). "The flapping flight of birds: Analysis and application". PhD thesis. DOI: 10.13140/RG.2.2.18656.94728.

Thielicke, William and E J Stamhuis (Oct. 2014). "PIVlab – Towards User-friendly, Affordable and Accurate Digital Particle Image Velocimetry in MATLAB". In: *Journal of Open Research Software* 2. DOI: 10.5334/jors.bl.

Tottori, Soichiro, Li Zhang, Famin Qiu, Krzysztof K. Krawczyk, Alfredo Franco-Obregón, and Bradley J. Nelson (2012). "Magnetic Helical Micromachines: Fabrication, Controlled Swimming, and Cargo Transport". In: *Advanced Materials* 24.6, pp. 811–816. DOI: 10.1002/adma.201103818.

Vella, Dominic, Emmanuel Pontavice, Cameron Hall, and Alain Goriely (2014). "The magneto-elastica: From self-buckling to self-assembly". In: *Proceedings. Mathematical, physical, and engineering sciences / the Royal Society* 470, p. 20130609. DOI: 10.1098/rspa.2013.0609.

Vilfan, Mojca, Anton Potočnik, Blaž Kavčič, Natan Osterman, Igor Poberaj, Andrej Vilfan, and Dušan Babič (2010). "Self-assembled artificial cilia". In: *Proceedings of the National Academy of Sciences* 107.5, pp. 1844–1847. DOI: 10.1073/pnas.0906819106.

Wang, Liu, Yoonho Kim, Chuan Fei Guo, and Xuanhe Zhao (2020). "Hard-magnetic elastica". In: *Journal of the Mechanics and Physics of Solids* 142, p. 104045. DOI: 10.1016/j.jmps.2020.104045.

Wiggins, Chris H, Daniel Riveline, Albrecht Ott, and Raymond E. Goldstein (1998). "Trapping and wiggling: elastohydrodynamics of driven microfilaments." In: *Biophysical journal* 74 2 Pt 1, pp. 1043–60. DOI: 10.1016/S0006-3495(98)74029-9.

Xu, Ke, Shuang Xu, and Fanan Wei (2021). "Recent progress in magnetic applications for micro- and Nanorobots". In: *Beilstein Journal of Nanotechnology* 12, pp. 744–755. DOI: 10.3762/bjnano.12.58.

Yamakawa, Hiromi and Genzo Tanaka (1972). "Translational Diffusion Coefficients of Rodlike Polymers: Application of the Modified Oseen Tensor". In: *Journal of Chemical Physics* 57, pp. 1537–1542.

Yang, Kaiyuan, Chen Lu, Xiaodan Zhao, and Ryo Kawamura (2017). "From bead to rod: Comparison of theories by measuring translational drag coefficients of micron-sized magnetic bead-chains in Stokes flow". In: *PLoS ONE* 12. DOI: 10.1371/journal.pone.0188015.

Zaben, Abdelqader, Guntars Kitenbergs, and Andrejs Cēbers (2020a). "3D motion of flexible ferromagnetic filaments under a rotating magnetic field". In: *Soft Matter* 16 (18), pp. 4477–4483. DOI: 10.1039/D0SM00403K.

— (2020b). "Deformation of flexible ferromagnetic filaments under a rotating magnetic field". In: *Journal of Magnetism and Magnetic Materials* 499, p. 166233. DOI: 10.1016/j.jmmm.2019.166233.

Zaben, Abdelqader, Guntars Kitenbergs, and Andrejs Cēbers (Dec. 2021). "Instability caused swimming of ferromagnetic filaments in pulsed field". In: *Scientific Reports* 11, p. 23399. DOI: 10.1038/s41598-021-02541-3.

Zeng, Chuiqing, Stephen Bird, James J. Luce, and Jinfei Wang (2015). "A Natural-Rule-Based-Connection (NRBC) Method for River Network Extraction from High-Resolution Imagery". In: *Remote Sensing* 7.10, pp. 14055–14078. DOI: 10.3390/rs71014055.

Zhang, Li, Jake J. Abbott, Lixin Dong, Bradley E. Kratochvil, Dominik Bell, and Bradley J. Nelson (2009a). "Artificial bacterial flagella: Fabrication and magnetic control". In: *Applied Physics Letters* 94.6, p. 064107. DOI: 10.1063/1.3079655.

Zhang, Li, Jake J. Abbott, Lixin Dong, Kathrin Eva Peyer, Bradley Kratochvil, Haixin Zhang, Christos Bergeles, and Bradley J. Nelson (2009b). "Characterizing the swimming properties of artificial bacterial flagella". In: *Nano letters* 9 10, pp. 3663–7. DOI: 10.1021/nl901869j.

Zhao, Boan, Eric Lauga, and Lyndon Koens (Aug. 2019). "Method of regularized stokeslets: Flow analysis and improvement of convergence". In: *Phys. Rev. Fluids* 4 (8), p. 084104. DOI: 10.1103/PhysRevFluids.4.084104.

Appendix A

Deformation of flexible ferromagnetic filaments under a rotating magnetic field

Abdelqader Zaben[a], Guntars Kitenbergs[a] and Andrejs Cēbers[a,*]

[a]MMML lab, University of Latvia, Jelgavas 3, Riga, LV-1004, Latvia

ARTICLE INFO

Keywords:
magnetic filament
rotating field
flexible filament
ferromagnetic particles

ABSTRACT

Research on magnetic particles dispersed in a fluid medium, actuated by a rotating magnetic field, is becoming increasingly active for both lab-on-chip and bio-sensing applications. In this study, we experimentally investigate the behaviour of ferromagnetic filaments in a rotating field.Filaments are synthesized by linking micron-sized ferromagnetic particles with DNA strands. The experiments were conducted under different magnetic field strengths, frequencies and filament sizes, and deformation of the filaments was registered via microscope and camera. The results obtained showed that the body deformation is larger for longer filaments and higher frequencies. The angle between the filament tangent at the centre and the magnetic field direction increases linearly with frequency at the low-frequency regime. A further increase in the frequency will result in filament movement out of plane when the angle approaches 90 degrees. The experimental results were used to estimate the magnetic moment and the bending elasticity of the filament.

1. Introduction

Flexible magnetic filaments are interesting for different applications, microfluidic mixing [1] and transport [2], sensors [3], creating self-propelling magnetic microdevices and others [4]. For these applications ferromagnetic filaments are of particular interest, which may be created by linking ferromagnetic microparticles [5]. Several interesting phenomena are known for ferromagnetic filaments - in the AC magnetic field with a sufficiently high frequency they orient perpendicularly to the field [5]. When the magnetic field direction is changed, filaments form snake like 'S' shape [6]. If the direction is inverted, a ferromagnetic filament makes a loop [7], which further relaxes by 3D motion. Due to the loop formation it is possible to create self-propelling magnetic microdevices [8]. Considerable effort has been put to numerical modelling of flexible magnetic filaments. For example, the behavior of small filaments under constant field has been investigated in the dilute regime [9] and under external flow [10]. Dynamics of a filament in rotating field have been studied in [11]. In the present work we investigate the physical properties of ferromagnetic filaments under a rotating magnetic field, focusing on the deformation dependence on the frequency and strength of the field.

2. Experimental

2.1. Synthesis

The filament synthesis methodology was adapted from [12]. In this way filaments with a length L between 8 μm to 80 μm are formed. For example, see Fig.1(a). The filaments were prepared by mixing 4.26 μm large ferromagnetic particles (Spherotech, 1%w/v) with DNA strands (ASLA biotech, 182 μg/ml) in TE buffer (10%) solution. Ferromagnetic particles are made from polymer beads that are covered with chromium dioxide. Their surface is functionalized with streptavidin. DNA strands are 1000bp long and have biotin at their ends.

Each sample was made by mixing 0.5 ml TE buffer solution ($\eta = 0.01$ P, pH = 7.5) with 10 μL of DNA solution and 2 μL particle suspension. This corresponds to a resulting DNA concentration of 6 nM and particle mass concentration of 0.004% w/v. The sample is then quickly placed in the middle of two $5 \times 5 \times 1$ cm Neodymium magnets, fixed 7 cm apart, providing a homogeneous field of $\approx$ 500 Oe. It is left in the field for two minutes, allowing the particles to form chains. While chains are being formed, the biotin ends of the DNA find their way to the streptavidin surface of beads and link the particle chains permanently.On average, each particle has $\approx 8 \cdot 10^6$ linkers, which is slightly less than their maximum capacity in [12].

2.2. Video microscopy

Filaments were observed with an optical microscope (Leica DMI3000B) using a 40× objective in bright field mode. The magnetic field is generated using a coil system that consists of six coils placed to provide fields in three directions. An AC power supply (Kepco BOP 20-10M) connects with the coil pairs in each direction, which is capable of producing fields of up to 120 Oe, with a maximum frequency of 50 Hz. The current output is controlled using National Instruments data acquisition card and LabVIEW code. It generates analogue sine and cosine signals for a rotating magnetic field. The fluidic cells are prepared using two glass slides separated by 130 μm double-sided adhesive tape. Each cell is formed by a 1×1 cm cut in the tape, in which 10 μl of the prepared solution are added. The images are taken using Basler ac1920-155um camera. Depending on the measurement, it is used either in a fixed frame rate, for which a maximum of 200 fps can be achieved, or by a trigger mode, which allows to synchronize it with the magnetic field direction.

*Corresponding author
andrejs.cebers@lu.lv (A. Cēbers)
ORCID(s):

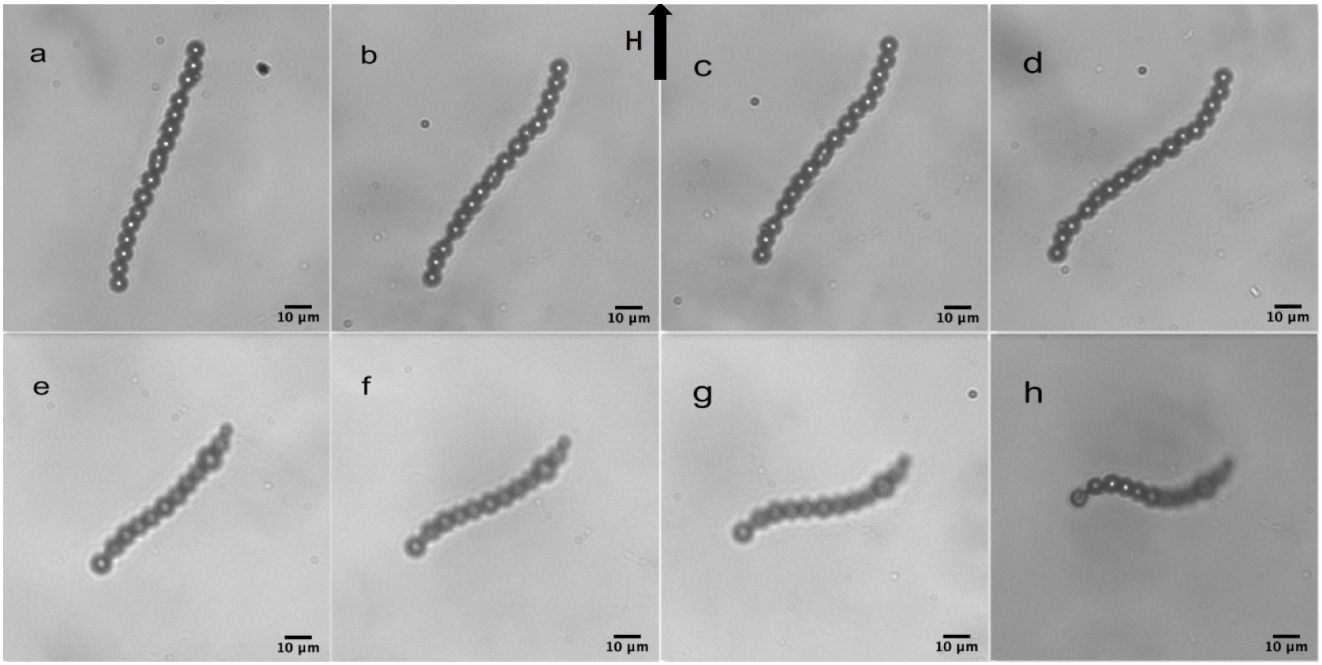

Figure 1: Behavior of two flexible magnetic filaments under rotating magnetic field $H = 8.6$ Oe. Filament with $L = 67.4$ μm at (a) 0.2 Hz, (b) 0.3 Hz, (c) 0.4 Hz and (d) 0.6 Hz. Filament with $L = 50.5$ μm at (e) 1.0 Hz, (f) 1.5 Hz, (g) 2.0 Hz and (h) 3.0 Hz. In (h), the filament moves out of imaging plane.

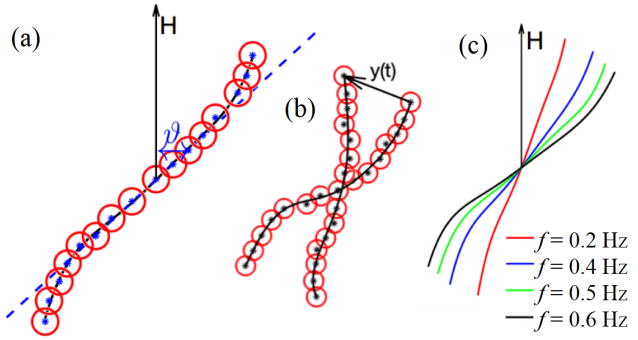

Figure 2: (a) An illustration of filament image processing. Polynomial fit (black curve) of centres of particles (blue asterisks and red circles) describes the deformed filament. The angle (ϑ) between the tangent at the filament center (blue dashed line) and the magnetic field direction (indicated with the black arrow) is used for characterizing deformation. (b) An example of deformation relaxation measurement. The position of filament tip particle (y-discplacement) is tracked over time. (c) Experimental magnetic filament deformations for different frequencies f (0.2, 0.4, 0.5 and 0.6 Hz) at $H = 8.6$ Oe.

2.3. Image processing

The images used for characterising the filament deformation were obtained by trigger mode in such a way that the magnetic field points to the north, as shown in Fig.1. Deformation of the filament may be characterized by the measurement of the tangent angle ϑ at the centre (shown in Fig.2(a)) and at the tip, which are compared with the results of the numerical simulations. The tangent angle at the tip was found to be not along the field; however close to it (data not shown).

Image processing was done with Matlab and the steps are depicted in Fig.2(a). Initially, the particle centres (blue asterisks) are detected using a circular object detection function (red circles). Then the shape of the filament is approximated by fitting the particle centre coordinated with a polynomial of sixth order (black curve). This allows us to find the tangent at the centre (blue dashed line) and calculate the angle ϑ.

Experiments for analysing the deformation relaxation time were obtained by setting the frame rate to 150 fps. Initial deformation of the filament is made by a rotating magnetic field having strength values between 8.6 Oe and 17.2 Oe. Then the magnetic field is turned off and the relaxation is observed, while tracking the displacement of the filament tip particle. An example of processed image for tracking the displacement of tip particle $y(t)$ is shown in Fig.2(b).

3. Results and Discussion

The experiments were conducted in the following manner. The fluidic cell is placed for observation under the microscope. Due to gravity effects, the filaments sediment to the bottom of the fluidic cell. A static magnetic field of 17.2 Oe is applied in the vertical direction for the initial alignment of the filament. A further static field is switched off, and a rotating field is applied in the clockwise direction. the field strength is between 6 Oe and 25 Oe, and a frequency up to 8 Hz. The image acquisition is set to trigger mode. Examples of steady-state configurations of two filaments in the rotating field are shown in Fig.1. Characteristic S-like shape may be seen, which is also observed for chains of paramagnetic particles, see for example [13].

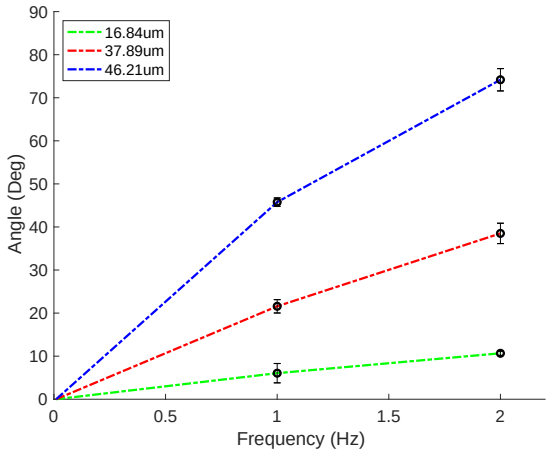

Figure 3: Relationship between the angle ϑ and frequency under rotating magnetic field, $H = 6.9$ Oe, for filaments with different lengths: $L = 46.2$ μm (blue line), $L = 37.9$ μm (red line) and $L = 16.8$ μm (green line).

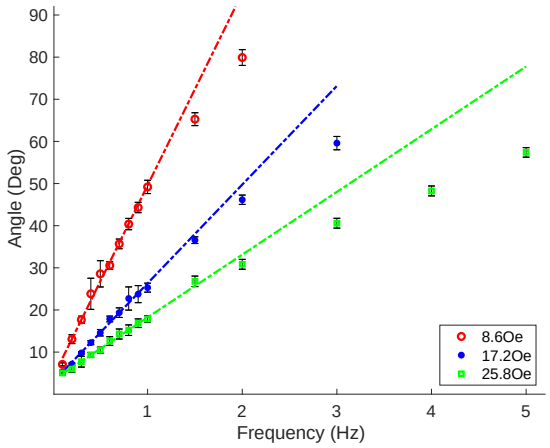

Figure 4: Relationship between the angle ϑ and frequency, under rotating magnetic field with different strengths, $H = 8.6$ Oe (red line), $H = 17.2$ Oe (blue line) and $H = 25.8$ Oe (green line), filament length $L = 46.3$ μm.

Increase of frequency induces a larger deformation of the filament. This can be clearly seen in Fig.2(c), where the filament polynomial fits for various frequencies (0.2 Hz (red curve), 0.4 Hz (blue curve), 0.5 Hz (green curve) and 0.6 Hz (black curve)) at fixed magnetic field strength $H = 8.6$ Oe are compared.

Measurements were done for filaments with different lengths. The results show that longer filaments have higher angle ϑ at a fixed frequency and field strength. Hence, longer filaments tend to deform more, while having more flexibility to deform by viscous torques under a rotating field. Angle as a function of the frequency for different filament lengths is shown in Fig.3.

The results for the effect of varying magnetic field strength H and frequency f was obtained using a single filament for each analysis. The rotating magnetic field introduces a magnetic torque, which is a function of the field strength opposed by viscous torque, dependent on the length L and the angular velocity $2\pi f$. The increase of the frequency at a constant H increases the characteristic angle ϑ. Results are shown in Fig.4. At low frequencies this relationship is found to be linear. A further increase in the frequency tends to lower the gradient as a result of the increased viscous forces. The filament tends to deform having 'S' like shape as visible in Fig.1(g), where the filament centre tends to orient perpendicular to the magnetic field direction.

The effect of increasing the field strength H at constant frequency decreases the deformation and angle ϑ, due to the increased torque to overcome the friction forces.

In these experiments filaments were found to move synchronously with the magnetic field (data not shown). This is different than observed in numerical modelling by Goyeau et al. [11]. There, if frequency is increased, the filaments reach an asynchronous regime, where the filaments experience back and forth motion due to lag in following the magnetic field. By comparison, in experiments a further increase in ϑ results in filament movement out of the image plane, in the third dimension. This transition was noted to occur when the filament centre orients perpendicularly with the field direction, having ϑ of 90°. An example of this behavior visible in figure Fig.1(h). As a result, we can assume that small fluctuations deform the filament to a three dimensional shape, which is dynamically preferable, before it reaches an asynchronous regime.

Similar deformed 'S' like filament shapes with back and forth motion can be observed for paramagnetic filaments in specific rotating magnetic field conditions [14]. However, the difference in magnetic properties does not allow to compare the behavior quantitatively.

For our experiments we can describe the angle ϑ dependence by a theoretical model for filament dynamics under rotating field presented in Ērglis et al. [7], where numerical simulations give the following relation

$$\vartheta = 0.086\frac{\omega\tau}{Cm}, \tag{1}$$

where τ is the elastic deformation time $\tau = \frac{\zeta L^4}{A_b}$, ω is the angular velocity $\omega = 2\pi f$ and Cm is the magnetoelastic number, $Cm = \frac{MHL^2}{A_b}$ for which L is the filament length, H is the magnetic field strength, A_b is the bending modulus and ζ is the hydrodynamic drag coefficient which is estimated by $4\pi\eta$.

We use relation (1) to analyze the linear regimes in Fig.4. Slopes $\frac{d\vartheta}{df}$ as a function of $\frac{1}{H}$ for a filament $L = 46.3$ μm are shown in Fig.5. The experimental data is fitted with a linear relation $\frac{\vartheta}{f} = a\frac{1}{H}$, for which we find $a = 6.8$ Oe·s. From this we find information about filament magnetization. For magnetization per unit length we get $M = 2.14 \cdot 10^{-7}$emu and for the magnetic moment of particle $m = 9.01 \cdot 10^{-11}$emu (M·d). The last value is not far from estimates in [7].

In order to measure the bending modulus, the protocol for filament relaxation was carried out, as explained in §2.3.

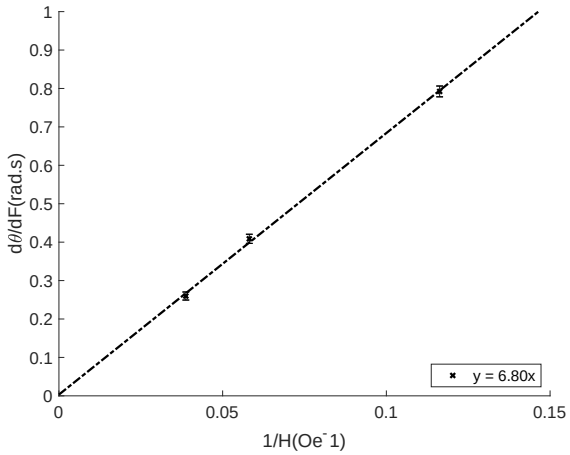

Figure 5: Relationship between $\frac{d\vartheta}{df}$ and $\frac{1}{H}$, obtained for a filament with length $L = 46.3$ μm.

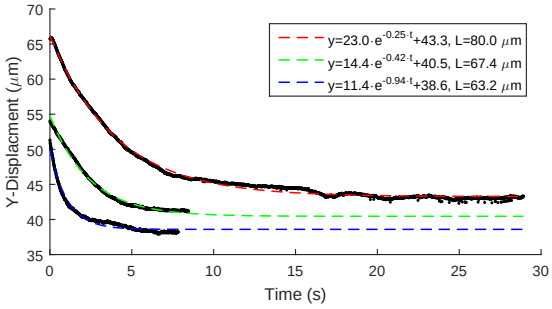

Figure 6: Filament relaxation behaviour for different filament length and initial rotating field conditions: $L = 80.0$ μm, $f = 1.0$ Hz and $H = 8.6$ Oe (red curve). $L = 63.2$ μm, $f = 1.0$ Hz and $H = 13.7$ Oe (blue curve). $L = 67.4$ μm, $f = 1.5$ Hz and $H = 8.6$ Oe (green curve).

The motion of the filament tip shows an exponential time dependence, as can be seen in Fig.6. The decrements of relaxation are different for different filament length and are found to be equal to 0.25 s^{-1} for $L = 80.0$ μm, 0.42 s^{-1} for $L = 67.4$ μm and 0.94 s^{-1} for $L = 63.2$ μm. It is worth to note that in our experiments the filament does not return to its original shape, as visible in Fig.2(b). Small remaining deformation may be the result of damaged bonds between the particles or due to wall surface drag.

The filament relaxes due to the action of bending elasticity and is slowed down by viscous forces. The solution of the elasticity problem for the rod at free and unclamped boundary conditions [15] gives the spectrum of relaxation rates from which the smallest decrement is given by relation $3.93^4 L^{-4} A_b/\zeta$. Taking experimental values of decrements and fitting as a function of L^{-4} allows to estimate the average bending modulus of the rod. This is done in Fig.7. The fitted line and its error gives $(A_b \pm \Delta A_b) = (6.5 \pm 3.4) \cdot 10^{-13}$ erg·cm. This is close to the estimate of the bending modulus obtained in [5]. The value obtained by relaxation experiments is by almost two orders of magnitude larger than the

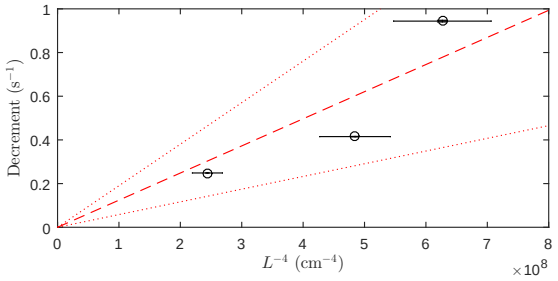

Figure 7: Relationship between relaxation decrements and L^{-4} for different filament lengths. Black circles are experimental points with errorbars. Red dashed line is linear fit and red dotted lines are confidence intervals for 3σ.

calculated by the relation for the dipolar interaction contribution to the bending modulus $A_b = M^2/2$ given in [4, 16] (For more exact nevertheless close coefficient before M^2, see [17]). Thus we may conclude that bending elasticity is determined by the linkers. In [18], the bending modulus of chains of paramagnetic particles was measured by the study of thermal fluctuations of their shape. obtained results show that these chains, possibly due to the much smaller size of the particles, are significantly more flexible.

4. Conclusions

Properties of ferromagnetic filaments synthesized by linking funtionalized ferromagnetic microparticles by biotinized DNA fragments are measured by the study of their deformation in a rotating magnetic field. It is found that filaments at low frequencies have 'S' like shapes and the tangent angle at the center of filament is proportional to the frequency and inverse value of the field strength. The fit of experimentally obtained dependence by the relation obtained numerically gives the magnetic moment of the ferromagnetic particles. Very interesting observation was made at higher frequencies of the rotating field showing that the filament is going out of the plane of rotating field. Detailed study of this important phenomenon is pending for future publications. The bending modulus of the filament is measured by registering its relaxation to straight configuration from initially prepared deformed shape. The results obtained show that synthesized ferromagnetic filaments are quite stiff and their persistence length has the order of magnitude of several tenths of centimeters.

Acknowledgements

A.Z. acknowledges support from the European Union's Horizon 2020 research and innovation programme under grant agreement MAMI No. 766007, A.C. from M.era-net project FMF No.1.1.1.5./ERANET/18/04 and G.K. from PostDocLatvia grant No. 1.1.1.2/VIAA/1/16/197.

References

[1] S. L. Biswal, A. P. Gast, Micromixing with linked chains of paramagnetic particles, Analytical Chemistry 76 (2004) 6448–6455.

[2] S. Hanasoge, P. J. Hesketh, A. Alexeev, Metachronal motion of artificial magnetic cilia, Soft Matter 14 (2018) 3689–3693.

[3] C. P. Moerland, L. J. van IJzendoorn, M. W. J. Prins, Rotating magnetic particles for lab-on-chip applications - a comprehensive review, Lab Chip 19 (2019) 919–933.

[4] A. Cēbers, K. Ērglis, Flexible magnetic filaments and their applications, Advanced Functional Materials 26 (2016) 3783–3795.

[5] K. Ērglis, M. Belovs, A. Cēbers, Flexible ferromagnetic filaments and the interface with biology, Journal of Magnetism and Magnetic Materials 321 (2009) 650 – 654.

[6] J. Townsend, R. Burtovyy, Y. Galabura, I. Luzinov, Flexible chains of ferromagnetic nanoparticles, ACS Nano 8 (2014) 6970–6978.

[7] K. Ērglis, R. Livanovičs, A. Cēbers, Three dimensional instability of flexible ferromagnetic filament loop, Magnetohydrodynamics 46 (2010) 245–256.

[8] M. Belovs, A. Cēbers, Ferromagnetic microswimmer, Phys. Rev. E 79 (2009) 051503. See also Erratum.

[9] J. J. Cerdà, P. A. Sánchez, D. Lüsebrink, Flexible magnetic filaments under the influence of external magnetic fields in the limit of infinite dilution, Phys. Chem. Chem. Phys. 18 (2016) 12616–12625.

[10] D. Lüsebrink, J. J. Cerdà, P. A. Sánchez, S. S. Kantorovich, T. Sintes, The behavior of a magnetic filament in flow under the influence of an external magnetic field, The Journal of Chemical Physics 145 (2016) 234902.

[11] L. Goyeau, R. Livanovičs, A. Cēbers, Dynamics of a flexible ferromagnetic filament in a rotating magnetic field, Phys. Rev. E 96 (2017) 062612.

[12] K. Ērglis, Experimental study of properties and motion of flexible magnetic microfilaments, PhD Thesis, University of Latvia (2010).

[13] S. L. Biswal, A. P. Gast, Rotational dynamics of semiflexible paramagnetic particle chains, Phys. Rev. E 69 (2004) 041406.

[14] S. Kuei, B. Garza, S. L. Biswal, From strings to coils: Rotational dynamics of DNA-linked colloidal chains, Phys. Rev. Fluids 2 (2017) 104102.

[15] C. H. Wiggins, D. Riveline, A. Ott, R. E. Goldstein, Trapping and wiggling: Elastohydrodynamics of driven microfilaments, Biophysical Journal 74 (1998) 1043 – 1060.

[16] B. Kiani, D. Faivre, S. Klumpp, Elastic properties of magnetosome chains, New Journal of Physics 17 (2015) 043007.

[17] D. Vella, E. D. Pontavice, C. L. Hall, A. Goriely, The magnetoelastica : from self-buckling to self-assembly, Proceedings of the Royal Society A: Mathematical, Physical and Engineering Sciences 470 (2014) 20130609.

[18] J. Byrom, P. Han, M. Savory, S. L. Biswal, Directing assembly of dna-coated colloids with magnetic fields to generate rigid, semiflexible, and flexible chains, Langmuir 30 (2014) 9045–9052. PMID: 25052952.

Soft Matter

ARTICLE TYPE

Cite this: DOI: 00.0000/xxxxxxxxxx

3D motion of flexible ferromagnetic filaments under rotating magnetic field †

Abdelqader Zaben,[a] Guntars Kitenbergs[a] and Andrejs Cēbers*[a]

Received Date
Accepted Date

DOI: 00.0000/xxxxxxxxxx

Ferromagnetic filaments in a rotating magnetic field are studied both numerically and experimentally. The filaments are made from micron-sized ferromagnetic particles linked with DNA strands. It is found that at low frequencies of the rotating field a filament rotates synchronously with the field and beyond a critical frequency it undergoes a transition to a three dimensional regime. In this regime the tips of the filament rotate synchronously with the field on circular trajectories in the plane parallel to the plane of the rotating field. The characteristics of this motion found numerically match the experimental data and allow us to obtain the physical properties of such filaments. We also discuss the differences in behaviour between magnetic rods and filaments and the applicability of filaments in mixing.

1 Introduction

Magnetic filaments are the subject of growing interest due to their applications, for example, as mixers for microfluidics [1] or in creating self-propelling microdevices capable of carrying cargo for targeted transport [2]. Different methods of driving magnetic particle systems were recently reviewed by Driscoll and Delmotte [3]. Magnetic rods under the action of a rotating field are of special interest for use in microrheological measurements by magnetic rotational spectroscopy [4,5]. The behavior of ferromagnetic rods under the action of a rotating magnetic field is interesting. It is known that for frequencies larger than the critical, a rigid ferromagnetic rod has two different regimes - one is an infinite in-plane rotation with a periodic angular velocity, and the other is a precessional motion around an axis inclined with respect to the plane of the rotating field. This situation is structurally unstable and at some small perturbation, for example, due to the Earth's magnetic field, only the precessional regime survives. For a rigid ferromagnetic rod this was recently illustrated experimentally [6]. Previously we have numerically studied the planar regime of a flexible ferromagnetic rod under the action of a rotating magnetic field [7]. It was shown that a filament has synchronous or asynchronous regimes of rotation depending on the frequency of the rotating field.

In the present paper the stability of the asynchronous planar regime of the flexible ferromagnetic rod is studied both experimentally and numerically. Using ferromagnetic filaments whose physical properties were measured previously [8], we found that the planar asynchronous regime is unstable at frequencies above the critical and the precessional regime is established. In this regime the tips of the filament move in the antiphase along circular trajectories in the planes parallel to the plane of rotating field. We discuss the differences between ferromagnetic and paramagnetic filament motion, as well their applicability to mixing.

2 Experimental

The filament synthesis was done as presented in details by Ērglis [9]. The filaments are made by linking 4.26 μm ferromagnetic particles (Spherotech, 1%w/v) with 1000 bp long biotinized DNA strands (ASLA biotech,192 μg/ml). The chromium oxide coated polystyrene particles are functionalized with streptavidin; which bonds with the biotin in the DNA ends and forms filaments. The samples are made by mixing 0.5 ml of 10% TE buffer solution ($\eta = 0.01$ P, pH = 7.5) with 10 μl of DNA giving a resulting concentration of 6.2 nM. 2 μl of particle solution is then added (0.004% w/v), and the sample is placed between two Neodymium magnets ($\approx$ 500 Oe) for two minutes to allow particle alignment. Chains are formed with length L ranging from 8 μm to 80 μm.

20 μl of the sample is placed in a fluidic cell for observation. The cell is made by spacing two glass sides with 211 μm thick adhesive tape. The fluidic cell is then placed under an optical microscope (Leica DMI3000B) using a 40x objective, bright field configuration. The magnetic field is generated using a coil system powered by Kepco BOP 20-10M power supplies, providing a field strength up to 120 Oe, with a maximum frequency of 50 Hz. The field profile is generated by a LabVIEW code through National Instruments data acquisition card (NI PCI-6229), which is connected to the power supplies. The images are acquired using Basler ac1920-155um camera with a fixed frame rate setting (up to 100 fps).

[a] MMML lab, University of Latvia, Jelgavas 3, Riga, LV-1004, Latvia; E-mail: andrejs.cebers@lu.lv

† Electronic Supplementary Information (ESI) available: Supplementary Videos and their description. See DOI: 10.1039/cXsm00000x/

Following the above procedure, the filaments were found to be randomly distributed with various lengths across the cell. A rotating field profile with a frequency $f = 1$ Hz and a field strength $H = 17.2$ Oe is first applied for 15 minutes to allow free particles to connect to the filaments. Due to the density difference, the filaments tend to sediment at the bottom of the cell. The filaments were found to have a slight movement during rotation, probably because of the particle to wall interaction.

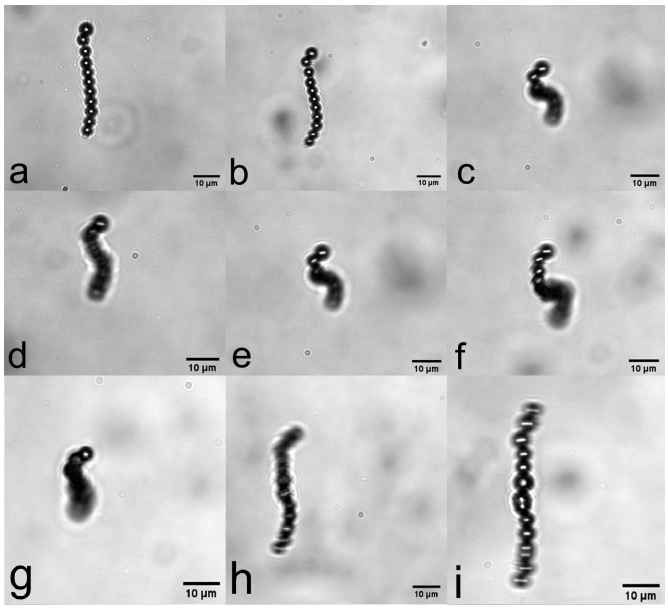

Fig. 1 Shapes of deformed filaments under rotating magnetic field. Filament with $L = 41$ μm at $H = 17.2$ Oe for frequencies (a) $f = 1$ Hz, (b) $f = 4$ Hz, (c) $f = 9$ Hz. Filaments at $H = 17.2$ Oe and $f = 8$ Hz for filaments with lengths (d) $L = 33$ μm, (e) $L = 41$ μm, (f) $L = 65$ μm. Filament with $L = 46$ μm at $f = 5$ Hz and magnetic fields (g) $H = 4.3$ Oe, (h) $H = 12.9$ Oe, (i) $H = 25.8$ Oe.

The experiments were done by applying a rotating field to samples of filaments with different lengths L, at multiple field strengths H and frequencies f. Some examples of deformed filament shapes under a rotating field in $x-y$ plane are shown in Fig. 1. The effect of increasing the frequency f can be seen in Fig. 1(a)-(c), where length L and field strength H are constant. At low frequencies, the filament rotates synchronously with the magnetic field having an orientation lag, which results in small deformations as visible in Fig. 1(a) and (b) and supplementary Video S1. We define the critical frequency (f_c) as the smallest frequency at which the steady state of the deformed filament has moved out of the plane of the rotating field. Experimentally, this can be seen as blurry parts of the filament, which have moved out of the focus plane. At higher frequencies ($f > f_c$), the filament tip motion was found to have a circular path (data not shown). An example of a deformed filament shape can be seen in Fig. 1(c) and supplementary Video S2. Fig.1(d) - (f) show the 3D shape for filaments of different lengths L, operating at a constant frequency ($f > f_c$) and field strength H. The effect of increasing the field strength H is shown in Fig. 1(g) - (i), for which the filament length L and frequency f are constant.

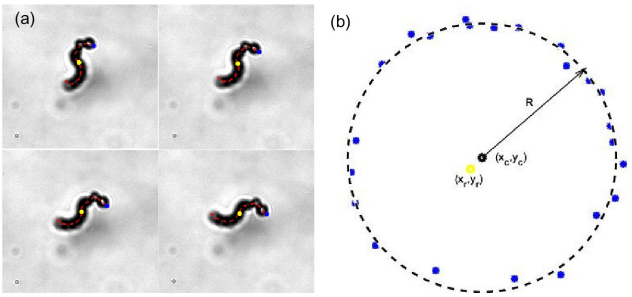

Fig. 2 An illustration of how radius R is for each filament. (a) Four consecutive images of a filament, which is rotating in 3D. Red lines indicate the centre line. The blue points shows the tracked, while yellow points represent the tracked centre, which is used for reference. (b) The tracked tip coordinates (blue points) are fitted with a circle (dashed line). Yellow point ((x_r,y_r)) is the reference and black point ((x_c,y_c)) denotes the fitted centre.

Image processing was done using Matlab. First, the images were segmented based on filament intensity. Second, the centre line of the filament was obtained using (NRBC) package[10]. To characterize the filament deformation we introduce the radius R. An illustration of radius R determination can be seen in Fig. 2. Then the coordinates of one of the filament tips (x_t,y_t) and centre (x_i,y_i) obtained from the detected centre line are recorded for each frame, shown as the blue and yellow points in Fig. 2(a) respectively. As the filaments are slightly moving during experiments, we use the filament centre coordinates (x_r,y_r), yellow point shown in Fig. 2(b), in the first image as a reference point. Then the difference between the centre coordinates (x_i,y_i) and (x_r,y_r) is calculated to obtain the new tip coordinates after translation. The tip coordinates, shown as scattered blue points in Fig. 2(b), are fitted with a circle equation. This gives the radius R and the centre of rotation (x_c,y_c) (black point). The differences between the blue points and the fitted circle allows us to define an experimental error as σ. It is important to also mention that the rotation of the filament is not symmetric with respect to the centre of the filament. To account for this, the length L is taken as $2 \cdot R_0$, where R_0 is the radius of an undeformed filament, which rotates at a low frequency. This is the reason why only one tip of each filament is tracked.

Following the image processing procedure mentioned above, we find the radius R at each frequency f and magnetic field H. In order to make results comparable, we scale radius R with length L. This means that for an undeformed filament $R/L = 0.5$. Fig. 3 shows the R/L dependence on frequency f for three filaments with different length L at the same magnetic field $H = 17.2$ Oe. For frequencies below critical f_c, the results show that the filaments have minor deformations reaching R/L $\sim$ 0.45. This is followed by a rapid drop of R/L for frequencies above critical. A further increase in the frequency was found to have smaller influence on R/L drop. It is clearly visible that a longer filament has a lower critical frequency than shorter filaments, if the field is kept constant.

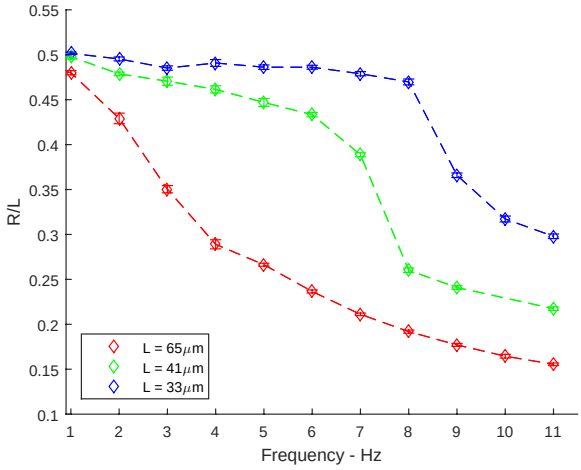

Fig. 3 Experimental data for the relationship between R/L and frequency; filaments with different length and operating at field strength H =17.2 Oe.

3 Model and numerical results

The ferromagnetic filament is described by a modified Kirchhoff model in which the action of magnetic torques is taken into account[11,12]. The force $\vec{F}$ in the cross section reads

$$\vec{F} = -A_b \frac{\partial^3 \vec{r}}{\partial l^3} + \Lambda \frac{\partial \vec{r}}{\partial l} - M\vec{H} \qquad (1)$$

where l is the natural parameter of the centerline, A_b is the bending modulus of the rod, the linear density of the magnetization M is along the local tangent direction and the Lagrange multiplier Λ enforces the inextensibility of the filament. The dynamics of the filament are described by the partial differential equation

$$\zeta \frac{\partial \vec{r}}{\partial t} = -A_b \frac{\partial^4 \vec{r}}{\partial l^4} + \frac{\partial}{\partial l}\left(\Lambda \frac{\partial \vec{r}}{\partial l}\right) \qquad (2)$$

and the term with the magnetic field enters only through the boundary conditions. These in the present case are taken as for the rod with free and unclamped ends: $\vec{F}|_{0,L} = 0$; $\partial^2 \vec{r}/\partial l^2|_{0,L} = 0$ (L is the length of the rod). The Eq.2 is solved for each time step by an implicit scheme and the inextensibility is accounted for by the projection operator $P = I - J^T (J\zeta^{-1} J^t)^{-1} J$, where $J = \partial g_i / \partial \vec{r}_k$ is the $p \times 3(p+1)$ matrix for the rod with $p+1$ marker points and p constraints $g_i = (\vec{r}_{i+1} - \vec{r}_i)^2 = h^2$.

We introduce the length L as the characteristic length scale and the elastic relaxation time $\tau_e = \zeta L^4 / A_b$ as the time scale, where $\zeta = 4\pi\eta$ and η is the viscosity of the medium. As a result the dynamics of the filament are determined by two dimensionless parameters - the magnetoelastic number $Cm = MHL^2/A_b$ and $\omega\tau_e$.

Previously, this algorithm was used to simulate the buckling of a ferromagnetic rod at field inversion[11], anomalous orientation in an AC field of high frequency[12], self-propulsion[13] and other phenomena. The behavior of the ferromagnetic rod in a rotating field was also considered[7]. Here we give evidence that the planar asynchronous regime is unstable and the filament relaxes to a three-dimensional precessional regime around the vector of the angular velocity of the rotating field.

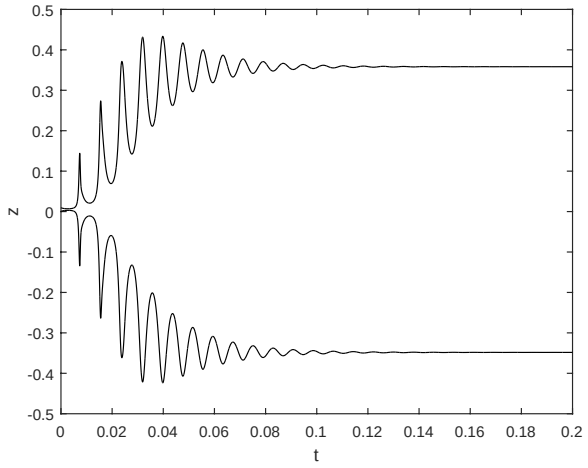

Fig. 4 Time dependence of filament tips' z coordinates show formation of a precessional regime. $Cm = 50$, $\omega\tau_e = 1000$.

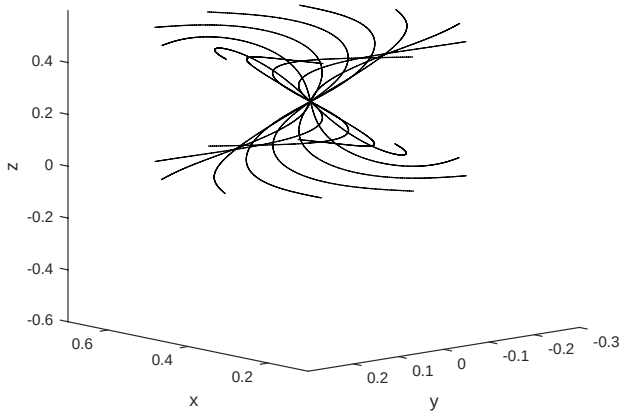

Fig. 5 Configurations of the filament in precessional regime. $Cm = 220$, $\omega\tau_e = 4500$.

The algorithm is run from initial conditions until a dynamic equilibrium is reached. In Fig. 4 the instability of the planar regime is illustrated by the time dependence of the z coordinates of the filament tips at $Cm = 50$ and $\omega\tau_e = 1000$. This is caused by a tiny deviation from the rotational plane - at $t = 0$ the initial coordinate of one tip is set to $z = 0.004$. When the precessional regime is established, the tips move in anti-phase along circular trajectories. Let us note that in this regime the motion of the filament is synchronous with the rotating field. The numerically calculated filament configurations in the precessional regime for $Cm = 220$ and $\omega\tau_e = 4500$ are shown in Fig. 5. Video examples of planar and 3D regimes can be seen in supplementary Videos S3 and S4.

The transition to the precessional regime occurs when the frequency is above the critical for the synchronous regime. Its nu-

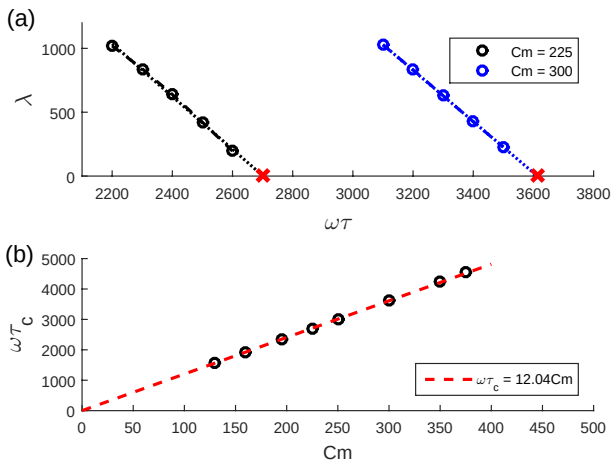

Fig. 6 Critical frequency $(\omega\tau_e)_c$ is proportional to the magnetoelastic number Cm. (a) An example of finding critical frequencies by decrement (λ) analysis for $Cm = 225$ and $Cm = 300$. Circles represent numerical data, lines - linear fits and red $\times$ correspond to critical frequencies $(\omega\tau_e)_c$. (b) Critical frequency as a function of Cm. Circles are numerical data and the dashed line is the linear fit.

merical value may be found by the study of the relaxation of the filament tip to the plane of the rotating field which for small perturbations occurs according to the law $z = z(0)\exp(-\lambda t)$. For each Cm we find the decrements λ as a function of frequency $\omega\tau_e$, as is shown in Fig. 6(a). By extrapolating data to $\lambda = 0$, we find critical frequencies $\omega\tau_{ec}$ for multiple magnetoelastic numbers Cm. These values are shown in Fig. 6(b). The data are well described by a linear dependence, which is $\omega\tau_{ec} = 12.04Cm$. The value of the slope is very close to 12, which was predicted for a ferromagnetic rod[7].

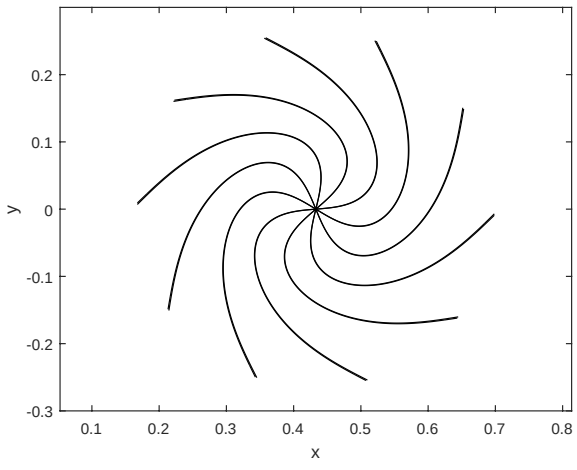

Fig. 7 Configurations of the filament in precessional regime in the projection on the plane of rotating field ($Cm = 220$ $\omega\tau_e = 4500$).

It should be remarked that the configurations of the filament in the precessional regime are quite strongly bent as may be seen from the experimental data Fig. 1. This is in qualitative agreement with the numerical simulation data, as shown in Fig. 7., where the filament configurations for $Cm = 220$ and $\omega\tau_e = 4500$ are shown in the projection on x, y plane.

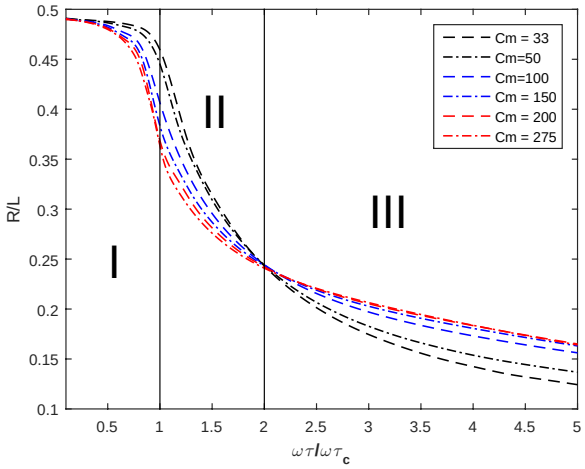

Fig. 8 Numerical simulation results for filament deformations. Normalized deformation R/L as a function of normalized frequency $\omega\tau/\omega\tau_c$.

The linear dependence of the critical frequency allows us to qualitatively analyze the numerical results and divide the filament behaviour into three regimes. Also, for numerical simulations we can define a deformation measure as the radius R. Here it can be simply taken as the half distance between the filament tips in the $x-y$ plane. The corresponding relationship of R/L as a function of frequency $\omega\tau$, normalised by $\omega\tau_c$, is shown in Fig. 8. Region I: In-plane rotation with filament deformation depending on Cm. At critical frequency $\omega\tau_c$ filament at lower Cm deforms less. The critical frequency corresponds to $\omega\tau/\omega\tau_c = 1$. Region II: 3D rotations with a rapid drop in R/L. Region III: A further increase in $\omega\tau/\omega\tau_c$ has a lower rate of R/L drop. It should be noted that operating at higher Cm ($Cm > 200$) has no influence on R/L at region III.

4 Comparison of experimental and numerical results

Previously experimental and numerical results were presented separately. In this section we compare them both qualitatively and quantitatively.

Using R/L allows us to directly compare the filament deformations. Data in Fig. 3 and Fig. 8 show a very similar behavior for the deformation dependence on frequency. There is an initial phase with little deformations, followed by a sharp drop and finishing with a much slower decrease. To perform a quantitative comparison, we made an experiment with the same filament ($L = \text{const}$) for five different magnetic fields H and multiple rotating field frequencies f for each of them. The experimental data are visible in Fig. 9 as diamonds with different colours.

To fit the numerical data to the experimental results, we introduce two parameters A and B. The magnetic field H is linked to the magnetoelastic number Cm by $A = Cm/H$. The frequency f is linked to the dimensionless frequency $\omega\tau_e$ by $B = \omega\tau_e/f$.

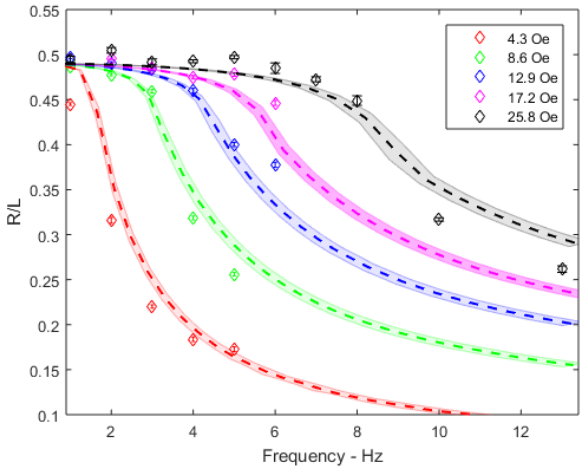

Fig. 9 Filament deformation comparison between experiment and numerical results via R/L dependence on frequency. The colored diamonds denote experimental data for filament with $L = 46$ μm operating at different field strength H. The dashed lines represents numerical simulations scaled with values of parameters obtained from the fit for different Cm values as shown in Table.1. The shaded area represents the error margins obtained from fitting.

H, Oe	Cm
4.3	31
8.6	62.5
12.9	93.8
17.2	125
25.8	187.5

Table 1 Experimental field strength H and corresponding magnetoelastic numbers Cm, as found by non-linear fit.

A and B are found with Matlab by a nonlinear least squares fit of all experimental data simultaneously. For that we take a 2D interpolation (scatteredInterpolant) of many numerical curves $R/L = func(\omega\tau_e, Cm)$ and build a custom function. Experimental errors are used as weights. Taking care of local minima, this results in $(A \pm \Delta A) = (125 \pm 2.2)$ Oe^{-1} and $(B \pm \Delta B) = (241.6 \pm 4.4)$ s. The fit allows us to relate values for each field strength H with a magnetoelastic number Cm, which are shown in Table 1.

With numerical results and parameters A and B it is possible to construct the best fits. These are shown in Fig. 9 as dashed lines of the same colour as the corresponding magnetic field. For a more obvious comparison we have added the possible fit errors with corresponding colour shades. They are constructed from the maximal positive and negative deviations, according to the errors. A reasonably good agreement is visible in the figure. For some points the fitted values have been slightly overestimated, while for others - underestimated.

It is important to verify the feasibility of the fit parameters. As $\omega = 2\pi f$, we can find the elastic relaxation time $\tau_e = B/2\pi = 38.5$ s. Using the parameter definitions and the same approach as previously[8], we can find the physical properties of the filament, namely, magnetization per unit length $M = 4.9 \cdot 10^{-7}$ emu and bending modulus $A_b = 1.5 \cdot 10^{-12}$ erg·cm. These values are close to the estimates we have found earlier[8], confirming the quality of the fit.

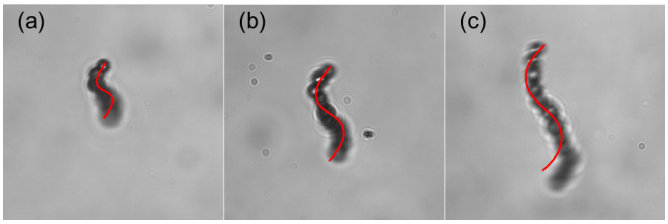

Fig. 10 Direct comparison of filaments in experimental images and numerical simulations, using best fit, shows a qualitative agreement. Filament of $L = 46$ μm at $f = 5Hz$ and different H is compared to numerical results at $\omega\tau = 1208$ and different Cm. (a) $H = 4.3$ Oe, $Cm = 31$, (b) $H = 8.6$ Oe, $Cm = 62.5$, (c) $H = 12.9$ Oe, $Cm = 93.8$.

A direct way of comparing experiments with the numerical data is by looking at the filament shapes. The experimental system with an optical microscope allows us only to view the 2d shape of the filament in the $x-y$ plane, while the third dimension can be seen by the out of focus blur. Using the parameters A and B, as well as knowing the filament length $L = 46$ μm allows us to overlay experimental images with projections of numerical results on the $x-y$ plane. This can be seen in Fig. 10 for 3 different magnetic fields. A qualitative agreement is easily visible. Notable discrepancies can be seen for the lower part of the filament. This clearly justifies the chosen approximations in image processing, as described in §2., namely, using the centre of rotation for determining R, not the whole length. The behaviour of the chosen part of the filament is predictable.

5 Discussion

Our results clearly show that a ferromagnetic filaments in a rotating field can have motion in the third dimension. However, this only happens above a critical frequency. An out of plane motion - precession - was predicted for soft magnetic particles in a rotating field[14]. Later this was observed experimentally for ferromagnetic nanorods[15] and recently elaborated in detail both experimentally and theoretically by Palkar *et al.*[6], where they show how a ferromagnetic rod beyond a critical frequency can have two possible regimes: unstable in-plane asynchronous back and forth motion and stable synchronous precession. It is worth noting that the critical frequency f_c both for ferromagnetic rods and filaments is proportional to the magnetic field H and inversely proportional to the length squared L^2.

Qualitatively, the appearance of the 3D regime can be explained with the interplay of the magnetic torque, the filament elasticity, the hydrodynamic drag and a small perturbation. For low frequencies the increasing frequency leads to higher drag, which is compensated by elastic deformations or reduced by the increase of the magnetic field and the corresponding torque[8]. Above a critical frequency, the magnetic torque is insufficient to deform the filament more and the drag forces the filament to lose synchronization with the field, while remaining in the plane of the rotating field. Surprisingly, a small perturbation, which might come from the Earth's magnetic field, is sufficient to rotate the

deformed filament out of plane. Coming out of the plane reduces the radius R, which results in reduced drag. Torque is once again large enough to cause a synchronous rotation, but now for a filament that is deformed in 3D. At least the appearance of stable precessing states for ferromagnetic rods is explained by analyzing the effect of small perturbations on the phase portrait[6].

Numerically, we find that the planar regime of the filament loses its stability at $\omega\tau_e = 12 \cdot Cm$ and the three dimensional precessional regime is established. Thus, at the critical frequency f_c the following relation is valid $2\pi f_c \zeta L^2/(12T/L) = 1$ where T is torque and $T/L = MH$ is the torque per unit length of the filament. It should be noted that taking $\zeta = 4\pi\eta/\log(L/d)$ and $T/L = \pi^2\chi^2 H^2 d^2/6$, a similar relation is valid for the critical frequency of a chain of paramagnetic particles with a susceptibility χ and a diameter d[16]. While relations for critical frequencies are similar, the important difference is in their behaviour beyond f_c. A paramagnetic filament undergoes a planar back and forth regime, while a ferromagnetic filament transitions to the 3D regime. This is in agreement with the behaviour of ferromagnetic and paramagnetic rods in a rotating field. Beyond the critical frequency a paramagnetic rod has only the back and forth regime, while the ferromagnetic rods have both in-plane and out of plane behaviour, as discussed earlier.

For paramagnetic filaments at high frequencies of the rotating field a peculiar behaviour of filament coiling can be observed[16]. This behaviour was not seen for ferromagnetic filaments. It is probably due to the finite magnetic relaxation time of paramagnetic beads[17].

Another interesting point is the value of the bending modulus of the DNA linked ferromagnetic particle chain. Here we find $A_b = 1.5 \cdot 10^{-12}$ erg·cm. This is one order of magnitude larger than from the dipolar interactions $M^2/2$ ($M = 4.9 \cdot 10^{-7}$ emu)[18]. Therefore, the elastic deformations and the corresponding bending modulus in our experiments comes from the deformations of DNA linkers. It is worth adding that the bending modulus of the DNA linker based filaments depends on their length. As was shown with paramagnetic bead based filaments, the change in linker length can influence the resulting bending modulus across three orders of magnitude[19].

Rotating chains and filaments have a potential for mixing applications in microfluidics[20]. Many examples use paramagnetic particle chains, however, such filaments have a clear limitation at the critical frequency, above which filaments experience back and forth motion, which forces a reduction in mixing efficiency[1]. In comparison, ferromagnetic filaments have a transition to the three dimensional regime and continue to rotate with the angular frequency of the field. This difference should enable efficient mixing also for higher frequencies and will be studied in detail in the near future.

6 Conclusions

In this study we have investigated the regimes that flexible ferromagnetic filaments undergo with the application of a 2D rotating magnetic field. It was found that for frequencies below the critical the filament rotates synchronously with the magnetic field with an orientation lag and a slightly deformed shape. For frequencies above the critical, the filament undergoes a transition to a three dimensional precessional regime, which is similar to the behaviour of ferromagentic rods. The critical frequency f_c is lower for longer filaments and higher for stronger magnetic fields. The experimentally obtained characteristics of this regime are in good agreement with the results of numerical simulations.

Conflicts of interest

There are no conflicts to declare

Acknowledgements

A.Z. acknowledges support from the European Union's Horizon 2020 research and innovation programme under grant agreement MAMI No. 766007, A.C. from M.era-net project FMF No.1.1.1.5./ERANET/18/04 and G.K. from PostDocLatvia grant No. 1.1.1.2/VIAA/1/16/197. Authors thank J. Cimurs for discussions.

Notes and references

1 S. L. Biswal and A. P. Gast, *Analytical Chemistry*, 2004, **76**, 6448–6455.
2 S. Jeon, S. Kim, S. Ha, S. Lee, E. Kim, S. Y. Kim, S. H. Park, J. H. Jeon, S. W. Kim, C. Moon, B. J. Nelson, J.-y. Kim, S.-W. Yu and H. Choi, *Science Robotics*, 2019, **4**, eaav4317.
3 M. Driscoll and B. Delmotte, *Current Opinion in Colloid & Interface Science*, 2019, **40**, 42 – 57.
4 A. Tokarev, B. Kaufman, Y. Gu, T. Andrukh, P. H. Adler and K. G. Kornev, *Applied Physics Letters*, 2013, **102**, 033701.
5 J.-F. Berret, *Nature communications*, 2016, **7**, 10134.
6 V. Palkar, P. Aprelev, A. Salamatin, A. Brasovs, O. Kuksenok and K. G. Kornev, *Phys. Rev. E*, 2019, **100**, 051101.
7 L. Goyeau, R. Livanovičs and A. Cēbers, *Phys. Rev. E*, 2017, **96**, 062612.
8 A. Zaben, G. Kitenbergs and A. CÄŞbers, *Journal of Magnetism and Magnetic Materials*, 2020, **499**, 166233.
9 K. Ērglis, *PhD Thesis, University of Latvia*, 2010.
10 C. Zeng, S. Bird, J. J. Luce and J. Wang, *Remote Sensing*, 2015, **7**, 14055–14078.
11 K. Ērglis, R. Livanovičs and A. Cēbers, *Magnetohydrodynamics*, 2010, **46**, 245–256.
12 K. ÄŠrglis, M. Belovs and A. CÄŞbers, *Journal of Magnetism and Magnetic Materials*, 2009, **321**, 650 – 654.
13 M. Belovs and A. Cēbers, *Phys. Rev. E*, 2009, **79**, 051503.
14 J. Cīmurs and A. Cēbers, *Phys. Rev. E*, 2013, **88**, 062315.
15 P. Aprelev, B. McKinney, C. Walls and K. G. Kornev, *Physics of Fluids*, 2017, **29**, 072001.
16 S. Kuei, B. Garza and S. L. Biswal, *Phys. Rev. Fluids*, 2017, **2**, 104102.
17 A. CÄŞbers and H. Kalis, *The European Physical Journal E*, 2011, **34**, year.
18 A. CÄŞbers, *Current Opinion in Colloid & Interface Science*, 2005, **10**, 167 – 175.
19 J. Byrom, P. Han, M. Savory and S. L. Biswal, *Langmuir*, 2014, **30**, 9045–9052.

20 E.-S. Shanko, Y. van de Burgt, P. D. Anderson and J. M. J. den Toonder, *Micromachines*, 2019, **10**, 731.

scientific reports

Check for updates

OPEN

Instability caused swimming of ferromagnetic filaments in pulsed field

Abdelqader Zaben, Guntars Kitenbergs & Andrejs Cēbers✉

Magnetic filaments driven by external magnetic field are an interesting topic of research in-terms of the possible bio-medical applications. In this paper, we investigated the applicability of using ferromagnetic filaments as micro swimmers both experimentally and numerically. It was found that applying a pulse wave field profile with a duty cycle of 30% induced experimentally observable swimming, which is similar to the breast stroke of micro algae. Good agreement with numerical simulations was found. Moreover, for stable continuous swimming, an initial filament shape is required to avoid transition to the structurally preferred non-swimming S-like mode.

The dynamics of artificial micro-swimmers has been a research topic of growing interest over the past several years. Such swimmers have been shown to be promising candidates for bio-medical applications[1], as in targeted drug delivery[2] and in sensing[3]. Different designs of artificial micro-swimmers have been presented in the literature which are often inspired by biological microorganisms that uses a flagella to propel, for example, helical devices controlled by a rotating magnetic field[4] and beating flagella driven by oscillating a transverse magnetic field[5]. Here, we investigate the dynamics of a micro swimmer made from a flexible ferromagnetic particle chain and actuated by a pulse magnetic field profile, which propels by similar mechanism as Chlamydomonos Reinhardi micro algae[6].

Magnetic filaments may be synthesised by linking para- or ferromagnetic particles by some linker in order to obtain chains similar to the chains of magnetosomes found in the magnetotactic bacteria[7]. The feasibility of such a micro-swimmer design was first investigated numerically by Belovs and Cēbers[8]. The filament propels by breaking its time reversal symmetry as a result of the buckling instability when a static magnetic field is inverted, due to the difference between the bending and relaxation times. This is similar to the well-known Euler instability of a rod under the compression[9]. The buckling of magnetic filaments is determined by the competition between the magnetic and elastic energies. The bending modulus of the filament may be determined by the deformation of links[10] or the magnetic interaction of particles[11–13]. The buckling of magnetic rods and shells is studied in a series of works and we can mention just some of them[14,15]. The resultant deformation can be either an 'S' like shape, when the filament ends bend in the opposite direction or form a 'U' like shape[16,17] where the filament tangent at the center of the filament aligns with the field while its 'arms' move toward each other. The continuous propulsion is achieved by introducing a periodic magnetic field inversion profile, which results in the filament 'U' like deformations of the filament under certain initial conditions[17,18]. It is important to emphasize that anisotropy of the hydrodynamic drag is essential to have self-propulsion[19]. For an infinite rod the ratio $\zeta_\perp/\zeta_\parallel$ of drag coefficients at perpendicular $\zeta_\perp$ and parallel $\zeta_\parallel$ motion to the local orientation of the filament is approximately 2[20]. For rods of finite length this ratio is smaller, and values of 1.2–1.4 are further used in the present work. Lower ratios have been experimentally estimated using resistive force theory for swimmers at low Reynolds number. For example, a ratio of 1.4 has been found C.elegans[21], and 1.7 for sperm cells[22] swimming far from the surface.

Previous published experimental studies for artificial micro-swimmers actuated by a magnetic field, for example as presented in[23,24], have been focused on using para-magnetic material to form flexible chains. Here we experimentally validate that ferromagnetic filaments propel in a piecewise constant AC field in one dimension. We also discuss the conditions required to form the 'U' shaped configuration and ways to optimise the swimming velocity.

Results

Following the experimental procedures as presented in the "Methods" section, a static field is first applied which aligns the filament with the field, followed by a pulse wave field profile with a duty cycle of 30%, where the magnetic field is inverted for 30% of the time within one period. The duty cycle 30% is found experimentally

MMML lab, University of Latvia, Jelgavas 3, Riga 1004, Latvia. ✉email: andrejs.cebers@lu.lv

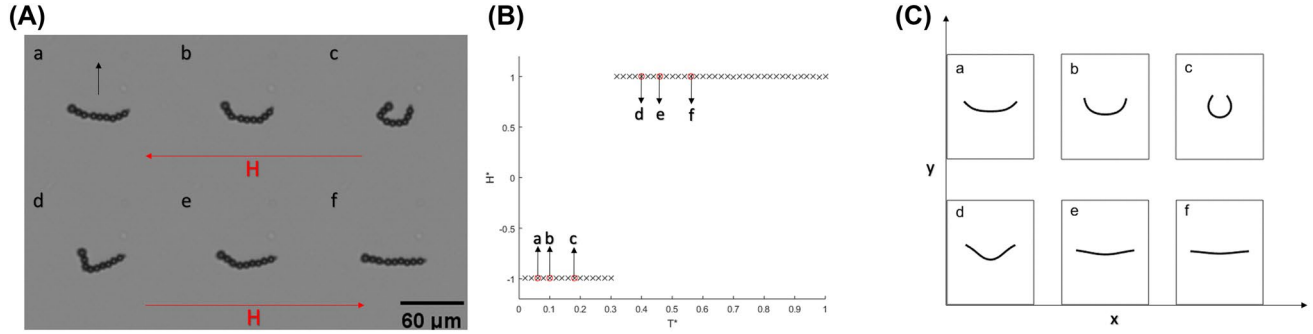

Figure 1. (**A**) An example of filament 'U' deformations under a 30% duty cycle pulse wave profile magnetic field, at different location within one period for filament with length L = 60 µm, field frequency f = 2 Hz and field strength H = 5.2 Oe. The arrow in 'a' shows the swimming direction. (**B**) Magnetic field measurements vs time over one period where $H^* = H/H_{\max}$ and $T^* = t/T$. The red circles show the readings that correspond to images (a–f) in both (**A**) and (**C**). (**C**) Filament shapes obtained by numerical simulations which are scaled with experiments shown in (**A**), $Cm = 51$ and $T/\tau = 0.0092$.

by trying different possibilities to achieve stable swimming. The choice of the definite duty cycle is based on the hypothesis of two different characteristic time scales- characteristic time of a straight filament instability growth and the characteristic time of the instability of the metastable U-like shape. A more detailed study of the last problem will be carried out in a forthcoming theoretical publication. An example of experimental filament deformation at different time t within one period T with their corresponding field reading are shown in Fig. 1A,B respectively. In Fig. 1A,a–c), the bending stage is shown. After reaching a maximum deformation in the 30% stage of the profile, the filament relaxes, as shown in Fig. 1A,d–f, until aligning with the magnetic field as shown in Fig. 1A–f. It should be noted that the lengths of the filament's 'arms' are not equal, which may be the result of defects occurring during the formation process due to the non equal number of linking DNA strands along the filament. The magnetic moment is along the tangent direction as determined by the initial condition and as a result is opposite to the field when it is in the 30% part of the cycle. In this case we have the unstable regime where the filament undergoes bending due to the buckling instability. Moreover, it was found experimentally that having the unstable regime in the 70% case the filament flips its orientation where the direction of magnetization and field correspond to the stable situation.

The filament shapes obtained by numerical simulation and corresponding to the experimentally observed shapes (Fig. 1A) are shown in Fig.1C; (a–c) shows the bending stage, followed by the relaxation stage as shown in (d–f). Scaling with experimental data was done by defining two dimensionless parameters, the magnetoelastic number $Cm = MHL^2/A_b$ and T/τ, where M is the magnetization per unit length, H is the magnetic field strength, L is the filament length, A_b is the bending modulus, the elastic relaxation time $\tau = \zeta_\perp L^4/A_b$, and $\zeta_\perp$ is the hydrodynamic drag coefficient which is estimated by $4\pi\eta$. For the values of filament physical properties M and A_b we use $M = 4.9 \pm 5.0 \times 10^{-7}$ emu and $1.5 \pm 2.0 \times 10^{-12}$ erg cm, respectively. These values were previously estimated in Ref.[25]. Moreover, we define here the anisotropy of the hydrodynamic drag coefficient λ as − 0.2 to account for the filament flexibility and length, where $\lambda = -(\zeta_\perp/\zeta_\parallel - 1)$. An example video of an experimental and numerical swimming filament can be found in the Supplementary Video S1.

This model was previously used in the numerical investigation of a ferromagnetic swimmer[8] and a 3D study of loop formation by a ferromagnetic filament due to field inversion[17,18]. Here we modify the model to account for the piece-wise periodic field profile similar to the one defined in the experiments—a pulse wave profile with having the unstable part in the 30% of the period. Furthermore, a condition is added to the model to prevent the filament from completely relaxing and to always have a slightly curved shape before the start of the bending stage in the unstable part of the field.

The initial curved shapes of the filament can be seen in Fig. 2a. This modification was made to account for the experimentally observed filament shapes where the filament was found not to completely relax and align with the magnetic field in the stable part of the field. An example of comparison between the experimental and numerical initial configurations of the filament is shown in Fig. 2a. Moreover, it was found numerically that if the condition of initial curved shape was not applied under the defined conditions similar to experiments, the 'U'-shaped deformation could not be achieved and the filament underwent the favoured 'S'-like deformation resulting in no propulsion. This is shown in Fig. 2b,c; in (b) the simulations were done without the initial curvature and in (c) 'U' was observed to have the initial filament shape before the start of the bending stage. Therefore, we propose that without an initial filament shape before the unstable part of the field, the filament will not undergo the 'U' shape swimming deformation mode and prefer the 'S' deformation mode instead. An example video of experimentally observed shapes with corresponding numerical simulations is shown in Supplementary Video S2.

The swimming behaviour was characterised by the filaments mass center velocity under different operating conditions. The swimming direction was found to be perpendicular to the applied field in the y-direction. Experimentally slight displacements were observed in the x-direction, probably due to the difference in the arms length as mentioned in previously. The y-displacements obtained from filament centre of mass were registered for each time step. The behaviour of the three different experiments can be seen as the diamonds, squares and circles in Fig. 3a scaled by τ and the filament length. Similarly, the corresponding y-displacements of filament's

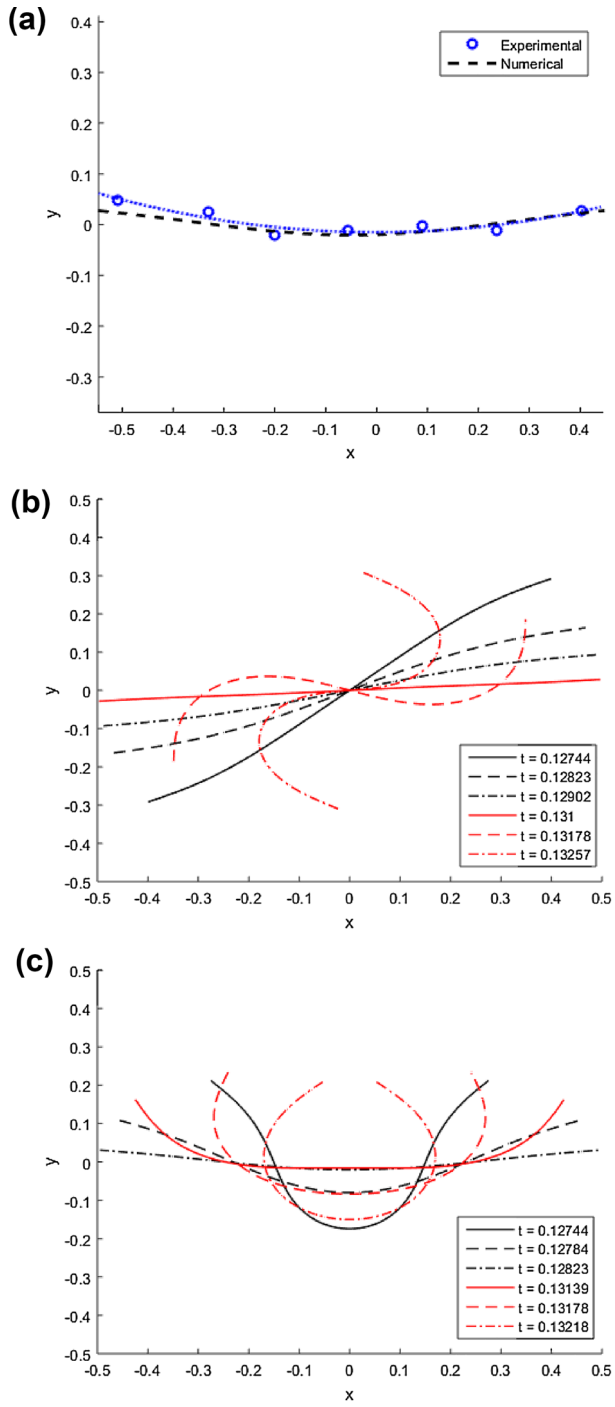

Figure 2. (**a**) Relaxed filament shapes obtained from experimental data and numerical simulations. For dashed line, $Cm = 30$ and $T/\tau = 0.0013$. The circles donates particle centres of experimental data with $L = 48\,\mu m$ and $H = 5.2$ Oe. (**b**,**c**) Filament shapes obtained by numerical simulations, red and black lines donates the configuration during bending and relaxation stage respectively within one period at different time moments t; $Cm = 70$ and $T/\tau = 0.0052$. (**b**) and (**c**) shows the difference of results without and with the condition of curved initial shape respectively.

median were obtained from numerical simulations as shown in the dashed lines in Fig. 3a. The swimming velocity was then obtained by a linear fit of the y-displacement vs time.

The experiments were repeated for filaments with three different lengths, a range of frequencies and at fixed field strength. The results for the experimental swimming velocity vs frequency are shown in Fig. 3b (data points) and by numerical simulation (solid lines). Here we repeated the simulations using λ values of − 0.2 and − 0.4 (lower and upper solid line respectively). It was noticed that for filaments with lengths 48 μm and 59 μm the

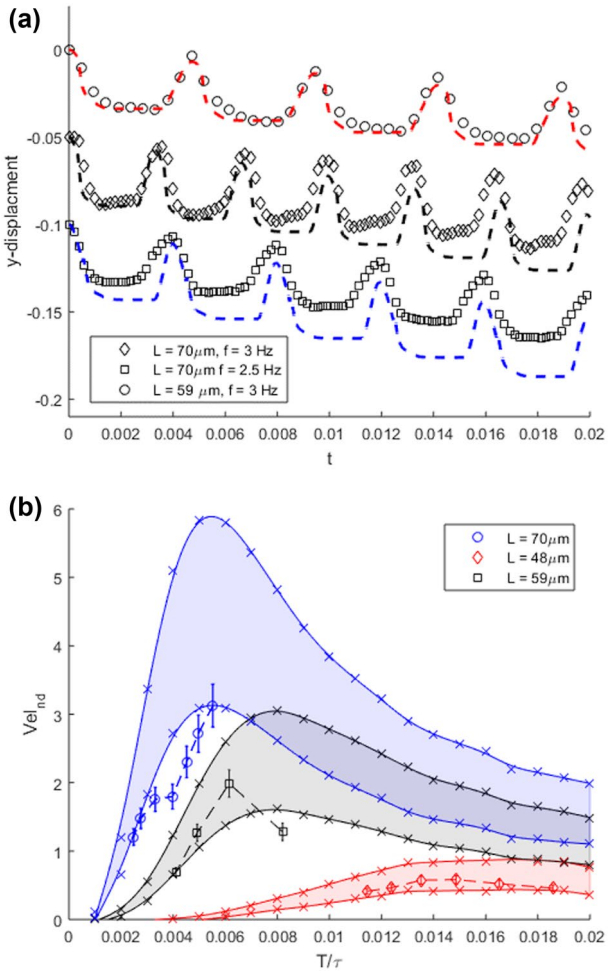

Figure 3. (**a**) Relationship between filament centre of mass y-displacements vs time, circle, diamond and square points donates experimental data. The displacement is scaled by the filament length on the y-axis and with $\tau = 54$ s (diamond and square) and 42 s (circle) on the x-axis. The dashed shows the numerical filament centre with points that correspond to the experiment (black: $Cm = 70, T/\tau = 0.0039$), (blue: $Cm = 70$, $T/\tau = 0.031$) and (red: $Cm = 50, T/\tau = 0.0047$). (**b**) Scatter points: velocity vs frequency for filaments with lengths $L = 48\,\mu$m (diamond), 59 μm (circle) and 70 μm (square) scaled with L/τ on y-axis and τ on the x-axis, operating at a range of frequencies and fixed field strength $H = 5.2$ Oe. The solid lines represent numerical simulations over range of T/τ: $Cm = 70$ (Blue), $Cm = 50$ (Black) and $Cm = 30$ (red). Colored regions boundaries corresponds simulations by defining $\lambda = -0.2$ and -0.4 for lower and upper lines respectively.

velocity reaches to a maximum and then drops. The velocity of 70 μm filament was found to decrease in the range of frequencies examined. Due to experimental limitation, the behaviour at lower frequencies could not be registered as the filament ends will get connected to each other and form a ring like shape. An example of a similar ring like shape can be seen in Fig. 4a. Figure 4 shows the maximum observed filament deformation under different operating conditions within one period. The effect of increasing the frequency is shown in Fig. 4a–c for the same filament operating at a fixed field strength; It was observed that the filament deformation decreases as the frequency is increased. The maximum curvature in the middle section decreases when the length is increased, as shown in Fig. 4a,d, at fixed frequency and field strength.

From the velocity and length ranges obtained shown in Fig. 3b, the calculated Reynolds number is found to be in the magnitude order of $\approx 10^{-4}$. Therefore, the propulsion can be assumed to be mainly driven by viscous forces in this regime. By comparing, the experimental filament shapes during bending and relaxation stages at a constant time step, a slight difference of shapes is observed in these stages; resulting in breaking the time reversal symmetry. Thereby satisfying the scallop theorem[26] to provide propulsion in Stokes hydrodynamics, while the filament velocity is not linearly dependent on the field frequency and is also a function of the difference in filament shapes during bending and relaxation stages. An example of shape difference during bending and relaxation at a constant time step over one period is shown in Fig. 5a. The difference in time between bending and relaxation stages can be seen by registering the difference of x-displacements for both of the filament's ends d^* over time, as shown in Fig. 5b. The experimental results shown in the cross and circle points are scaled by the filament length, while the dashed line shows the corresponding numerical simulations.

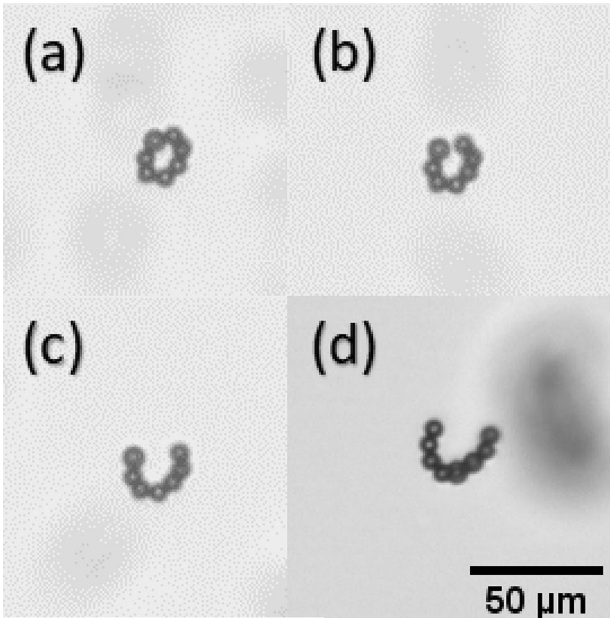

Figure 4. Maximum observed filament deformation within one period for different filaments. In (**a**–**c**) $L = 48\,\mu$m, $H = 5.2$ Oe and $f = 4 - 6$ Hz. In (**d**) $L = 53\,\mu$m at fixed $f = 4$ Hz and $H = 5.2$ Oe.

We see good agreement between the numerical and experimental results as shown in the figures presented above. Nevertheless, some discrepancies were noticed, which may be due to the small variation of the filament's physical properties such as the difference in the number of linked DNA strands between the particles and the variation in particle sizes. Moreover, the anisotropy of the hydrodynamic drag coefficient λ is length dependent, which can affect both the shape and the velocity in the numerical simulations. The swimming velocity can be optimised by either changing the field profile, as shown in Fig. 5b, in this way the time between the bending and relaxation, where the filament is stationary can be reduced. The field unstable time ratio within one period should be maintained to avoid cessation of swimming and transition to S-shape mode. This transition was numerically investigated in Ref.[18], and was also observed experimentally. By having the same field profile, the maximum swimming velocity as shown in Fig. 3b, can be achieved by having values of d^* close to zero. Moreover, lower values of Cm will give a wider range of operating frequency to achieve the maximum velocity, due to reduced flexibility to form a ring-like shape.

Discussion

Buckling of the ferromagnetic filament in the pulsed magnetic field induces its propulsion. Anisotropy of hydrodynamic drag is essential for this. Quantitative description of experimental data shows that the ratio of the perpendicular and parallel hydrodynamicdrag coefficients is less than 2—a value valid for an infinite straight rod as observed also for different microorganisms. The mechanism of propulsion, as shown by experimental and numerical results, consists of breaking the time inversion symmetry between the bending and straightening stages of the filament. Achieved propulsion velocities by this mechanism are not very high and in the best cases gives a displacement of several percents of the filament length per period, which is much less than, for example, for example, for spermatozoon[27], which propel at much higher frequencies of deformation. The corresponding frequency range is not accessible for the present filaments since it requires higher field values at which these filaments would break.

To compare the swimming performance of ferromagnetic filaments with those observed for microorganisms[28], we see that average displacement per period of Chlamydomonas $\Delta x_{CR} \approx 2.5\,\mu$m is only 3 times larger than for our fastest swimmer ($\Delta x \approx 0.75\,\mu$m at $v = 3\,\mu$m/s and $f = 4$ Hz). Thus we believe that the ferromagnetic filament is a demonstration of an artificial puller type microswimmer[29].

Methods

Experimental. The filaments are made from ferromagnetic particles functionalized with strepdavidin linked together by biotinized DNA fragments. The 4.26 μm average diameter magnetic particles (Spherotech, 1% w/v) are first mixed with 1000 base pairs long DNA strands (ASLA biotech, biotinated on the 5′ ends) in a TE buffer solution ($\eta = 0.01$ P, pH = 7.5). The sample is then placed between two Neodymium magnets (field strength ≈ 500 Oe) for two minutes to allow the particles to align and form the filaments. More details about the filament formation methodology can be found in Ref.[30]. For sample observation, fluidic cells are used; made from two glass slides and separated by 211 μm thick double side adhesive tape. The behaviour of the filaments are registered by optical microscopy (Leica DMI3000B, objectve 10×, bright field mode), via Basler ac1920-155um camera using a fixed acquisition rate of up to 100 Hz. A coil system, which consists of six coils is used to

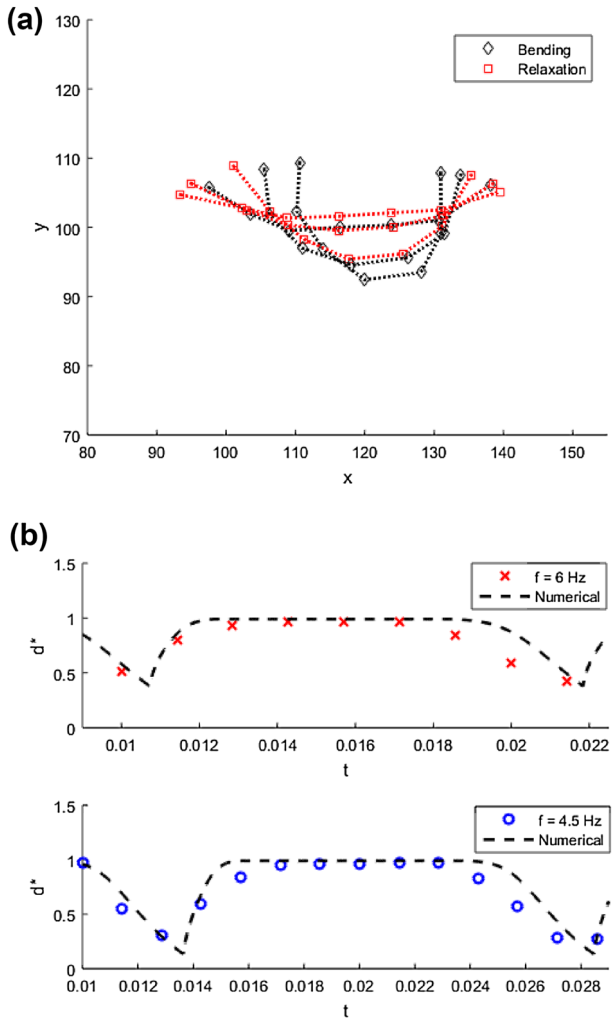

Figure 5. (**a**) Experimental filament configurations showing the difference in bending and relaxation stages at a constant time step over one period. (**b**) End to end x-displacement of filament tips (d^*) vs time. Scatter points for experimental data for filament with length $L = 48\,\mu m$, $H = 5.2$ Oe, frequency $f = 6$ Hz (cross) and $f = 4.5$ (circle). Dashed line shows numerical simulation results of d^*; $Cm = 30$, $\lambda = -0.2, T/\tau = 0.011$ (upper plot) and $T/\tau = 0.014$ (lower plot).

generate the magnetic field. Each coil pair is connected to an AC power supply (Kepco BOP 20-10M). The power supplies are controlled by LabVIEW program via NI-PCI-6229 data acquisition card.

The images are processed using Matlab, the filaments are first segmented from the image by intensity threshold resulting in a binary image. And regionprops function was used to calculate the centroid of the filament. The centreline of the filament is obtained from the particle centre points using circular Hough transform function. The above results for velocity calculation presented are for 500 images processed for each data point, with an acquisition frame rate of 50 fps.

Data availability

Experimental and numerical data used in this study will be published on the open-access repository (https://zenodo.org).

Code availability

Codes used in this work are available from the authors upon request.

Received: 21 August 2021; Accepted: 10 November 2021
Published online: 03 December 2021

References

1. Wang, L., Meng, Z., Chen, Y. & Zheng, Y. Engineering magnetic micro/nanorobots for versatile biomedical applications. *Adv. Intell. Syst.* **3**, 2000267 (2021).

2. Ahmed, D., Dillinger, C., Hong, A. & Nelson, B. J. Artificial acousto-magnetic soft microswimmers. *Adv. Mater. Technol.* **2**, 1700050 (2017).
3. Peng, X. *et al.* Opto-thermoelectric microswimmers. *Light Sci. Appl.* **9**, 064107 (2020).
4. Zhang, L. *et al.* Artificial bacterial flagella: Fabrication and magnetic control. *Appl. Phys. Lett.* **94**, 064107 (2009).
5. Dreyfus, R. *et al.* Microscopic artificial swimmers. *Nature* **437**, 862–865 (2005).
6. Ringo, D. Flagellar motion and fine structure of the flagellar apparatus in chlamydomonas. *J. Cell Biol.* **33**, 543–571 (1967).
7. Blakemore, R. P. Magnetotactic bacteria. *Annu. Rev. Microbiol.* **36**, 217–238 (1982).
8. Belovs, M. & Cēbers, A. Ferromagnetic microswimmer. *Phys. Rev. E* **79**, 051503 (2009).
9. Pilyugina, E., Krajina, B., Spakowitz, A. J. & Schieber, J. D. Buckling a semiflexible polymer chain under compression. *Polymers* **9**, 99 (2017).
10. Koenig, A. *et al.* Magnetic force probe for nanoscale biomolecules. *Phys. Rev. Lett.* **95**, 128301 (2005).
11. Cēbers, A. Flexible magnetic filaments. *Curr. Opin. Colloid Interface Sci.* **10**, 167–175 (2005).
12. Vella, D., du Pontavice, E., Hall, C. L. & Goriely, A. The magneto-elastica: From self-buckling to self-assembly. *Proc. R. Soc. A Math. Phys. Eng. Sci.* **470**, 20130609 (2014).
13. Kiani, B., Faivre, D. & Klumpp, S. Elastic properties of magnetosome chains. *New J. Phys.* **17**, 043007 (2015).
14. Su, T., Liu, J., Terwagne, D., Reis, P. M. & Bertoldi, K. Buckling of an elastic rod embedded on an elastomeric matrix: Planar vs. non-planar configurations. *Soft Matter* **10**, 6294–6302 (2014).
15. Yan, D., Pezzulla, M., Cruveiller, L., Abbasi, A. & Reis, P. M. Magneto-active elastic shells with tunable buckling strength. *Nat. Commun.* **12**, 2831 (2021).
16. Belovs, M. & Cēbers, A. Nonlinear dynamics of semiflexible magnetic filaments in an ac magnetic field. *Phys. Rev. E* **73**, 051503 (2006).
17. Ērglis, K., Livanovičs, R. & Cēbers, A. Three dimensional instability of flexible ferromagnetic filament loop. *Magnetohydrodynamics* **46**, 245–256 (2010).
18. Ērglis, K., Livanovičs, R. & Cēbers, A. Three dimensional dynamics of ferromagnetic swimmer. *J. Magn. Magn. Mater.* **323**, 1278–1282 (2011).
19. Lauga, E. & Powers, T. R. The hydrodynamics of swimming microorganisms. *Rep. Prog. Phys.* **72**, 096601 (2009).
20. Powers, T. R. Dynamics of filaments and membranes in a viscous fluid. *Rev. Mod. Phys.* **82**, 1607–1631 (2010).
21. Sznitman, J., Shen, X., Sznitman, R. & Arratia, P. E. Propulsive force measurements and flow behavior of undulatory swimmers at low Reynolds number. *Phys. Fluids* **22**, 121901 (2010).
22. Friedrich, B. M., Riedel-Kruse, I. H., Howard, J. & Jülicher, F. High-precision tracking of sperm swimming fine structure provides strong test of resistive force theory. *J. Exp. Biol.* **213**, 1226–1234 (2010).
23. Ido, Y., Li, Y.-H., Tsutsumi, H., Sumiyoshi, H. & Chen, C.-Y. Magnetic microchains and microswimmers in an oscillating magnetic field. *Biomicrofluidics* **10**, 011902 (2016).
24. Li, Y.-H., Lin, H.-C. & Chen, C.-Y. Steering of magnetic micro-swimmers. *IEEE Trans. Magn.* **49**, 4120–4123 (2013).
25. Zaben, A., Kitenbergs, G. & Cēbers, A. 3d motion of flexible ferromagnetic filaments under a rotating magnetic field. *Soft Matter* **16**, 4477–4483 (2020).
26. Purcell, E. M. Life at low Reynolds number. *Am. J. Phys.* **45**, 3–11 (1977).
27. VelhoRodrigues, M. F., Lisicki, M. & Lauga, E. The bank of swimming organisms at the micron scale (boso-micro). *PLoS One* **16**, 1–80 (2021).
28. Goldstein, R. Batchelor prize lecture fluid dynamics at the scale of the cell. *J. Fluid Mech.* **807**, 1–39 (2016).
29. Drescher, K., Goldstein, R. E., Michel, N., Polin, M. & Tuval, I. Direct measurement of the flow field around swimming microorganisms. *Phys. Rev. Lett.* **105**, 168101. https://doi.org/10.1103/PhysRevLett.105.168101 (2010).
30. Ērglis, K. Experimental study of properties and motion of flexible magnetic microfilaments, PhD Thesis, University of Latvia (2010).

Acknowledgements

A.C. and G.K. acknowledge support by grant of the Latvian Council of Science lzp-2020/1-0149 and M.era-net project FMF No.1.1.1.5/ERANET/18/04. A.Z. acknowledges support from the European Union's Horizon 2020 research and innovation programme under grant agreement MAMI No. 766007. Authors are thankful to R.Livanovičs for discussion.

Author contributions

A.Z. carried out experimental measurements and made numerical calculations with the participation of A.C., G.K. participated in experimental work, contributed in data acquisition. A.C. elaborated numerical algorithm, participated in the interpretation of experimental results. All authors discussed and interpretated results. A.C. conceived the project. A.Z. and A.C. wrote the paper.

Competing interests

The authors declare no competing interests.

Additional information

Supplementary Information The online version contains supplementary material available at https://doi.org/10.1038/s41598-021-02541-3.

Correspondence and requests for materials should be addressed to A.C.

Reprints and permissions information is available at www.nature.com/reprints.

Publisher's note Springer Nature remains neutral with regard to jurisdictional claims in published maps and institutional affiliations.

Appendix B

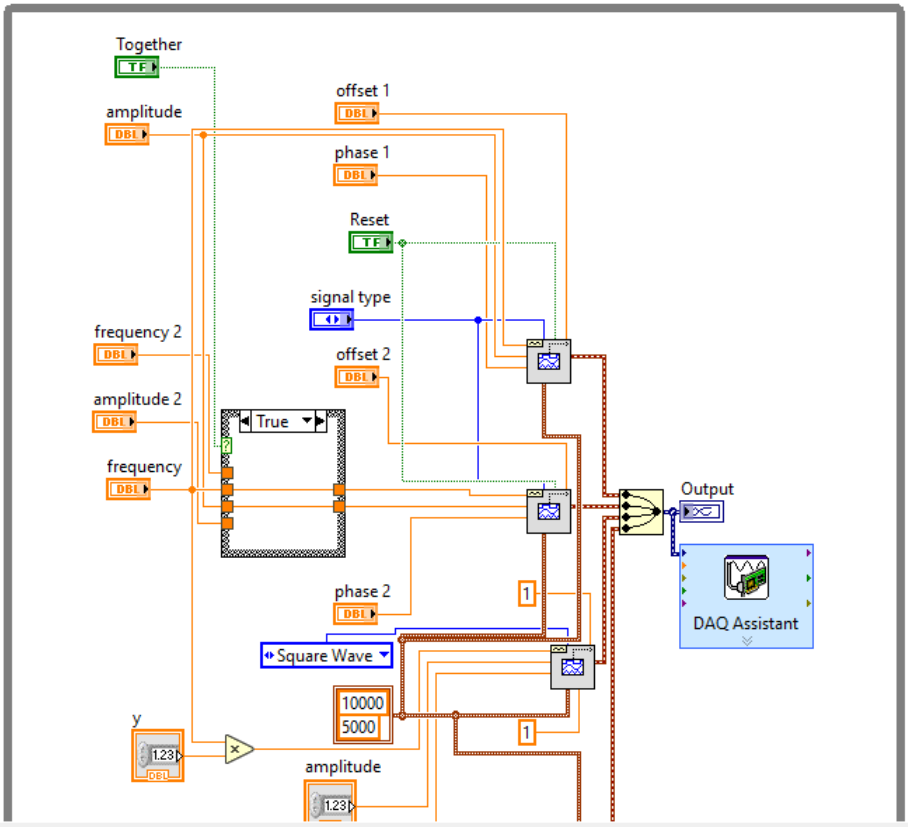
Together
amplitude
offset 1
phase 1
Reset
signal type
frequency 2
offset 2
amplitude 2
True
frequency
Output
DAQ Assistant
phase 2
Square Wave
10000
5000
y
amplitude

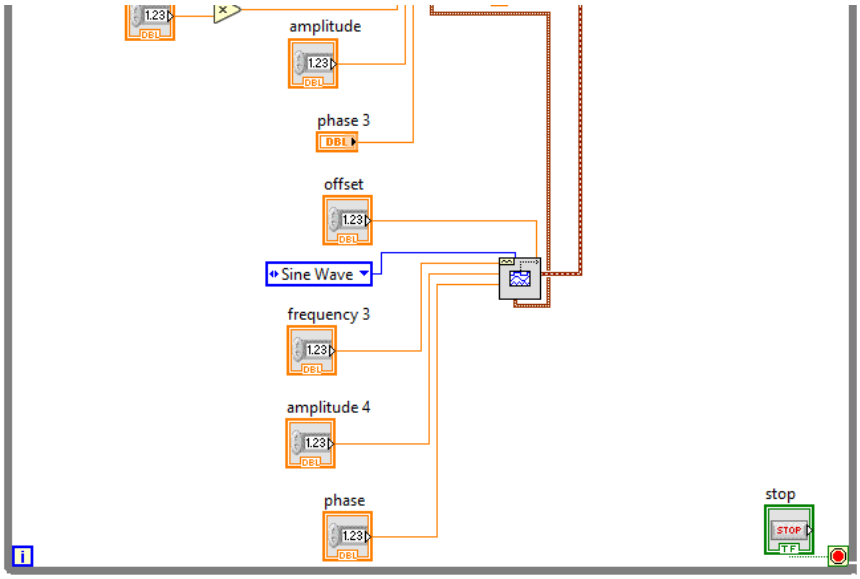
amplitude
phase 3
offset
Sine Wave
frequency 3
amplitude 4
phase
stop

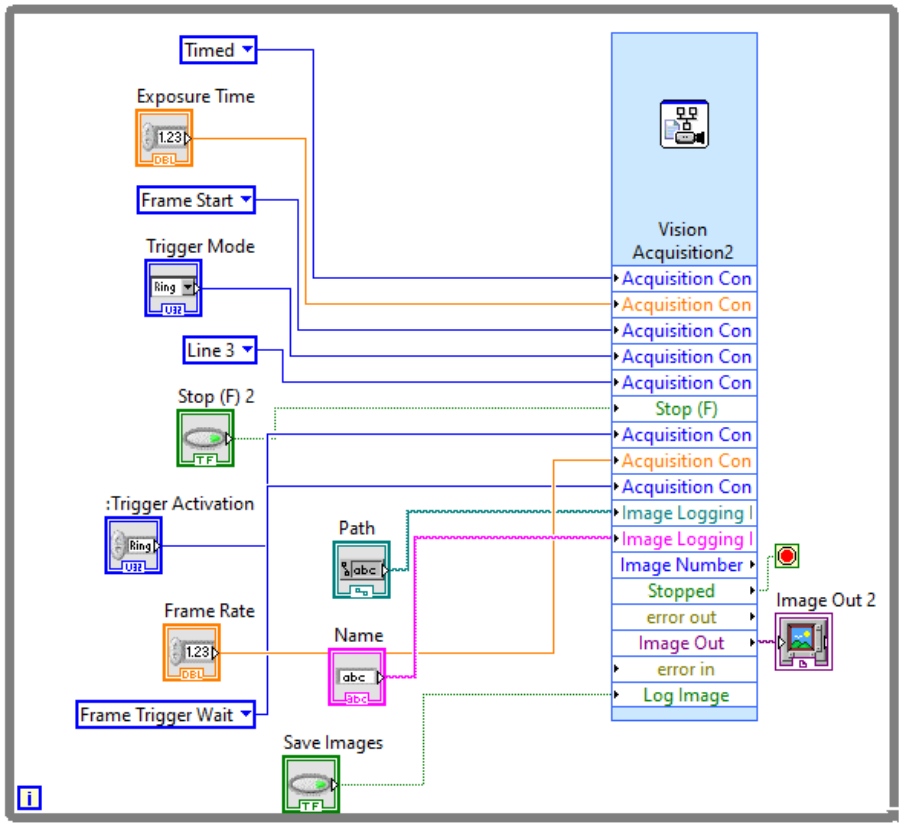

FIGURE B.1: LabVIEW block diagram showing the program used for field profile definition that is sent to the power supplies and image acquisition, which triggered by pulse signal at a defined location.

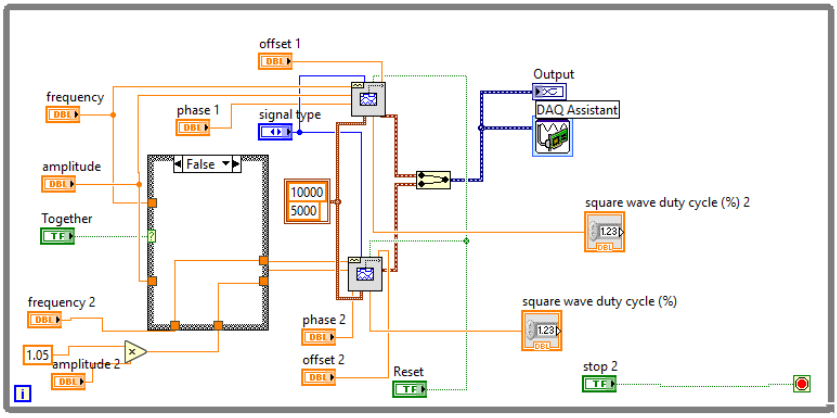

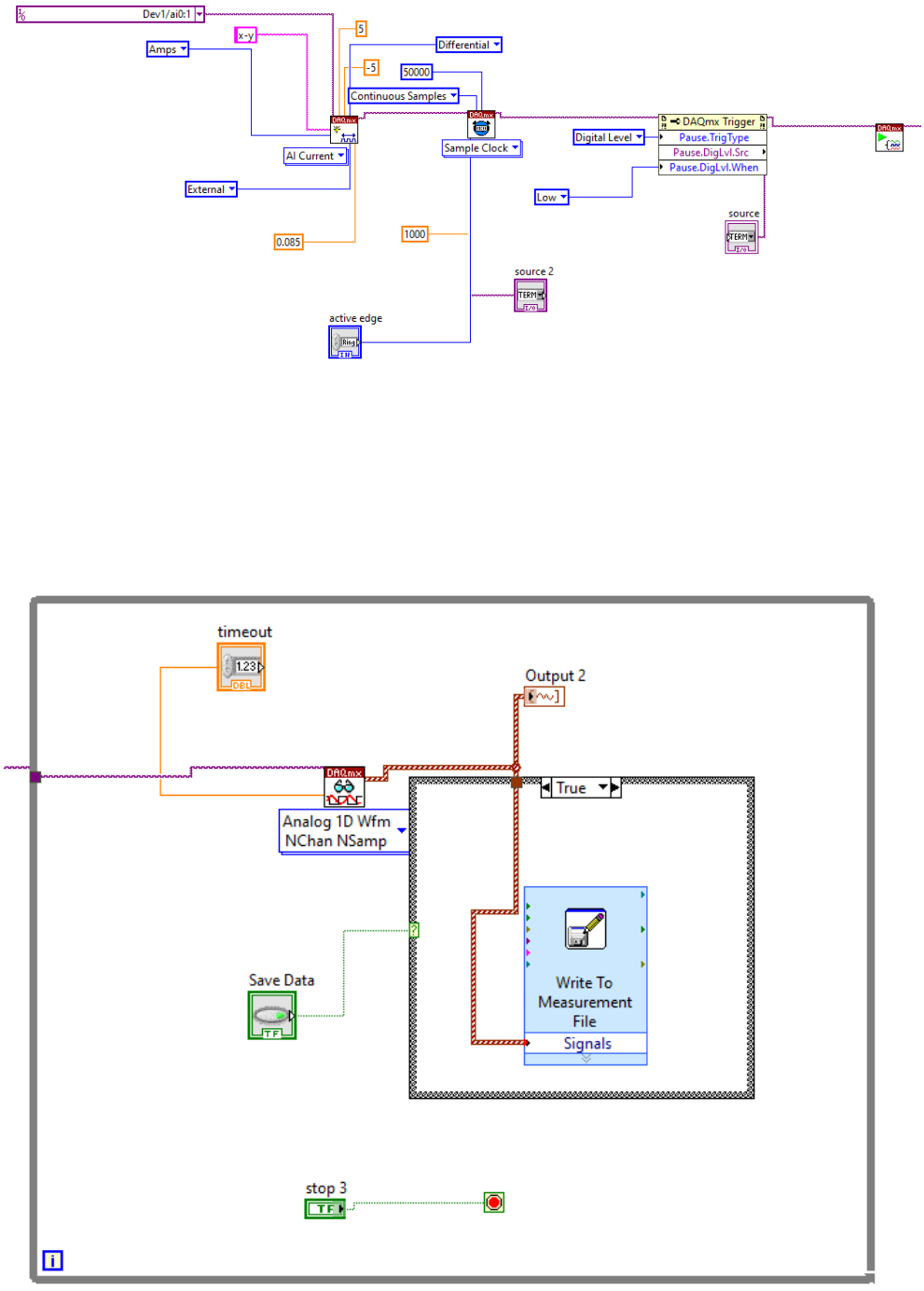

FIGURE B.2: LabVIEW block diagram showing the program used for field profile definition that is sent to the coils and magnetic field readings, which are registered by a signal received from the camera